

Copyright

by

Paul Byron Jordan

2016

**The Thesis Committee for Paul Byron Jordan
Certifies that this is the approved version of the following thesis:**

**Two-Phase Relative Permeability Measurements in Berea Sandstone at
Reservoir Conditions**

**APPROVED BY
SUPERVISING COMMITTEE:**

Supervisor:

Gary A. Pope

Co-Supervisor:

David A. DiCarlo

**Two-Phase Relative Permeability Measurements in Berea Sandstone at
Reservoir Conditions**

by

Paul Byron Jordan, B.S.Ch.E

Thesis

Presented to the Faculty of the Graduate School of

The University of Texas at Austin

in Partial Fulfillment

of the Requirements

for the Degree of

Master of Science in Engineering

The University of Texas at Austin

December 2016

Dedication

To my family and friends for their unwavering support.

Acknowledgements

First and foremost, I would like to thank Dr. Gary Pope for his rigorous guidance and supervision. It is inspiring to work under someone of such great scientific experience and deep academic prowess. I would like to thank Dr. David DiCarlo for his excellent supervision and outstanding leadership in my theoretical and experimental work. I am especially grateful to Dr. Rafael Longoria for his extensive assistance with the experiments as well as his expert analysis of the data. His vast technical experience, knowledge, and understanding made this study possible. He also helped me with the preparation of this thesis with his tireless review and editing of its many drafts.

An emphatic thanks to Pathma Jith Liyanage and his excellent team, including Brien Allen, Arnob Bhuyan, Austin Lim, Patrick Lim, Willie Martin, Travis Pitcher, Erin Shook, Adam Verna, and everyone else for their unending supply of technical expertise and help.

A deep thank you to fellow graduate students Leonard Chang, Lauren Churchwell, Johnathan Driver, Sean Li, Nabi Nizamidin, and Denning Wang as well as post-doctoral fellows Jun Lu, Sung-Hyun Jang, and Nadeeka Upamali. Our camaraderie made my graduate school experience all the more memorable.

Lastly, a big thank you to Esther Barrientes and everyone within the Petroleum Engineering Department at the University of Texas at Austin for their help throughout my entire graduate career. I wish everyone the best of luck in their bright futures.

Abstract

Two-Phase Relative Permeability Measurements in Berea Sandstone at Reservoir Conditions

Paul Byron Jordan, M.S.E.

The University of Texas at Austin, 2016

Supervisor: Gary A. Pope

Co-Supervisor: David A. DiCarlo

The goal of this research was to explore the role of composition on relative permeability by performing two-phase steady-state relative permeability measurements. The effect of changing fluid composition was studied by using different fluid pairs: CO₂/brine, N₂/brine and n-decane/brine. In addition, the experiments were performed at two different pressures for the same fluid pair, CO₂/brine, since pressure also changes fluid properties such as density that may have an effect on the relative permeability.

A very important part of this study was the establishment of the experimental procedures needed to ensure accurate measurements of the relative permeability. These are difficult measurements subject to many experimental artifacts and complications. For example, a special effort was made to reduce capillary end effects in these experiments.

Although many studies have reported relative permeability measurements for N₂/brine, CO₂/brine, or oil/brine, this is the first experimental study where the relative permeability for different fluids was measured using precisely the same methodology.

The same core was used for all experiments allowing for a direct comparison between the different fluids. Furthermore, special care was taken in this study to eliminate experimental artifacts that affect relative permeability measurements. In particular, experiments were performed at a high Rapoport-Leas number to minimize capillary end effects. Fractional flow effects, e.g. not being able to flow enough pore volumes to reach residual saturation throughout the whole core, while not eliminated, were circumvented by measuring sectional pressure drops, as opposed to only the pressure drop over the whole core.

Table of Contents

List of Tables	xi
List of Figures	xiii
Chapter 1 – Introduction	1
Chapter 2 – Background and Theory	3
2.1 Fluid Flow	3
2.2 Tracers.....	6
2.3 Capillary Pressure	7
2.3.1 Capillary End Effect	10
2.3.2 Capillary Number.....	12
2.4 Corey-Type Curves.....	13
Chapter 3 – Materials and Methods	15
3.1 Rock	15
3.2 Fluids.....	19
3.2.1 Brines	19
3.2.2 Carbon Dioxide.....	20
3.2.3 Nitrogen	21
3.2.4 Oil	22
3.2.5 Interfacial Tension	25
3.3 Apparatus	26
3.3.1 Pumps.....	31
3.3.2 Mass Flow Controller	31
3.3.3 Back Pressure Regulators	32
3.3.4 Dead Volumes.....	32
3.3.5 Sample Collection.....	33
3.3.6 Residual Water Saturation Measurement.....	34
3.3.7 Ultraviolet Spectrophotometer.....	34
3.4 Troubleshooting.....	35
3.4.1 Carbon Dioxide Absorption and Attack	35

3.4.2 O-Rings	36
3.4.3 Back Pressure Regulators	36
3.4.4 Transducer Manifold Gas Diffusion	37
3.4.5 Sectional Pressure Drops	37
3.4.6 Joule-Thomson Effect.....	41
3.4.7 Gas Compression Effects.....	42
3.5 Procedure for Relative Permeability Measurements.....	43
Chapter 4 – Results and Analysis	46
4.1 Initial Testing.....	47
4.2 Carbon Dioxide and Brine Relative Permeability Experiments	49
4.2.1 High Density CO ₂	49
4.2.1.1 Drainage Relative Permeability Measurement	51
4.2.1.2 Imbibition Relative Permeability Measurement	54
4.2.2 Low Density CO ₂	57
4.2.2.1 Drainage Relative Permeability Measurement	58
4.2.2.2 Imbibition Relative Permeability Measurement	61
4.3 Nitrogen and Brine Relative Permeability Experiments.....	64
4.3.1 Drainage Relative Permeability Measurement	64
4.3.2 Imbibition Relative Permeability Measurement	69
4.4 Decane and Brine Relative Permeability Experiments.....	72
4.5 Comparison of Relative Permeability Data	75
4.5.1 Relative Permeabilities	75
4.5.1.1 High Density CO ₂ versus N ₂	75
4.5.1.2 Low Density CO ₂ versus N ₂	78
4.5.1.3 High Density CO ₂ versus Low Density CO ₂	81
4.5.1.4 N ₂ versus n-Decane.....	84
4.5.1.5 High Density CO ₂ versus n-Decane.....	86
4.5.2 Corey Parameters	88
4.5.2.1 Exponents.....	88
4.5.2.2 Residual Saturations.....	90

4.5.2.3 Endpoint Relative Permeabilities.....	92
4.5.3 Sectional Permeabilities.....	93
4.6 Literature Comparisons.....	96
4.6.1 High Density scCO ₂ /Brine versus Liquid CO ₂ /Brine Relative Permeabilities in Berea Sandstone.....	97
4.6.2 n-Decane/Brine in Guelph Dolomite versus High Density CO ₂ /Brine in Berea Sandstone.....	100
4.6.3 High Density CO ₂ /Brine in Berea Sandstone	102
4.6.4 N ₂ /Brine in Berea Sandstone	105
4.6.4.1 Drainage.....	105
4.6.4.2 Imbibition.....	108
4.6.5 Oil/Brine Drainage in Berea Sandstone.....	109
Chapter 5 - Summary, Conclusions, and Future Work.....	111
5.1 Summary and Conclusions	111
5.2 Future work.....	114
Appendix.....	116
High Density CO ₂ and Brine Flooding.....	116
Drainage Regime	116
Imbibition Regime	121
Low Density CO ₂ and Brine Flooding.....	124
Drainage Regime	124
Imbibition Regime	127
N ₂ and Brine Flooding.....	128
Drainage Regime	128
Imbibition Regime	133
n-Decane and Brine Flooding.....	136
Drainage Regime	136
References.....	140
Vita	145

List of Tables

Table 3-1: Berea sandstone core properties.....	15
Table 3-2: Brine properties at 40 C.....	20
Table 3-3: Brine properties at 70 C.....	20
Table 3-4: CO ₂ properties at 40 C.....	21
Table 3-5: N ₂ properties at 40 C.	21
Table 3-6: n-decane properties at 70 C.	22
Table 3-7: Interfacial Tension between Brine and CO ₂	25
Table 3-8: Interfacial Tension between Brine and N ₂	25
Table 3-9: Interfacial Tension between Brine and n-decane.	25
Table 3-10: Pressure tap locations along core	26
Table 4-1: Pure fluid properties at temperature and pressure of corefloods.....	46
Table 4-2: Brine permeability data for Berea sandstone core.....	47
Table 4-3: Brine permeability data at different times.	48
Table 4-4: Flooding parameters for CO ₂ /brine relative permeability measurements at 1900 psi and 40C.	50
Table 4-5: CO ₂ and brine flooding parameters for drainage measurements.....	51
Table 4-6: High density CO ₂ and brine Corey parameters.	51
Table 4-7: 1900 psi CO ₂ and brine imbibition flooding parameters.....	55
Table 4-8: CO ₂ and brine drainage flooding parameters at low pressure.	57
Table 4-9: Low density CO ₂ and brine Corey parameters.....	58
Table 4-10: 1200 psi CO ₂ and brine imbibition flooding parameters.....	61
Table 4-11: Experimental parameters used for the N ₂ /brine drainage measurements.	64

Table 4-12: N ₂ and brine Corey parameters	65
Table 4-13: N ₂ and brine imbibition flooding parameters.....	69
Table 4-14: Brine and oil flooding parameters.....	72
Table 4-15: n-decane and brine Corey parameters.	72
Table 4-16: Imbibition relative permeabilities for high density CO ₂ /brine and N ₂ /brine.....	77
Table 4-17: Experimental fluid parameters for the research sets.....	96
Table 4-18: Comparison of oil and brine flooding residual brine saturations.	109

List of Figures

Figure 2-1: CO ₂ and brine drainage fractional flow curve at 1900 psi and 40 C. .5	
Figure 2-2: Berea sandstone capillary pressures and Leverett J-function (Pentland, 2011).8	8
Figure 2-3: Berea sandstone capillary pressure curves (Pini and Benson, 2013). .9	9
Figure 3-1: Berea sandstone core after drying.16	16
Figure 3-2: Core after wrapping with Teflon and aluminum foil.16	16
Figure 3-3: Inlet and outlet faces of core.16	16
Figure 3-4: Appearance of overall core after five months of flooding.17	17
Figure 3-5: Appearance of inlet and outlet faces of core after five months of flooding.17	17
Figure 3-6: Appearance of core after eight months of flooding.17	17
Figure 3-7: Appearance of inlet and outlet faces of core after eight months of flooding.18	18
Figure 3-8: UV absorbance of 614.24 ppm naphthalene in n-decane.22	22
Figure 3-9: Comparisons of light absorbance of different cuvette materials. . . .23	23
Figure 3-10: UV absorbance versus concentration of naphthalene in n-decane. . .24	24
Figure 3-11: Flow Diagram for CO ₂ and brine floods.27	27
Figure 3-12: Flow Diagram for N ₂ and brine floods.28	28
Figure 3-13: Flow Diagram for Oil and Brine floods.29	29
Figure 3-14: Pressure transducer manifold.30	30
Figure 3-15: Pressure drop data measured during injection of CO ₂ into core saturated with brine at 40 C and 1800 psi.38	38
Figure 3-16: Pressure data after stopping injection of CO ₂ at 40 C and 1800 psi.39	39

Figure 3-17: CO ₂ flood to residual brine pressure drop data at 40 C and 1900 psi.	40
Figure 4-1: Comparison of brine tracers before and after the permeability reduction.	48
Figure 4-2: CO ₂ and brine drainage relative permeabilities at 1900 psi.....	52
Figure 4-3: Brine drainage relative permeabilities at 1900 psi for each section of the core.....	53
Figure 4-4: CO ₂ drainage relative permeabilities at 1900 psi for each section of the core.....	54
Figure 4-5: CO ₂ and brine imbibition relative permeabilities at 1900 psi.....	55
Figure 4-6: Brine imbibition relative permeabilities at 1900 psi for each section of the core.....	56
Figure 4-7: CO ₂ imbibition sectional relative permeabilities at 1900 psi.....	56
Figure 4-8: CO ₂ and brine drainage relative permeabilities at 1200 psi.....	59
Figure 4-9: Brine drainage sectional relative permeabilities at 1200 psi.	60
Figure 4-10: CO ₂ drainage sectional relative permeabilities at 1200 psi.	60
Figure 4-11: CO ₂ and brine imbibition relative permeabilities at 1200 psi.....	62
Figure 4-12: Brine imbibition sectional relative permeabilities at 1200 psi.	63
Figure 4-13: N ₂ and brine drainage relative permeabilities at 1800 psi.	66
Figure 4-14: Brine drainage sectional relative permeabilities at 1800 psi.	67
Figure 4-15: N ₂ drainage sectional relative permeabilities at 1800 psi.	68
Figure 4-16: N ₂ and brine imbibition relative permeabilities at 1800 psi.	69
Figure 4-17: Brine imbibition sectional relative permeabilities at 1800 psi.	70
Figure 4-18: N ₂ imbibition sectional relative permeabilities at 1800 psi.	71
Figure 4-19: Oil and brine drainage relative permeabilities at 1500 psi.	73
Figure 4-20: Brine drainage sectional relative permeabilities at 1500 psi.	74

Figure 4-21: Oil drainage sectional relative permeabilities at 1500 psi.	74
Figure 4-22: Comparison of drainage relative permeabilities of high density CO ₂ /brine versus N ₂ /brine.....	76
Figure 4-23: Comparison of imbibition relative permeabilities of high density CO ₂ /brine versus N ₂ /brine.....	77
Figure 4-24: Comparison of drainage relative permeabilities of low density CO ₂ /brine versus N ₂ /brine.....	79
Figure 4-25: Comparison of imbibition relative permeabilities of low density CO ₂ /brine versus N ₂ /brine.....	80
Figure 4-26: Drainage comparisons of high density CO ₂ versus low density CO ₂ flooding.....	82
Figure 4-27: Imbibition comparisons of high density CO ₂ versus low density CO ₂ flooding.....	83
Figure 4-28: Comparison of drainage relative permeabilities of n-decane/brine versus N ₂ /brine.....	85
Figure 4-29: Comparison of drainage relative permeabilities of n-decane/brine versus high density CO ₂ /brine.....	87
Figure 4-30: Comparison of Corey-type drainage exponents for all experiments.	88
Figure 4-31: Comparison of Corey-type imbibition exponents for the high density CO ₂ /brine and N ₂ /brine experiments.	89
Figure 4-32: Comparison of the residual saturations for all experiments.....	90
Figure 4-33: Residual saturations versus the non-wetting phase density.	91
Figure 4-34: Residual saturations versus the non-wetting phase viscosity.	91
Figure 4-35: Comparison of endpoint relative permeabilities for all experiments.	92

Figure 4-36: Drainage endpoint (at residual brine saturation) sectional comparisons.	94
Figure 4-37: Inlet section drainage endpoint relative permeability versus non-wetting phase density.....	95
Figure 4-38: High density (1900 psi and 40 C) CO ₂ drainage comparison to liquid CO ₂ (Chen, 2014).....	98
Figure 4-39: High density (1900 psi and 40 C) CO ₂ imbibition comparison to liquid CO ₂ (Chen, 2014).....	99
Figure 4-40: n-Decane/brine in Guelph dolomite (Dria, 1989) versus high density CO ₂ /brine in Berea sandstone.....	101
Figure 4-41: Drainage relative permeabilities for high density scCO ₂ /brine and scCO ₂ /brine (Perrin, 2009).....	103
Figure 4-42: Drainage relative permeabilities for low density scCO ₂ /brine and scCO ₂ /brine (Perrin, 2009).....	104
Figure 4-43: Drainage relative permeabilities for N ₂ /brine from this research and N ₂ /brine (Oak, 1990).....	106
Figure 4-44: Drainage relative permeabilities for low density CO ₂ /brine from this research and N ₂ /brine (Oak, 1990).....	107
Figure 4-45: Imbibition relative permeabilities for low density CO ₂ /brine from this work and N ₂ /brine (Oak, 1990).....	108
Figure 4-46: Drainage relative permeabilities for n-decane/brine from this research and mineral/oil brine (Oak, 1990).....	110
Figure 5-1: Endpoint relative permeability and molar Gibbs free energy for all non- wetting fluids used in this study.....	114
Figure A-1: CO ₂ -saturated brine flood, 1881 psi 40 C.....	116

Figure A-2: Brine fractional flow at 0.5, 1894 psi 40 C.....	117
Figure A-3: Brine fractional flow at 0.114, 1900 psi 40 C. Sectional pressure taps became plugged during this flood.....	118
Figure A-4: Brine fractional flow at 0.125, 1858 psi 40 C.....	119
Figure A-5: Brine fractional flow at zero, 1875 psi 40 C. The discontinuities of pressure drop indicate when the apparatus was switched to a full accumulator of CO ₂	120
Figure A-6: Brine fractional flow at 0.25, 1876 psi 40 C.....	121
Figure A-7: Brine fractional flow at 0.5, 1859 psi 40 C.....	122
Figure A-8: CO ₂ -saturated brine flood, 1868 psi 40 C. Flow rate of 1 mL/min followed by 1.5 mL/min.	123
Figure A-9: CO ₂ -saturated brine flood, 1170 psi 40 C.....	124
Figure A-10: Brine fractional flow at 0.25, 1178 psi 40 C.....	125
Figure A-11: Brine fractional flow at zero, 1180 psi 40 C. The discontinuities of pressure drop indicate when the apparatus was switched to a full accumulator of CO ₂	126
Figure A-12: CO ₂ -saturated brine flood, 1176 psi 40 C. Flow rate of 0.5 mL/min followed by 1 mL/min.	127
Figure A-13: Brine fractional flow at 0.498, 1853 psi 40 C.....	128
Figure A-14: Brine fraction flow at 0.103, 1855 psi 40 C.....	129
Figure A-15: Brine fractional flow at 0.0451, 1848 psi 40 C.....	130
Figure A-16: Brine fractional flow at zero, 1889 psi 40 C.....	131
Figure A-17: Brine fractional flow at zero, 1854 psi 40 C. Flowrate increased in a stepwise fashion.....	132
Figure A-18: Brine fractional flow at 0.0559, 1845 psi 40 C.....	133

Figure A-19: Brine fractional flow at 0.198, 1843 psi 40 C.....	134
Figure A-20: Brine flooding, 1842 psi 40 C. The continually decreasing differential pressure is unexplained.....	135
Figure A-21: Brine fractional flow at 0.95, 1536 psi 70 C.....	136
Figure A-22: Brine fractional flow at 0.75, 1553 psi 70 C.....	137
Figure A-23: Brine fractional flow at 0.25, 1549 psi 70 C.....	138
Figure A-24: Brine fractional flow at zero, 1547 psi 70 C. The discontinuities of pressure drop indicate when the apparatus was switched to a full accumulator of n-decane.....	139

Chapter 1 – Introduction

Relative permeability has been studied extensively for many years due to its importance to multiple phase flow in permeable media with applications to the production of gas and oil as well as other applications such as the geological storage of carbon dioxide. The objective of this research was to explore the effect of composition on relative permeability at reservoir conditions. The steady state relative permeability was measured for two-phase flow of gas and brine and for oil and brine. The gases were carbon dioxide and nitrogen. The oil was pure n-decane. The same brine and Berea sandstone core was used in all experiments. Special care was taken to minimize experimental artifacts that affect relative permeability measurements, i.e. experiments were performed at a high flow rate to diminish capillary end effects, but the flow rates were kept below the critical capillary number. Both drainage and imbibition measurements were made for the gas and brine experiments.

The relative permeability experiments by Oak (1990) are particularly noteworthy because of the large number of systematic experiments and the high quality of the data. Oak (1990) measured the two-phase relative permeability of gas and brine in Berea sandstone. He also measured the three-phase relative permeability of gas, brine, and oil in Berea sandstone. He used nitrogen gas for these experiments.

Dria (1989) measured the two and three-phase relative permeability of gas, brine, and oil in a carbonate core. He used carbon dioxide for the gas phase because it is a commonly used gas for miscible enhanced oil recovery. The relative permeability data for carbon dioxide gas reported by Dria (1989) and the data for nitrogen gas reported by Oak (1990) are significantly different. However, Oak (1990) and Dria (1989) obtained data in different rocks and at different conditions. Yuan and Pope (2012) observed a

significant difference in gas relative permeability data reported in the literature, but the problem is despite the numerous studies over many decades and the central importance to multiphase flow in permeable media, these and other studies were not done under conditions that enable a rigorous determination of the effect of composition. Thus, the motivation for this research was to perform experiments under the same conditions to isolate the effect of composition on relative permeability.

The background and theory are presented in Chapter 2. The materials and methods are described in Chapter 3. In Chapter 4, the experimental data are presented, analyzed, and compared with data from the literature. The summary and conclusions are presented in Chapter 5.

Chapter 2 – Background and Theory

Background related to relative permeability and fractional flow basics are presented in this chapter. Tracers were used to estimate fluid saturations, so the method used to calculate the saturations from tracer data is described next. A brief review of capillary pressure end effects is presented because a major effort was made in this study to minimize end effects. The Corey-type equations used to fit the experimental relative permeability data are also described in this chapter.

2.1 FLUID FLOW

Darcy's law for the steady state flow of multiple phases in a linear permeable medium can be written as follows:

$$\frac{q_j}{A} = \frac{-kk_{rj}\Delta P}{\mu_j L} \quad (1)$$

where q_j is the flow rate of phase j , A is the cross-sectional area, k is the brine permeability at 100% brine saturation, k_{rj} is the relative permeability of phase j , ΔP is the pressure drop, μ_j is the viscosity of phase j , and L is length.

The relative permeability of a given phase depends on the saturation of that phase as well as on the saturation history and direction of saturation change. For two-phase flow, two directions exist: drainage and imbibition. Drainage refers to displacing the wetting phase with a non-wetting phase, i.e. a decreasing wetting phase saturation path. Conversely, imbibition refers to displacing the non-wetting phase with the wetting phase. The fractional flow of a water phase (f_w) in a linear core is given by:

$$f_w = \frac{q_w}{q_{total}} \quad (2)$$

where q_w is the water flow rate and q_{total} is the total flow rate. For the particular case of two-phase flow of water and gas, the fractional flow of water can be written as:

$$\frac{1}{f_w} = 1 + \frac{k_{rnw}\mu_w}{k_{rw}\mu_{nw}} \quad (3)$$

where k_{rnw} is the non-wetting phase relative permeability, k_{rw} is the water relative permeability, μ_w is the water viscosity, and μ_{nw} is the non-wetting phase viscosity. Brine, rather than pure water, was used in the relative permeability experiments, so in practice it is the brine properties that are used in the equations rather than pure water values, so from now on the term brine will be used rather than water. Relative permeability is a function of saturation so the fractional flow also depends on saturation. An example of a fractional flow curve for gas and brine is shown in Figure 2-1.

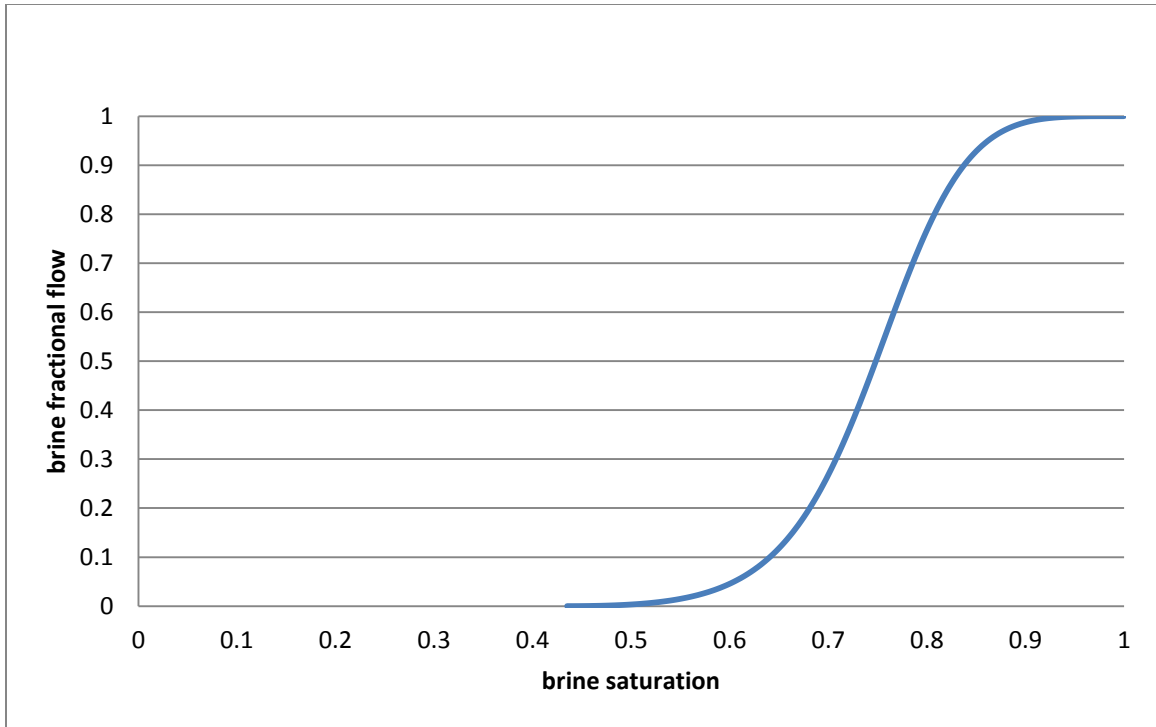


Figure 2-1: CO₂ and brine drainage fractional flow curve at 1900 psi and 40 C.

The derivative of the fractional flow curve is the saturation velocity (Lake, 1989). The inverse of the saturation velocity is the non-dimensional time (in units of pore volume [V_P]) when a given saturation breaks through at the end of the core.

$$\frac{1}{V_P} = \frac{df_W}{dS_W} \quad (4)$$

where $\frac{df}{dS_W}$ is the slope of the fractional flow curve at the target brine saturation and V_P is the pore volumes at breakthrough. This calculation was used to make initial estimates of the time required to reach steady state during two-phase injection at a fixed fractional flow. Initial estimates of the fractional flow curves were made based on fluid properties and relative permeability parameters from the literature (Chen, 2014).

2.2 TRACERS

Tracers have been used extensively to determine fluid saturations (Deans 1978, Dria 1989). Tracers by definition do not alter the properties of the fluids in the rock. An ideal tracer is stable, does not adsorb on the rock, does not change its properties, and can be detected at a low concentration. In addition, when used to determine fluid saturations in a core, the tracers should not be reactive. Ideally both partitioning and non-partitioning tracers should be used to determine saturations. However, in this work a non-partitioning tracer was used to determine saturation. The saturation was also estimated by material balance to provide two independent estimates of saturation.

The retention volume \bar{V}_i was calculated by measuring the tracer concentration C_i and phase volumes V of the effluent samples, normalizing the effluent tracer concentrations between minimum and maximum concentrations, and integrating the normalized concentration versus the phase volume using the trapezoidal rule to approximate the following integral:

$$\bar{V}_i = \int_0^{\infty} (1 - C_{Di}) dV \quad (5)$$

where C_{Di} is the normalized concentration of the tracer within its carrying phase and V is the effluent volume for the carrying phase. This is equivalent to calculating the area above the tracer curve. The volume of each phase in the outlet tubing and back-pressure regulators (the so called dead volume [V_D]) was subtracted from \bar{V}_i to calculate the saturation of phase i (S_i):

$$S_i = \frac{(\bar{V}_i - V_D)}{V_P} \quad (6)$$

2.3 CAPILLARY PRESSURE

Capillary pressure (P_C) is defined as the difference in pressure across the interface between two immiscible fluids. The Young-Laplace equation relates the capillary pressure in a narrow cylindrical tube:

$$P_C = \frac{2\sigma \cos \theta}{R} \quad (7)$$

where σ is the interfacial tension between the fluids, θ is the contact angle measured across the densest phase, and R is the radius of the tube.

In a porous medium with a distribution of pore throat sizes, the capillary pressure is a function of the fluid saturation. This relationship, called the capillary pressure curve, is sometimes measured using mercury intrusion (MICP). It is important to note that the value of the capillary pressures measured by MICP are for the mercury-air system, where $\sigma = 485$ mN/m and $\theta = 130^\circ$. The Leverett J-function (Leverett, 1941) can be used to scale the capillary pressure curve obtained with one fluid pair to another or from a one rock to another, as long as the pore structure between the two rocks is similar. For example, one could use this relationship to scale the P_C curve between two Berea sandstones with different permeabilities and porosities. The Leverett J-function is defined as:

$$J(S_w) = \frac{P_C(S_w)}{\sigma \cos \theta} \sqrt{k/\phi} \quad (8)$$

where σ is the interfacial tension, θ is the contact angle, and ϕ is the porosity.

An example of a J-function for Berea sandstone (Pentland, 2011) is shown below:

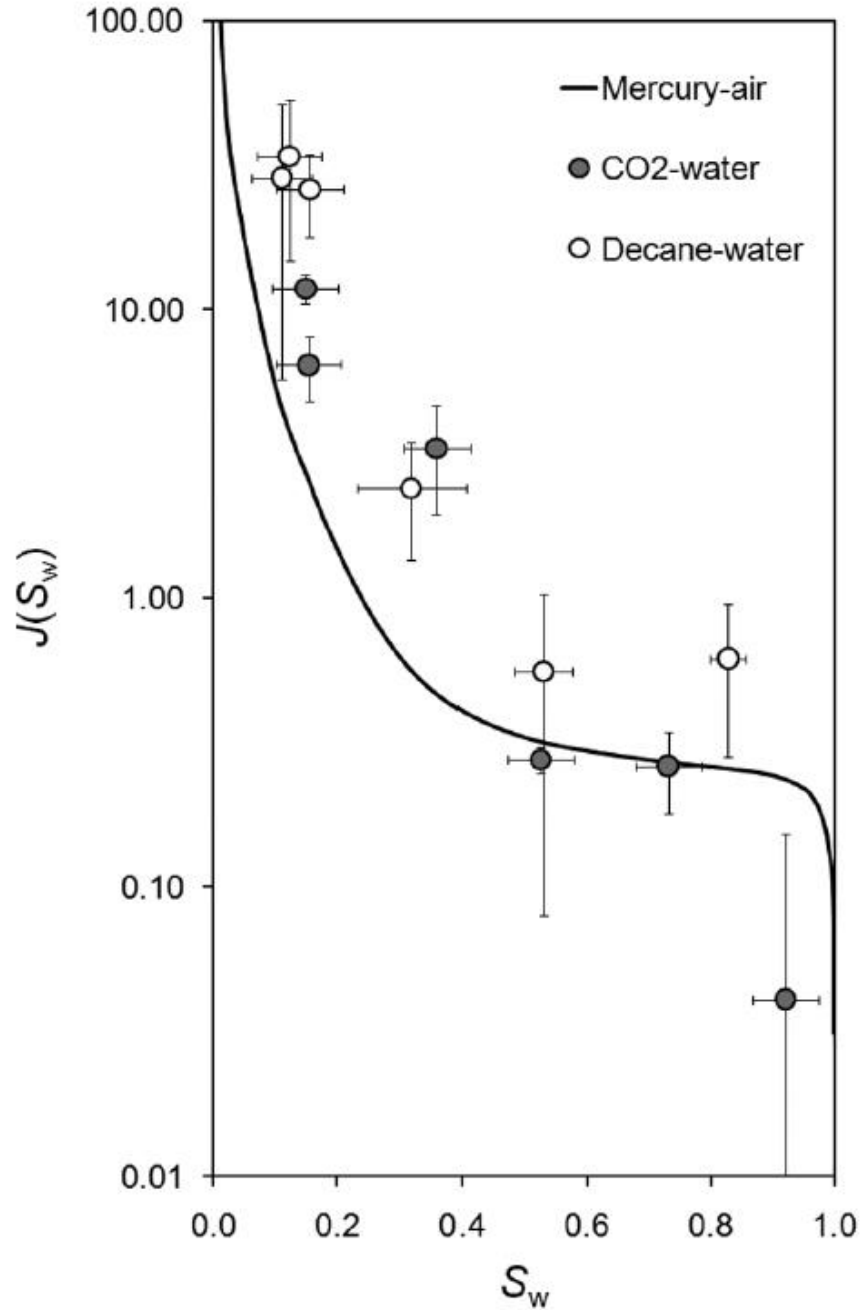


Figure 2-2: Berea sandstone capillary pressures and Leverett J-function (Pentland, 2011).

Example capillary pressure curves (Pini and Benson, 2013) at 50 C for N₂ and CO₂ at 348 psi and for CO₂ at 1305 psi in Berea sandstone are shown in Figure 2-3.

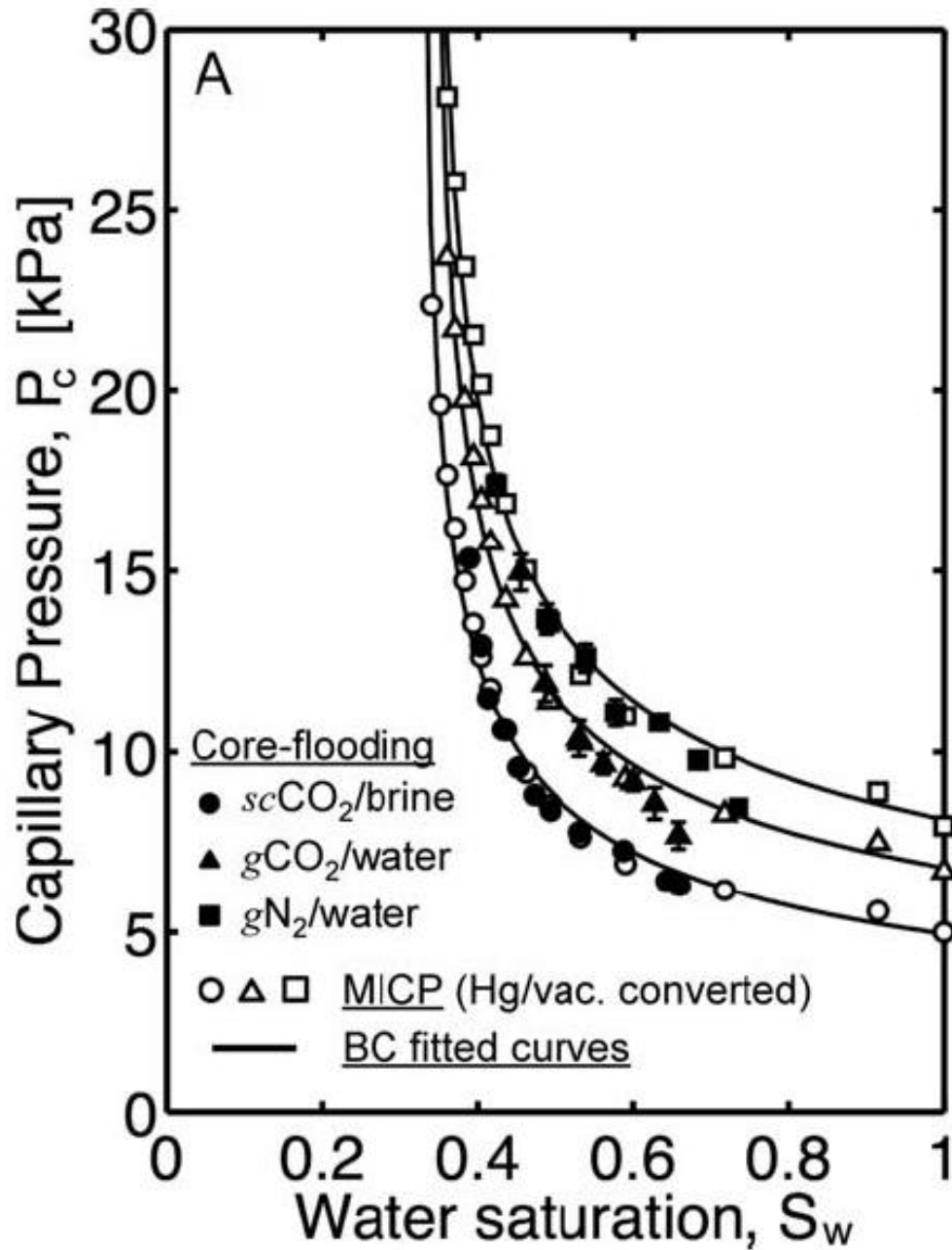


Figure 2-3: Berea sandstone capillary pressure curves (Pini and Benson, 2013).

2.3.1 Capillary End Effect

When two phases are injected into a core until steady state is reached, the saturations may not be uniform near the boundary between the rock and the end piece due to capillary pressure. This is called a capillary end effect. Continuity of phase pressures across the boundary requires the fluid saturations to be different than the steady state saturations away from the boundary. The goal of a well-designed experiment to measure relative permeability is to minimize this end effect. Alternatively, if the core is long enough and saturations are measured in the interior of the core, e.g. by X-ray imaging, and pressure drop measured using interior pressure ports, then the relative permeability can be determined from such data that are not subject to an end effect. In this work, interior saturations were not measured, so it was important to minimize the end effect.

Rapoport and Leas (1953) studied the capillary end effect in cores and developed a scaling group to determine when this end effect would be significant. The Rapoport-Leas number (N_{RL}) is defined as follows:

$$N_{RL} = \frac{L\mu q}{A} \quad (9)$$

where L is the core length, μ is the displacing fluid viscosity, and q is the volumetric flow rate of the displacing fluid, and A is the cross-sectional area of the core. A modified Rapoport-Leas number (N_{RL}^{mod}) is used for two-phase flow, defined as follows:

$$N_{RL}^{mod} = \frac{L\mu q}{Ak_{rnw}} \quad (10)$$

They found that the Rapoport-Leas number needed to be greater than 3 $\text{cm}^2 \cdot \text{cP}/\text{min}$ for end effects to be small. Note that the Rapoport-Leas number is not non-dimensional so the units matter. It is better to define a non-dimensional number such as defined in Lake (1989). The capillary end effect can be minimized by ensuring that the viscous force upon the fluid is higher than the capillary force. Thus, the capillary end effect can be reduced if the ratio of $\Delta P/P_c$ is considerably larger than one. A high Rapoport-Leas number corresponds to a high ratio of pressure drop to capillary pressure. The pressure drop exceeded the estimated capillary pressure at residual brine saturation by about an order of magnitude for the endpoint relative permeability experiments done as part of this study.

2.3.2 Capillary Number

Brownell and Katz (1947) and numerous other investigators have used the capillary number to correlate residual saturations in porous media. They used the following definition of capillary number:

$$N_c = \frac{k_w \Delta P}{L \sigma} \quad (11)$$

where k_w is the brine permeability at 100% brine saturation, ΔP is the pressure drop across the core, L is the core length, and σ is the interfacial tension between the two phases. The fundamental principle is that the pressure gradient must exceed the capillary pressure in the pore throat where the oil is trapped, so the original definition by Brownell and Katz makes sense. However, many other definitions can be found in the literature (Lake, 1989).

Chatzis and Morrow (1984) measured the capillary desaturation curve for Berea sandstone and found that the critical capillary number required to mobilize oil was on the order of 10^{-5} based on the following definition of capillary number:

$$N_c = \frac{u \mu_w}{\sigma} \quad (12)$$

where u is Darcy velocity and is μ_w the brine viscosity.

In this research, the flow rates were chosen to ensure that the capillary number remained below its critical value, i.e. no decrease in the residual saturation.

2.4 COREY-TYPE CURVES

Brooks and Corey (1964) developed a set of equations to describe the relative permeability behavior of two fluids in porous media. Similar equations were used to fit the relative permeability data. The equation used to fit the drainage data is:

$$k_{rw} = \left(\frac{S_w - S_{wr}}{1 - S_{wr}} \right)^{n_w} \quad (13)$$

where k_{rw} is the brine (assumed wetting phase) relative permeability, S_w is the brine saturation, S_{wr} is the brine residual saturation, and n_w is the brine exponent. For the non-wetting phases (gas or oil), a similar equation was used:

$$k_{rnw} = k_{rnw}^o \left(\frac{1 - S_w}{1 - S_{wr}} \right)^{n_{nw}} \quad (14)$$

where k_{rnw} is the non-wetting phase relative permeability, k_{rnw}^o is the endpoint relative permeability for the non-wetting phase, and n_{nw} is the non-wetting phase drainage exponent.

The imbibition equations used in this research are listed below:

$$k_{rw} = k_{rw}^o \left(\frac{S_w - S_{wr}}{1 - S_{nwr} - S_{wr}} \right)^{m_w} \quad (15)$$

where S_{nwr} is the non-wetting phase residual saturation, k_{rnw}^o is the endpoint relative permeability for the wetting phase, and m_w is the wetting phase imbibition Corey exponent.

$$k_{rnw} = k_{rnw}^o \left(\frac{1 - S_{nwr} - S_w}{1 - S_{nwr} - S_{wr}} \right)^{m_{nw}} \quad (16)$$

where m_{nw} is the non-wetting phase imbibition Corey exponent.

The relative permeability endpoints, residual saturations, and exponents are the parameters used to quantitatively compare the relative permeability data sets. These parameters were determined by fitting the relative permeability data using a weighted least squares method. The sum of the relative differences between measured data and the calculated values was minimized where the relative difference is defined as follows:

$$\Delta = \left(\frac{k_{r,c} - k_r}{k_r} \right)^2 \quad (17)$$

where k_r is the relative permeability data point, $k_{r,c}$ is the calculated relative permeability, and Δ is the relative difference.

Chapter 3 – Materials and Methods

The purpose of this chapter is to introduce the experimental materials and methods that were used to conduct the two-phase relative permeability experiments.

Multiple two-phase corefloods of varying injection rates of brine and gas or oil were performed to measure steady state two-phase relative permeability data. A major portion of this research was to set up the apparatus and work out a suitable procedure for accurate measurements. Extensive trouble shooting and refinements in the experimental procedure were required to make these measurements.

3.1 ROCK

Berea sandstone was used for the relative permeability experiments. The 1-7/8 inch diameter sandstone core was dried in a 90 C oven until the weight remained constant over a period of a few hours. Once dry, the mass and core dimensions were measured. Then the core was wrapped in heat-shrink Teflon, followed by a continuous aluminum foil four layers thick (to reduce CO₂ permeation through the Teflon layers), and then another layer of heat-shrink Teflon.

Table 3-1: Berea sandstone core properties.

dry mass	1126	grams
length	29.57	cm
diameter	4.699	cm
bulk volume	512.8	mL
pore volume	87.09	mL
porosity	16.98	%
brine permeability	68.28	mD

The following images show the appearance of the core at the beginning of the research:



Figure 3-1: Berea sandstone core after drying.



Figure 3-2: Core after wrapping with Teflon and aluminum foil.

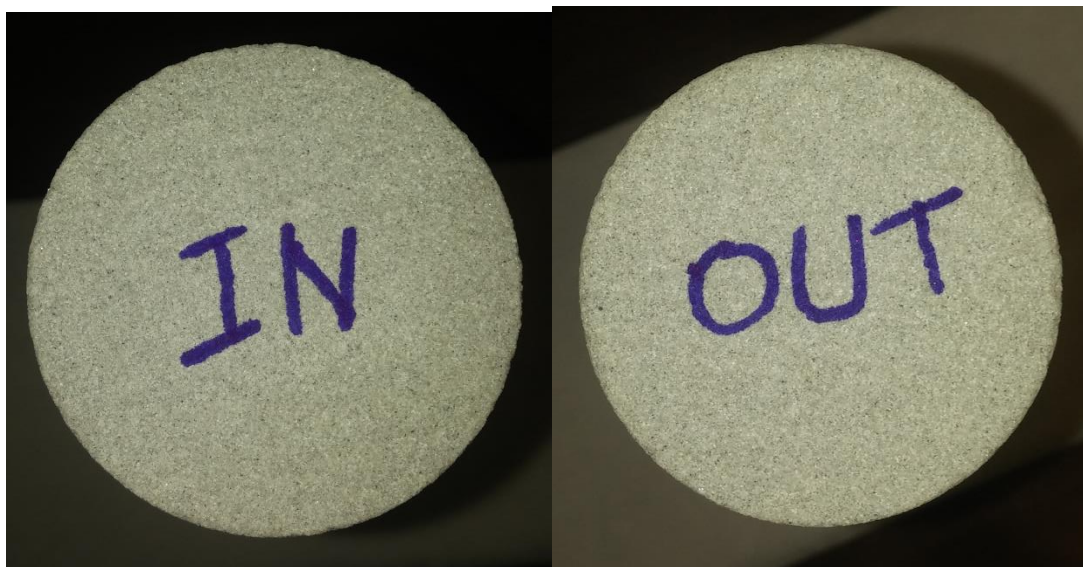


Figure 3-3: Inlet and outlet faces of core.

The following images show the appearance of the core during the course of the research:



Figure 3-4: Appearance of overall core after five months of flooding.



Figure 3-5: Appearance of inlet and outlet faces of core after five months of flooding.



Figure 3-6: Appearance of core after eight months of flooding.



Figure 3-7: Appearance of inlet and outlet faces of core after eight months of flooding.

These images clearly show evidence of iron on the faces of the core. The dissolution of carbon dioxide in the brine lowers its pH. It seems likely that the acidic brine dissolved iron from the core and that the rust color on the faces of the core are due to iron precipitation under atmospheric conditions.

3.2 FLUIDS

3.2.1 Brines

The initial brine consisted of 3 wt% NaCl and 0.1 wt% CaCl₂ brine (referred to as 3 wt% brine) and the tracer brine consisted of 6 wt% NaCl with 0.2 wt% CaCl₂ brine (referred to as 6 wt% brine). The main purpose of these salts was to prevent clay swelling and dispersion in the Berea sandstone that would be expected to occur at low salinity and hardness. The salinity of effluent brine was measured using a refractometer. This is a convenient way to use salinity as a brine tracer.

The brines were prepared by weighing the appropriate amount of salts in a plastic jug and then adding enough de-ionized water to bring the solution mass to 4 kilograms. The solution was shaken, the salt was allowed to fully dissolve, and the solution was vacuum filtered through a 0.45 μm membrane to remove any possible debris.

For CO₂ flooding, the brines were initially pressurized with an excess amount of CO₂. The equilibrium solubility of CO₂ in 3 wt% brine at 40 C and 1800 psi is approximately 0.0198 mole fraction CO₂ or 49.35 grams CO₂ per kg 3 wt% brine (Bando et al., 2003). Roughly double this amount of CO₂ was used to pressurize the brine-filled accumulators before they were rocked (to aid gas dissolution) and placed into the oven overnight for heating and equilibration to pressures above 1900 psi.

After equilibrium was indicated by a constant pressure within the accumulator, the excess CO₂ was slowly vented from the top of the accumulator while pumping water into the water-side of the accumulator, displacing the gas cap. A back-pressure regulator (set to about 1750 psi for the 1900 psi flooding and set to 1150 psi for the 1200 psi flooding) was used to maintain pressure on the brine while venting excess CO₂. The regulator pressure was slightly below the flooding pressure to prevent free gas from forming in the core. Once liquid began flowing from the back-pressure regulator, the

excess gas was assumed to have been removed from the accumulator and the CO₂-saturated brine was ready for injection into the core.

Table 3-2 lists the estimated brine properties at 40 C and Table 3-3 lists the estimated brine properties at 70 C. The brine density was considered independent of pressure and brine viscosity was interpolated from literature data at 1450 psi (Kestin et al., 1981):

Table 3-2: Brine properties at 40 C.

Brine wt%	Density (g/mL)	Viscosity (cP)
3	1.023	0.687
6	1.054	0.723

Table 3-3: Brine properties at 70 C.

Brine wt%	Density (g/mL)	Viscosity (cP)
3	1.009	0.431
6	1.040	0.455

3.2.2 Carbon Dioxide

The CO₂ used in this research was supplied by Praxair Inc. and was 99.5% pure. At 1800 psi (12.4 MPa) and 40 C, the mole fraction of water in CO₂ is approximately 0.0045 (Sabirzyanov, 2002), which is approximately 1.3 mL water for every liter of supercritical CO₂. Therefore, to ensure the CO₂ was fully saturated with water, 20 mL of 3 wt% brine was added to the accumulators for every liter of CO₂. The properties of pure CO₂ at 40 C are given in Table 3-4 (NIST, 2016):

Table 3-4: CO₂ properties at 40 C.

CO ₂ Pressure (psi)	Density (g/mL)	Viscosity (cP)
1200	0.314	0.0240
1900	0.745	0.0624

3.2.3 Nitrogen

N₂ gas was supplied by Praxair Inc. at 6000 psi and was 99.999% pure. During flooding, the N₂ was bubbled through approximately 500 mL of 3 wt% brine to saturate it with water vapor before injection into the core. This ‘bubbling unit’ was a 1.5 liter capacity accumulator, allowing for 1 liter of gas space within the unit. Also, the bubbling unit was kept in the oven and served as a heater, bringing the N₂ stream from room temperature to oven temperature (40 C) as it passed through the brine and diffused throughout the accumulator gas space. At peak flow rate (1450 grams N₂/hour or 184.9 mL/minute at 1800 psi and 40 C), the residence time of the gas within the bubbling unit was 5.4 minutes, allowing enough time for the N₂ to warm to 40 C before injection into the core. The properties of pure N₂ are given in Table 3-5 (NIST, 2016):

Table 3-5: N₂ properties at 40 C.

N ₂ Pressure (psi)	Density (g/mL)	Viscosity (cP)
1800	0.131	0.0210

3.2.4 Oil

99+% pure n-decane was supplied by ThermoFisher Scientific. The n-decane properties at 70 C are given in Table 3-6 (from NIST). The n-decane was not equilibrated with brine before injection.

Table 3-6: n-decane properties at 70 C.

C ₁₀ H ₂₂ Pressure (psi)	Density (g/mL)	Viscosity (cP)
1500	0.702	0.549

Naphthalene was used as an oil tracer. 99% pure naphthalene was supplied by ThermoFisher Scientific. The naphthalene concentration in effluent samples was measured using ultraviolet (UV) absorbance. Naphthalene is readily detected via UV spectroscopy. Naphthalene dissolved in n-decane appears as a distinct peak at 311 nm wavelength within the absorbance spectrum, as shown in Figure 3-8 for a naphthalene concentration of 614.24 ppm:

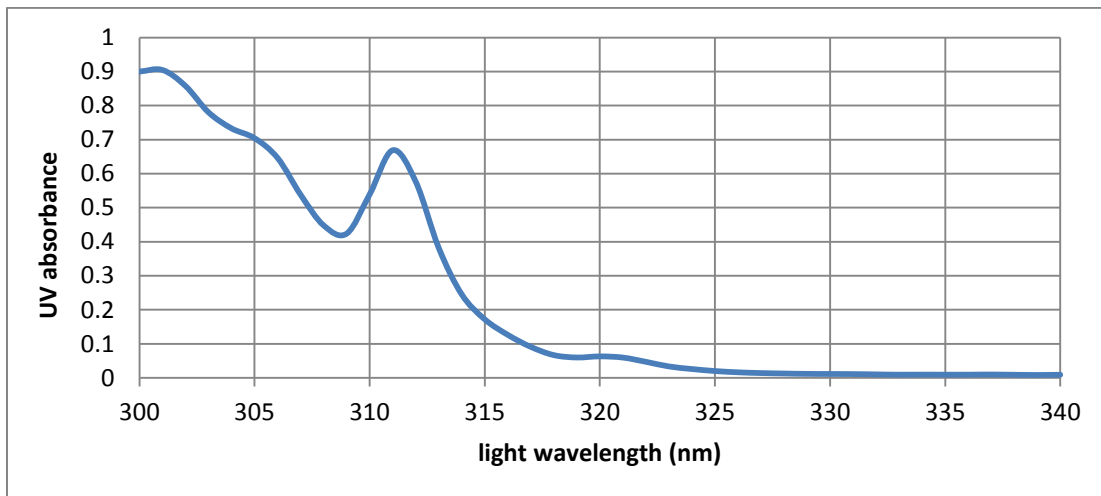


Figure 3-8: UV absorbance of 614.24 ppm naphthalene in n-decane.

The absorbance was measured between 300 nm and 340 nm to allow for troubleshooting via absorbance curve analysis, such as a possibly contaminated solution or faulty cuvettes. Absorbance below 300 nm was not performed due to the use of plastic visible-light cuvettes that begin to absorb near this wavelength (Brandt, 2010), as seen in Figure 3-9:

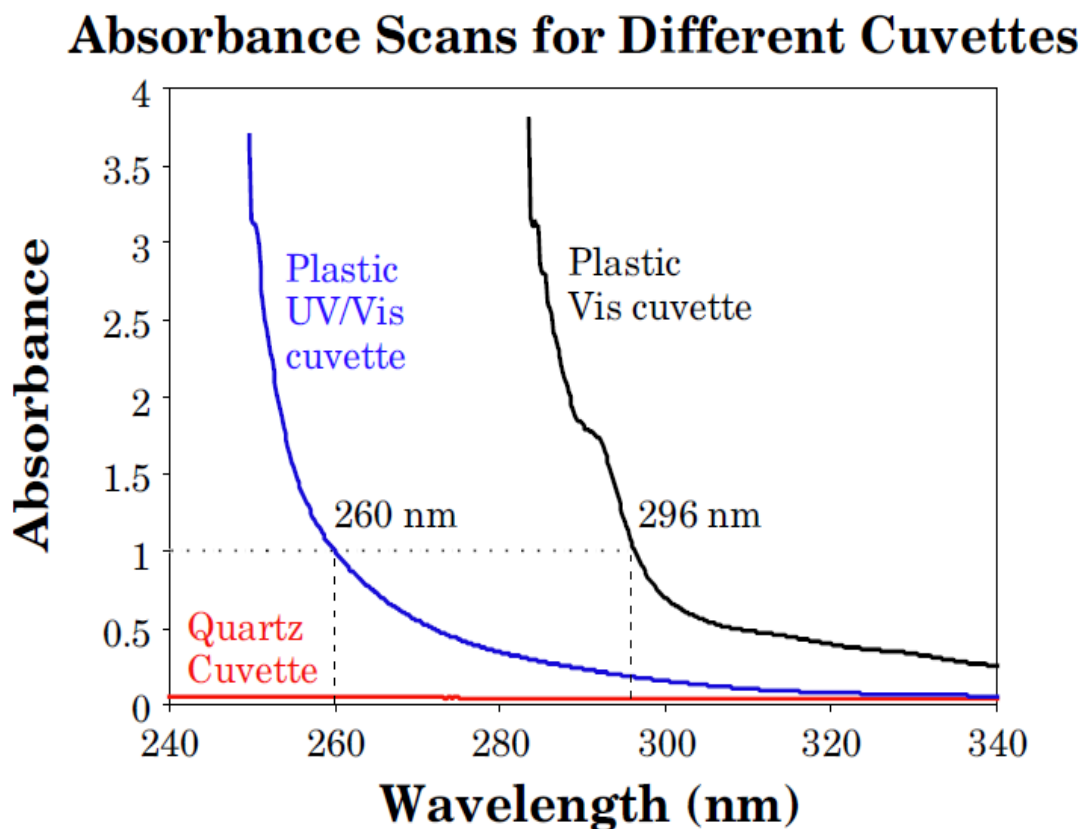


Figure 3-9: Comparisons of light absorbance of different cuvette materials.

As the naphthalene concentration increases, the solution has a higher UV absorbance at the 311 nm peak. The relationship between UV absorbance (B) at 311 nm and naphthalene concentration in n-decane (C_N) as parts per million (ppm) is shown below in equation 18 and Figure 3-10:

$$\frac{B - 0.0241}{0.001} = C_N \quad (18)$$

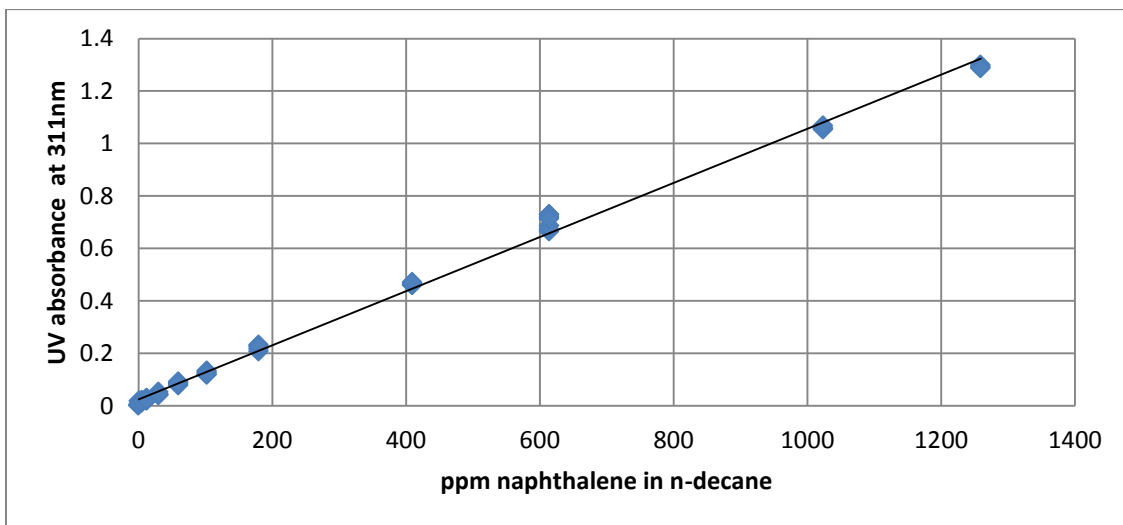


Figure 3-10: UV absorbance versus concentration of naphthalene in n-decane.

Naphthalene will dissolve into 3.5 wt% brine at a maximum concentration of 22.8 ppm at 25 C (Haynes, 2016). Compared to the concentrations used in the oil tracers (0 to 1200 ppm), this partitioning of naphthalene into brine is negligible.

3.2.5 Interfacial Tension

Interfacial tension data from the literature are given in Tables 3-7 to 3-9:

Table 3-7: Interfacial Tension between Brine and CO₂.

Brine NaCl wt%	Temperature (°C)	Pressure (psi)	Interfacial Tension (mN/m)	Source
7.578	41	1160	32.7	Bachu, 2009
7.578	41	1740	25.5	Bachu, 2009
0.5	59.85	1886	38.7	Al-Yaseri, 2015

Table 3-8: Interfacial Tension between Brine and N₂.

Brine NaCl wt%	Temperature (°C)	Pressure (psi)	Interfacial Tension (mN/m)	Source
0.5	59.85	1886	60.5	Al-Yaseri, 2015
0	40	1450	65.1	Yan, 2001
0	40	2176	63.3	Yan, 2001

Table 3-9: Interfacial Tension between Brine and n-decane.

Brine NaCl wt%	Temperature (°C)	Pressure (psi)	Interfacial Tension (mN/m)	Source
5.17	50	1630	51.3	Bi-Yu Cai, 1996

3.3 APPARATUS

Figures 3-11 to 3-14 show a schematic of the flow apparatus. A Phoenix Instruments© stainless-steel two-inch diameter core holder rated to 10,000 psi and 300 °F was used for all coreflood experiments. A mass balance was connected to the control computer for pressure and effluent mass data collection. Taps along the length of the core holder provided pressure communication between the core and a series of calibrated Rosemount® 4-20 mA pressure transducers connected to the control computer. Hydraulic pressure communication from the transducers to the core was created by drilling through the Teflon and aluminum foil layers with a 1/16 inch drill-bit. The taps were located at the following lengths along the core holder, starting from the inlet:

Table 3-10: Pressure tap locations along core

Pressure Tap	Distance from Core Inlet (cm)
1	6.75
2	14.37
3	21.99

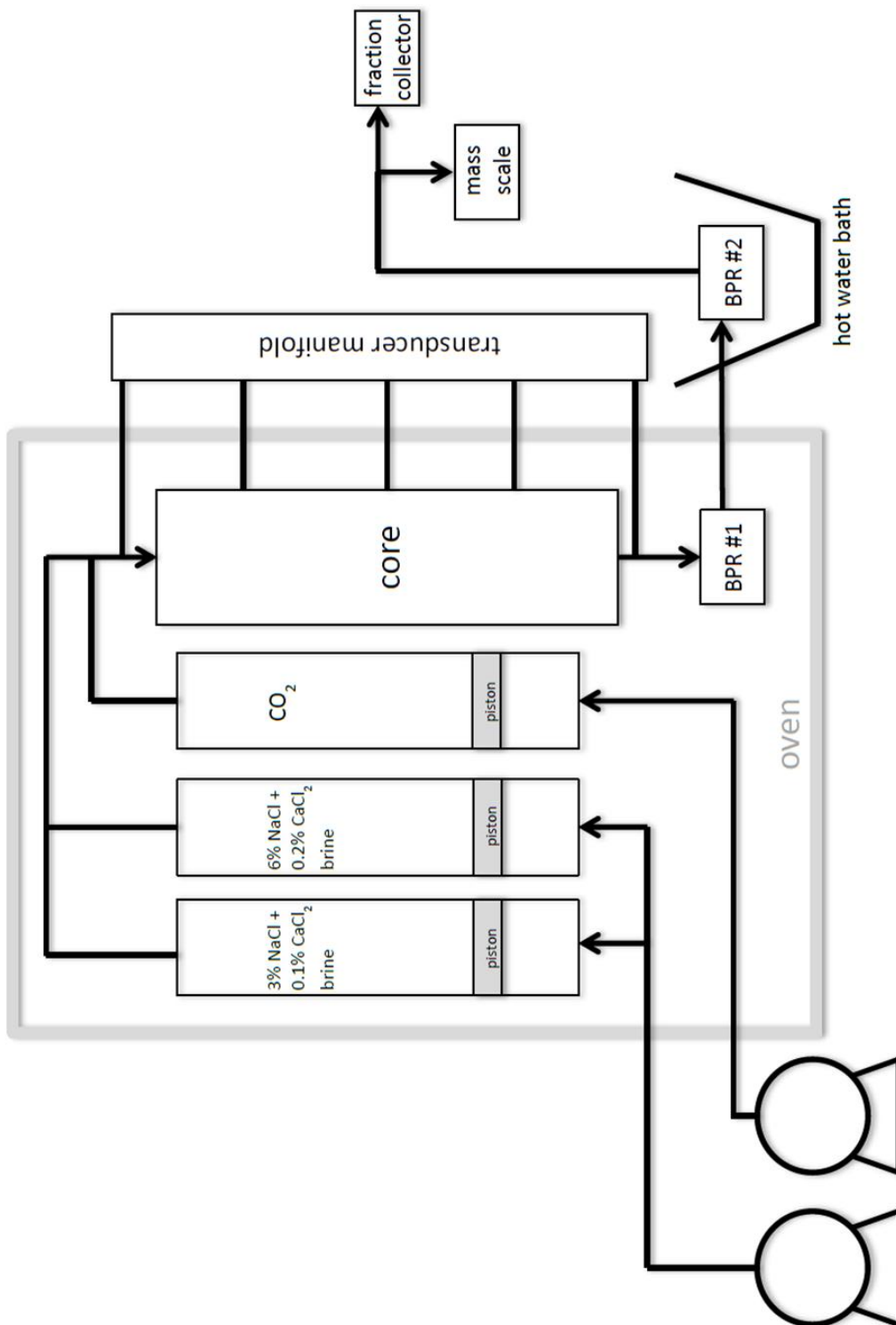


Figure 3-11: Flow Diagram for CO₂ and brine floods.

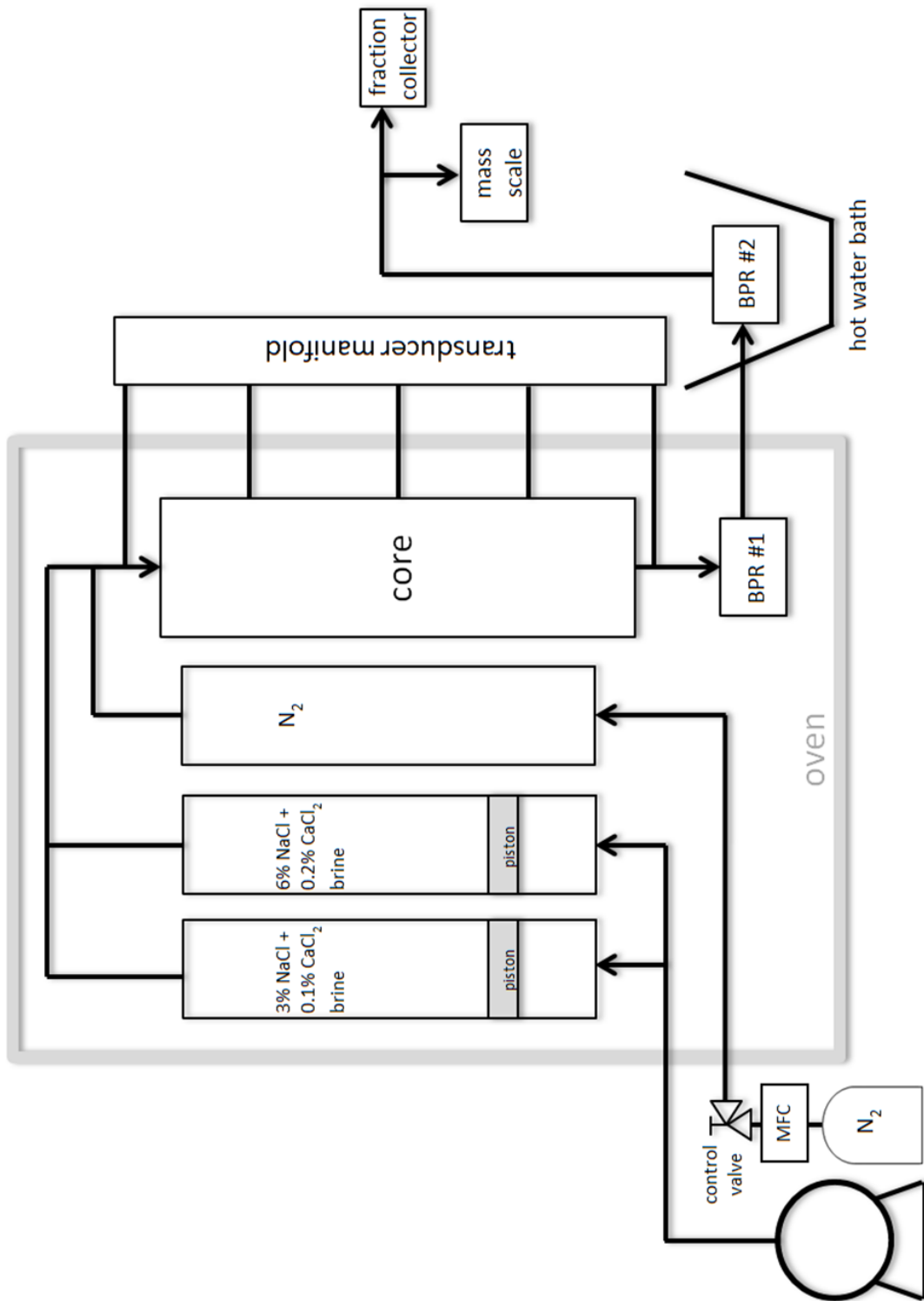


Figure 3-12: Flow Diagram for N₂ and brine floods.

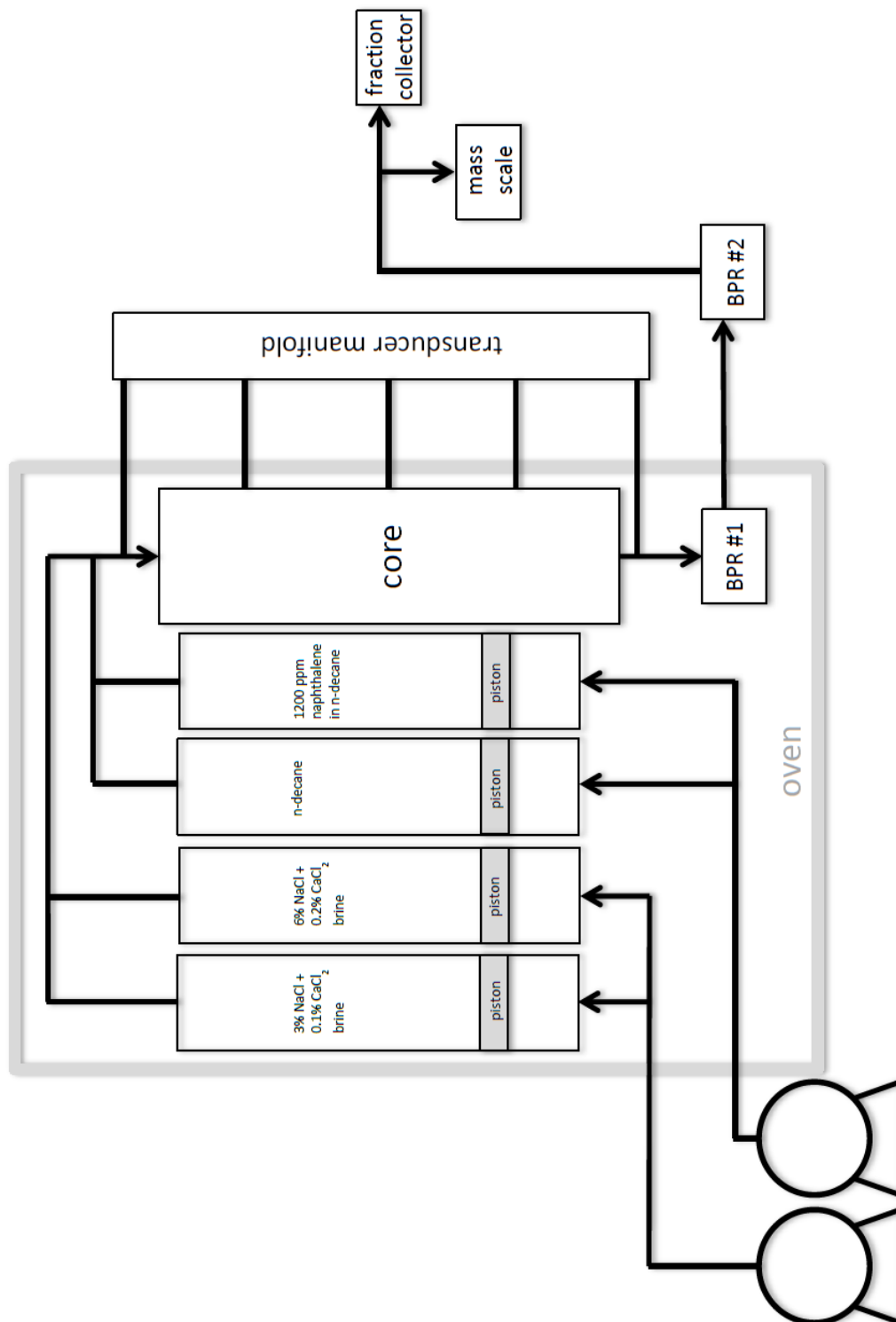


Figure 3-13: Flow Diagram for Oil and Brine floods.

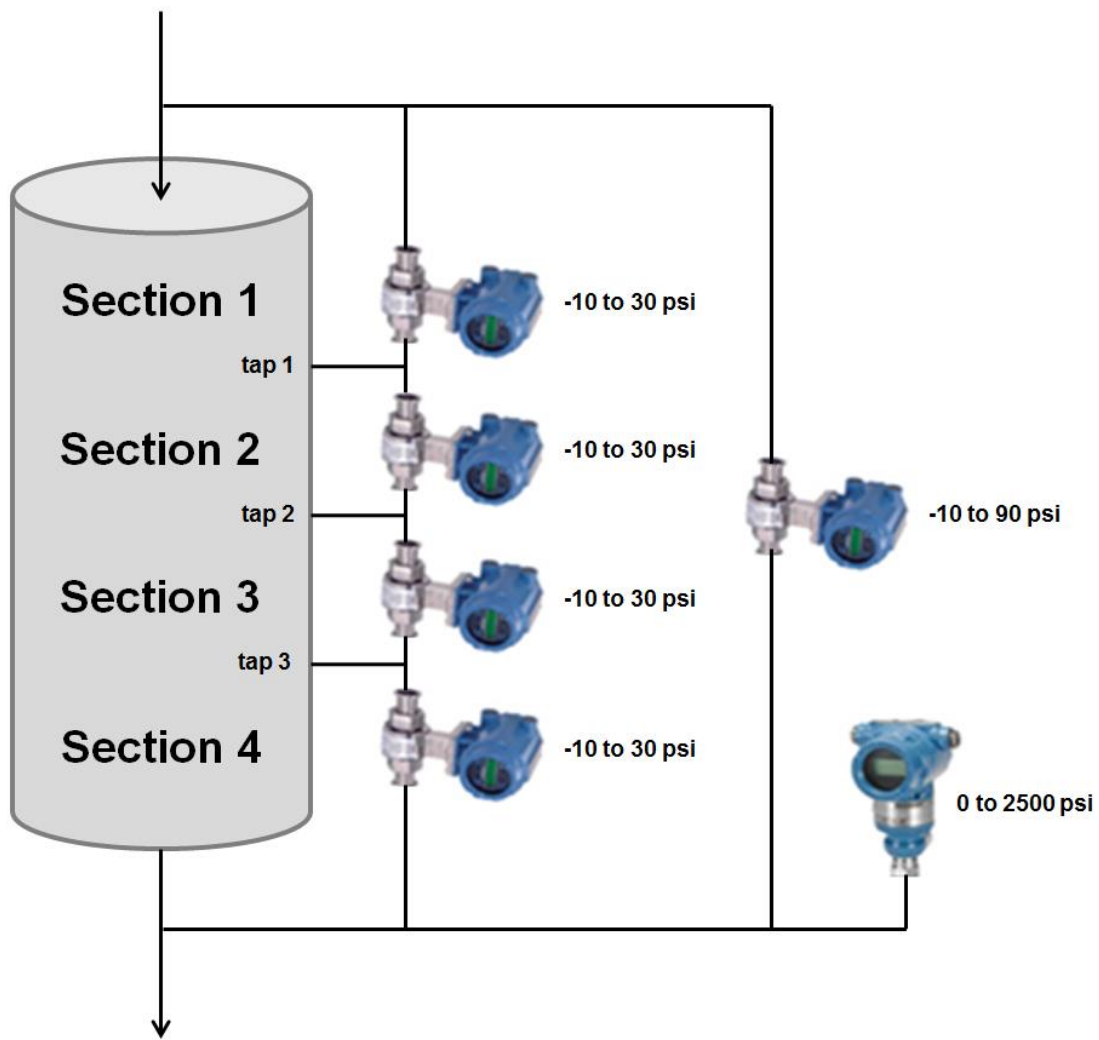


Figure 3-14: Pressure transducer manifold.

3.3.1 Pumps

The pumps used in this research were Chandler Engineering© Quizix QX pumps each capable of pressures up to 6000 psi and flow rates up to 50 mL/minute. The pumps had two modes: constant pressure delivery or constant flow rate mode that would deliver a continuous flow of water using two pumping cylinders. Tap water was used as the pump fluid. Two pumps were used to pump into a single accumulator at rates above 50 mL per minute.

3.3.2 Mass Flow Controller

The N₂ flow rate was regulated via a mass flow controller (MFC) linked to a control valve. The MFC was a Bronkhorst® mini Cori-Flow™ unit that measured the process fluid flow rate (independent of fluid properties) based on the Coriolis effect. This flow rate measurement was input into PID control software that manipulated the shop-air pressure supply to the control valve. The shop-air pressure actuated the control valve a specified amount, changing the discharge orifice within the valve and thus the gas flow rate.

The control valve was a RESEARCH CONTROL® valve built by BadgerMeter, Inc. Two separate control valves, of differing control orifice sizes, were procured for this research because of the varying gas flow rates used in the floods.

The MFC was calibrated at the factory but additional checks were performed to ensure its accuracy. Specifically, N₂ was flowed through the MFC, control valve, and into the top of a deionized-water-filled accumulator. The accumulator water was held at pressure by a back-pressure regulator (approximately 1800 psi), allowing the gas to flow into the accumulator and displace the water at a known pressure and at room temperature. This displaced water was measured using a mass balance connected to the control computer, thus recording the mass flow rate of the water and allowing the volumetric

flow rate of the N₂ into the accumulator to be calculated. This testing showed that the MFC and control valve performed as expected and that the N₂ equation of state used to prescribe the mass and volumetric flow rates was accurate. The MFC mass flow rate was used to regulate the volumetric flow rate of the N₂ into the core using the core inlet pressure.

3.3.3 Back Pressure Regulators

Equilibar® H3P-model back pressure regulators (BPRs) were used in this research for their corrosion resistance and multi-phase flow pressure control ability. They were composed of a stainless steel body with a polyether-ether-ketone diaphragm that was pressurized with nitrogen gas from a high pressure laboratory nitrogen cylinder.

The produced fluids were depressurized in stages across BPR#1 (from 1800 psi to approximately 1500 psi for the higher pressure experiments, or 1200 psi to approximately 1100 psi for the lower pressure experiments) and then across BPR#2 (approximately 1500 psi to ambient, or approximately 1100 psi to ambient). The intermediate pressure was set close to the core pressure to minimize the temperature change within BPR#1. Consequently, the pressure control for BPR#1 was more stable with BPR#2 downstream than it was without it.

3.3.4 Dead Volumes

The precise volume of each fluid within the inlet and effluent tubing, filters, BPRs, and other connections (referred to as the dead volume) is needed for an accurate saturation measurement. During gas flooding, the dead volume for each fluid was determined by calculating the fractional flow of the fluid at the three different pressures of the apparatus. Using CO₂ or N₂ equations of state, the density of the gas can be calculated for each pressure segment of the apparatus. Brine was assumed to have the

same compressibility as water and thus the density at each pressure was calculated. The temperature in the tubing was assumed to be constant.

Assuming a constant mass flow through all tubing, the volumetric flow rate of each fluid can be determined within each pressure segment. Each fluid's fraction of its particular volumetric flow rate within the overall volumetric flow rate equates to its fractional flow at that pressure. Additionally, during CO₂ flooding, the brine releases dissolved CO₂ as it depressurizes, adding to the gas flow rate. N₂ dissolves into brine in such small amounts that N₂ dissolution into and effervescence out of the brine was neglected. The brine dead volume consists of the liquid fraction of the raw volume of each brine-containing tubing segment. This particular value is used for each specific fractional flow brine tracer.

During oil flooding, the fractional flow of brine and oil in all segments was considered constant. The fractional flow of each fluid was used to determine its dead volume. Pressure-dependent volume changes of the liquids were neglected.

3.3.5 Sample Collection

Effluent fluid samples were collected in either a Teledyne Isco© RETRIEVER® 500 fractional collector or an apparatus constructed in the laboratory. The fractional collector is a device that sequentially moves, on a time basis, disposable 15 mL capacity centrifuge collection tubes into position to collect the effluent fluids coming from the end of the setup tubing.

During floods with a significant fractional flow of gas, the fractional collector was unable to catch all of the liquid splashing into the tubes, due to rapid depressurized gas flow, and thus the liquid volumes were not accurate. Therefore, for gas flooding, a lab-constructed device was used. The device consisted of a three-way valve that directed the

effluent stream into collection tubes while allowing the gas to escape to the room, thus ensuring the liquid was collected in the tubes. The effluent flow direction (between the two collection tube slots) was chosen by a hand-operated three-way valve. At that time, the filled collection tube was collected and replaced with a dry collection tube. In this manner, all liquid effluent was able to be collected for tracer and saturation measurements.

3.3.6 Residual Water Saturation Measurement

When flooding with only gas, a brine tracer could not be used due to zero brine flow. Instead, the mass of the effluent was measured using a mass balance during the final drainage flood and also during the first imbibition flood. During the last drainage flood, the final mass of the expelled brine was considered to be the brine saturation change of the core. Additionally, after steady-state was achieved during the first imbibition flood, an instantaneous measurement of the difference between total brine pumped into the core and total brine effluent collected gave the change in amount of brine within the core (after correcting for dead volumes). These dual measurements were analyzed and compared to determine the residual water saturation.

3.3.7 Ultraviolet Spectrophotometer

For oil tracer analysis an Agilent Technologies Cary 100® UV-Visible spectrophotometer was used. The spectrophotometer was calibrated to samples of pure n-decane in BrandTech® semi-micro methacrylate spectrophotometry cuvettes. Oil tracer samples of unknown naphthalene concentration were loaded into semi-micro cuvettes and placed into the spectrophotometer to measure the absorbance.

3.4 TROUBLESHOOTING

3.4.1 Carbon Dioxide Absorption and Attack

Supercritical CO₂ absorbs into rubber and reduces its integrity. The core holder was equipped with a Viton® rubber sleeve that was used to apply a confining pressure of 3000 psi on the core. This sleeve allowed fluid pressure communication from the core holder taps to the rock surface via pressure ports. These pressure ports were composed of stainless steel taps embedded within the rubber sleeve.

During CO₂ flooding, some anomalies were noted in the pressure data. It was discovered that the pressure ports were plugged and not allowing pressure communication. Re-drilling through the core holder taps and into the rock allowed core fluids to again communicate with the transducer manifold. Cuttings from the drill-bit were mostly black rubber with minor pieces of Teflon and aluminum foil. This indicated that the port was plugged by the rubber sleeve, which was assumed to be swelling and sealing off the pressure port due to supercritical CO₂ absorption into the rubber material during gas flooding, exacerbated by apparatus depressurizations. Wrapping the core in multiple aluminum foil layers was an attempt to limit CO₂ permeation into the rubber sleeve.

After repeated drillings of the plugged rubber sleeve pressure ports, the pressure response of the core improved but was not perfect. At the conclusion of the CO₂ floods, the rubber sleeve was replaced with a similar sleeve composed of AFLAS® rubber, which better resists CO₂ chemical attack than Viton®. Additionally, check valves used in the apparatus had Viton® seals which began to leak after high-pressure CO₂ exposure and pressure cycling. These check valves were replaced with identical models using AFLAS® seals instead of Viton® seals, with positive results.

CO₂ reacts with iron to produce iron carbonate, a black-colored corrosion product. Blackening was noted on any carbon-steel parts of the apparatus, i.e. the diaphragms of the initial carbon steel BPRs. A 2 μm filter for liquid and 0.5 μm filter for gas were placed upstream of the inlet of the core holder to remove corrosion products. Also, a 2 μm filter was placed downstream of the core, but upstream of the first BPR, in order to filter out particulates before reaching the BPRs. Such debris could cause the BPRs to not seal correctly, resulting in poor pressure management of the core.

3.4.2 O-Rings

Most of the elastomeric o-rings used in this research were composed of Viton® rubber, with some composed of Buna-N rubber. Elastomeric materials absorb gas when exposed to high-pressure gas for prolonged periods. When rapidly de-pressurized, the o-rings would suffer explosive decompression, disintegrate, and not contain pressure. Buna-N appeared to be more resistant to de-pressurization and CO₂ attack than Viton®. Both types of o-rings seemed to be affected more by high-pressure CO₂ than high-pressure N₂.

The affected o-rings (those that were subjected to rapid depressurization or exposed to high-pressure CO₂) were replaced, when possible, to ensure the components within the apparatus maintained pressure. During installation, the fresh o-rings were lightly greased with either DOW CORNING® high vacuum grease or a silicone-based o-ring lubricant. No difference in sealing performance was noted between the two lubricants.

3.4.3 Back Pressure Regulators

BPRs with carbon steel diaphragms were initially used for coreflood pressure control. Due to CO₂ corrosion and single-phase fluid design, these BPRs were not able to

maintain a steady pressure within the core during brine and CO₂ co-injection. The use of Viton® rubber diaphragms was attempted, but similar pressure control issues remained. Finally, Equilibar® BPRs composed of a stainless steel body with polyether-ether-ketone diaphragms were used. They resisted corrosion while producing stable pressure control during two-phase flow.

3.4.4 Transducer Manifold Gas Diffusion

The transducer manifold was initially filled and pressurized with deionized water, but switched to city tap water after a few months with no problems. During initial CO₂ flooding it was noted that if the setup was depressurized, some of the sectional pressure transducers would begin to produce erroneous data. Evidently, during CO₂ flooding, some gas would dissolve into the transducer manifold pressure media (water) and when the system was de-pressurized the CO₂ would effervesce out of the water within the manifold. This free gas in the manifold lines caused the erroneous pressure readings. This issue was partially resolved by keeping the manifold pressurized at all times during gas flooding. If the manifold lost pressure and thereafter produced unreliable data, it would be de-pressurized, purged with air, evacuated, re-filled with de-ionized water, re-pressurized, and tested.

3.4.5 Sectional Pressure Drops

The pressure transducers measure a pressure difference between two diaphragms. The sectional pressure measurements are altered when the CO₂ transport through the core, changing the pressure in each section in turn as each pressure tap encounters gas. This effect is exemplified in the pressure data of a test flood when CO₂ at 1800 psi was injected into a core filled with 3 wt% brine.

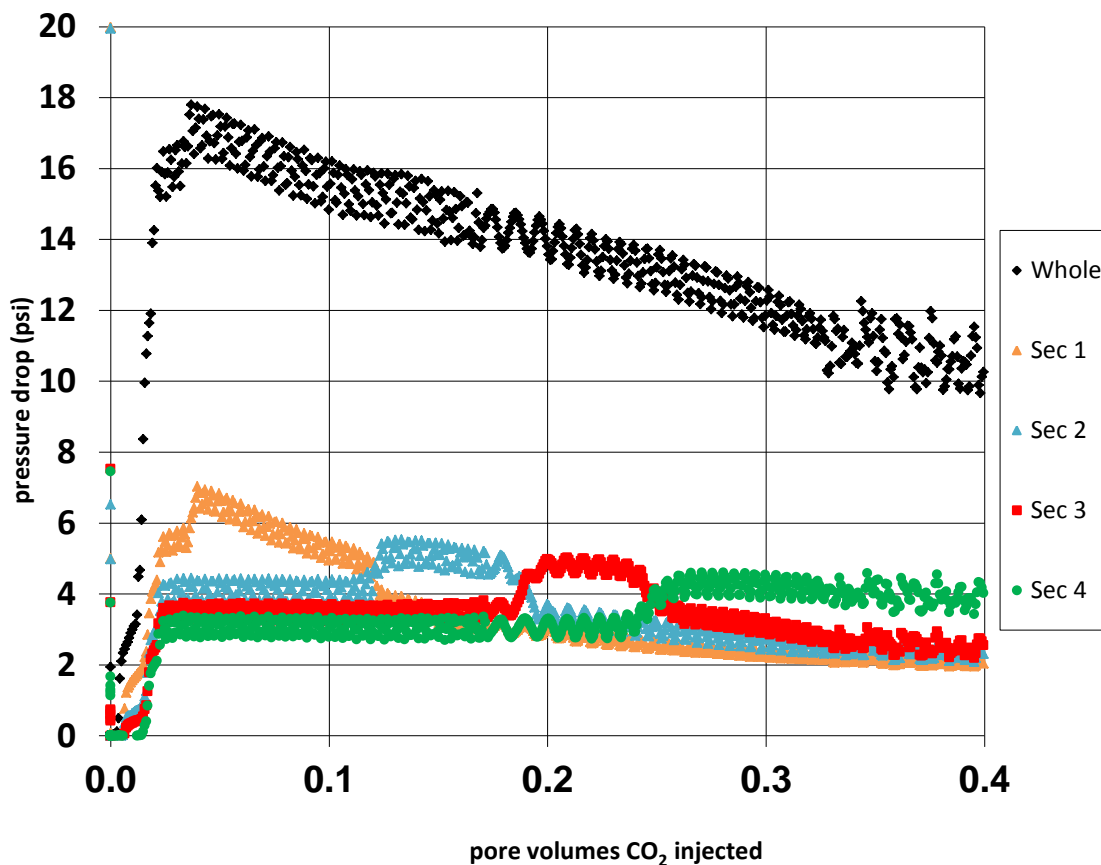


Figure 3-15: Pressure drop data measured during injection of CO₂ into core saturated with brine at 40 C and 1800 psi.

The CO₂ begins to affect the sectional pressure measurements at around 0.04 pore volumes of gas injected, starting with first section and affecting the sections in sequence. An increase in pressure drop of about 1 psi occurred when the gas reached each section, indicating a pressure difference across the phases (capillary pressure) of about 1 psi. This increase in pressure drop disappears when the gas reaches the next section because the pressure is now measured in the same phase for both the upstream and downstream sides of the transducer, so there is no effect of capillary pressure.

During a preliminary CO₂ injection test, the pressure data shown in Figure 3-16 was recorded and the flow was stopped at 93.4 minutes. The persistent pressure differences across some sections of the core may also be due to capillary pressure differences if different sides of the transducers sense pressures in different phases. However, whether this was the cause or something else caused the differences was not determined.

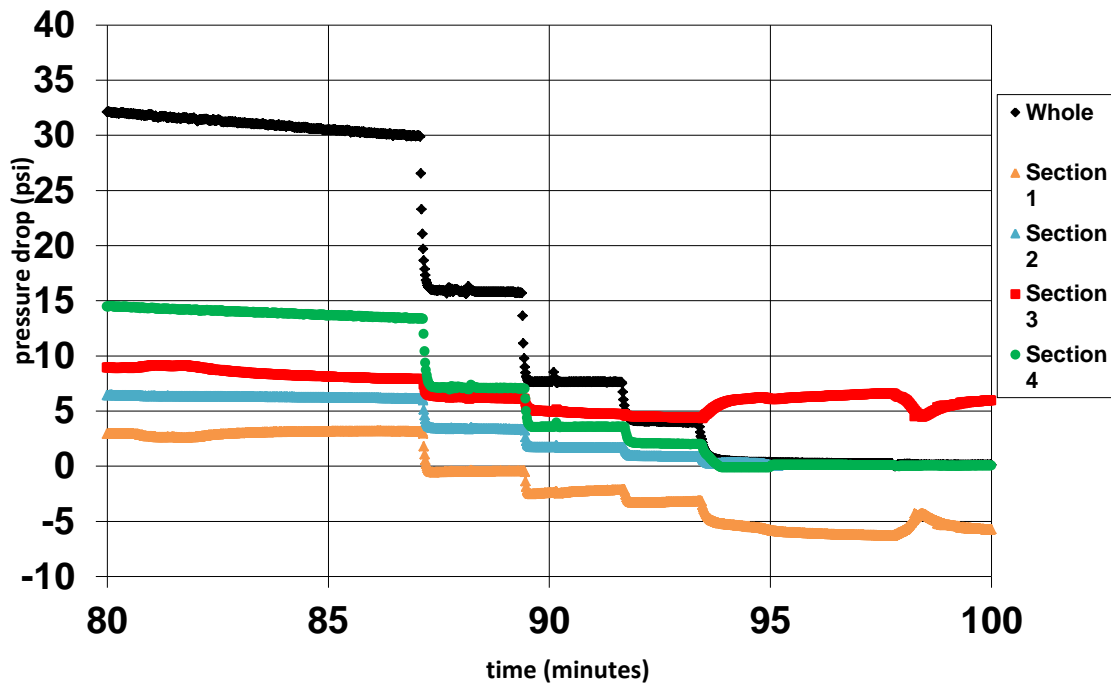


Figure 3-16: Pressure data after stopping injection of CO₂ at 40 C and 1800 psi.

At other times, sectional pressure drops became erratic as illustrated in the pressure data measured during the CO₂ flood to residual water shown in Figure 3-17.

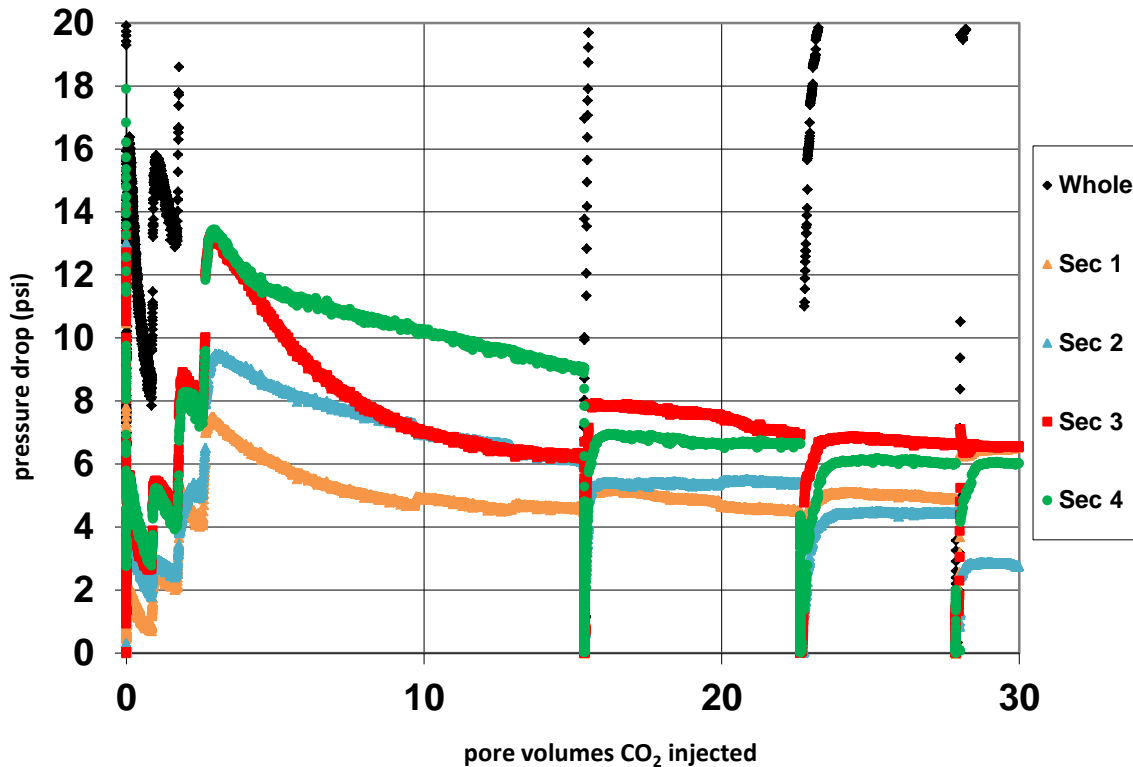


Figure 3-17: CO₂ flood to residual brine pressure drop data at 40 C and 1900 psi.

The sectional pressure drops switched their ordering (i.e. sections 3 and 4 at 15.5 pore volumes, sections 1 and 2 at 22.8 pore volumes) when the flood stopped to switch to a new accumulator of CO₂ (shown as the discontinuities of pressure drop data). Obviously the permeabilities of the sections cannot rapidly and abruptly change because the CO₂ is drawn from a new accumulator. One hypothesis is that during the time to change the accumulators, gas diffused into and throughout the transducer manifold, altering the differential pressure measurements. Another possible explanation is that

fluids within the core are rearranged by capillary forces during the downtime needed to change the accumulators. Therefore sectional permeability behavior was analyzed with these possible experimental complications in mind.

3.4.6 Joule-Thomson Effect

During preliminary gas floods, it was discovered that the effluent fluids coming from the core would freeze in the line immediately downstream of the single BPR in use at the time. These frozen plugs would cause an increase in pressure when the effluent line became blocked while the pumps continued to inject fluids. The freezing was caused by the Joule-Thomson effect when the CO₂ rapidly expanded from 1800 psi to atmospheric pressure.

This issue was resolved by adding a second BPR to the apparatus. For 1800 psi flooding, the second BPR was set to about 1500 psi and for 1200 psi flooding, the second BPR was set to about 1100 psi. The secondary BPR was placed into a water-filled metal bucket atop a thermometer-controlled hotplate which kept the water bath at 50 C for CO₂ floods and 40 C for N₂ floods (due to higher CO₂ Joule-Thomson cooling than N₂). The addition of the secondary BPR allowed for the gas to be depressurized in stages, resulting in the majority of the Joule-Thomson cooling to occur within the secondary BPR. This regulator was heated with a hot water bath so that even at high gas flow rates, the depressurization of the gas did not lower the temperature of the BPR and tubing to the freezing point.

3.4.7 Gas Compression Effects

When co-injection of gas and brine begins, the pumps begin pushing the CO₂ or the mass flow controller allows N₂ flow at their appropriate flow rate. As the core outlet fluids remain at BPR pressure and a differential pressure builds across the core, the pressure of the liquid upstream of the core increases without any significant delay, but the pressure of the gas upstream of the core does not increase quickly due to the compressibility of the gas. The upstream gas must ‘catch-up’ to the rising pressure of the core inlet fluids. If not accounted for, this would lead to only brine being injected into the core while the gas pressure gradually increased to the point where it will begin to be injected into the core. Also, the brine could also backflow through the gas inlet line and into the gas accumulator, leading to an unknown injection rate of the brine into the core. This was a significant issue related to avoiding the effects of saturation hysteresis.

This issue was resolved by carefully managing the flow rates of the injection. When beginning co-injection, the fluids would be slowly injected into the core while the gas injection pressure was carefully monitored to ensure proper pressurization and flow. In this fashion the injection rates of both gas and brine were carefully increased to the prescribed rates concurrently. Additionally, check valves were placed in the injection lines to prevent the higher-pressure fluid from back-flowing into the injection line for the other fluid in the event of a pressure differential between the injection fluids.

3.5 PROCEDURE FOR RELATIVE PERMEABILITY MEASUREMENTS

1. The prepared core was placed into the steel core-holder and 3000 psi of confining water pressure was applied, the setup was leak checked, and any known leaks were resolved. The core was evacuated for at least an hour and then 6 wt% brine was vacuum-imbibed. The pore volume was estimated from the amount of brine imbibed.
2. The room temperature core was then pressurized to 1900 psi with 6 wt% brine and the permeability was determined with 6 wt% brine at flow rates varying from 1 mL per minute to 8 mL per minute.
3. A room temperature brine salinity tracer test was then performed by injecting 3 wt% brine at 2 mL/minute. Then the apparatus and fluids were heated overnight to 40 C. After complete heating, the permeability was checked again with 3 wt% brine at 40 C.
4. For CO₂ flooding, the initial brine is replaced by injecting two pore volumes of CO₂-saturated 3 wt% brine. This brine replacement step was not performed for N₂ nor oil flooding.
5. The water-saturated CO₂ and CO₂-saturated brine, or N₂ and brine, or oil and brine were then co-injected into the core at a specified fractional flow. The mass of the effluent fluid was recorded with a mass balance linked to the computer. Once steady-state was reached (indicated by constant pressure drop during at least one pore volume of injected fluids), the respective flow rates and pressure drop were used to calculate the relative permeability of each fluid.
6. A brine tracer was performed with either CO₂-saturated 6 wt% brine or 6 wt% brine while continuing to inject gas at the same rate. Initial brine and tracer brine are injected at same flow rate. This was used to determine the water saturation of

the core at that particular fractional flow. 1200 ppm naphthalene in n-decane was used for an oil tracer. The pore volume of each traced fluid at steady state was determined by integrating the normalized tracer data using the trapezoidal rule. The tracers were injected until the effluent tracer concentration was constant. Under those conditions, the tracer area can be used to calculate the pore volume of the fluid used to inject the tracer.

7. Once the tracer is completed, the tracer fluid in the core was replaced with the initial fluid while continuing to flow the other phase at prescribed rates. The core is now ready for the co-injection of fluids at the next fractional flow.
8. To measure the primary drainage relative permeabilities, decreasing fractional flows of brine were chosen. The brine flow rate was lowered step-wise, with tracers performed at each fractional flow steady-state co-injection, until eventually only gas or oil is injected. When the pressure drop across the core stabilized, the core was considered to be at residual water saturation. For gas flooding, the residual water saturation is determined by subtracting the amount of the produced brine from the water saturation of the previous fractional flow tracer test. For oil flooding, an oil tracer was performed.
9. For the imbibition floods, CO₂-saturated 3 wt% brine or 3 wt% brine was injected with the gas at the prescribed fractional flow. When the first imbibition flood after residual water has stabilized, the instantaneous volume of the expelled brine is subtracted from the instantaneous injected brine volume and, with the subsequent tracer test, the residual water saturation was compared to the previous calculation. Imbibition flooding progressed eventually to injecting only the respective 3 wt% brine with no gas injection. The core was considered to be at residual gas saturation when the pressure drop across the cores stabilized for at least a pore

volume of injected fluids. Imbibition flooding was not performed for oil experiments.

10. Upon completion of the floods, the core was de-pressurized by slowly lowering the gas pressure on the BPR, allowing the fluids to gradually escape. Once de-pressurized the room pressure, a vacuum was applied to the core to remove any gas. The core was then filled with 3 wt% brine, pressurized to approximately 1800 psi, and then flooded with at least two pore volumes of 3 wt% brine to dissolve and displace any remaining gas. The core was then considered to be saturated with brine and ready for the next series of floods.

Chapter 4 – Results and Analysis

The data and analysis of two-phase steady-state relative permeability measurements are presented in this chapter. The same core was used for all the measurements allowing for a direct comparison of the relative permeabilities for the different fluid pairs. The objective of this work was to investigate the effect of composition and pressure on relative permeability. The steady state relative permeability was measured for the following fluid pairs: CO₂/brine, N₂/brine, and n-decane/brine. Measurements for CO₂/brine were also performed at two different pressures while maintaining the same temperature. The properties of the different fluids used are shown in Table 4-1 below. The density of CO₂ at 40 C increases from 0.314 g/mL to 0.745 g/mL when the pressure is increased from 1200 psi to 1900 psi.

Table 4-1: Pure fluid properties at temperature and pressure of corefloods.

Pure Fluid	Temperature	Pressure (psi)	Density (g/mL)	Viscosity (cP)	Estimated Interfacial Tension with Brine
CO ₂	40 C	1900	0.745	0.0624	25.5 mN/m
CO ₂	40 C	1200	0.314	0.0240	32.7 mN/m
N ₂	40 C	1800	0.131	0.0210	60.5 mN/m
n-decane	70 C	1500	0.702	0.549	51.3 mN/m

4.1 INITIAL TESTING

The same Berea sandstone core was used for all the measurements presented in this Chapter. The pore volume measured using a salinity tracer was 84 ml. The brine permeability was measured by injecting brine containing 3 wt% NaCl and 0.1 wt% CaCl₂. The brine permeability data for each section of the core as well as the whole core are shown in Table 4-2.

Table 4-2: Brine permeability data for Berea sandstone core.

Section	Permeability (mD)
1	103
2	100
3	93
4	96
Overall Core	100

During the course of the eight-month experiment, the brine permeability decreased slowly as shown in Table 4-3. Figure 4-1 shows an example of two tracer tests performed two months apart. The aqueous pore volumes measured for the two cases agree within experimental error. No faulty connections or equipment were found. A similar effect was reported by Oak during a year-long relative permeability experiment. For the purpose of calculating the relative permeabilities from the measured pressure drop data, the brine permeability obtained at the beginning of each set of floods was used as the normalization factor.

Table 4-3: Brine permeability data at different times.

Dates of Floods	Flooding Parameters	Brine Permeability (mD)
November 2015 – January 2016	CO ₂ and 3 wt% brine, 40 C and 1900 psi	100.1
February 2016 – March 2016	CO ₂ and 3 wt% brine, 40 C and 1200 psi	74.3
April 2016 – May 2016	N ₂ and 3 wt% brine, 40 C and 1800 psi	64.9
June 2016	oil and 3 wt% brine, 70 C and 1500 psi	57.6

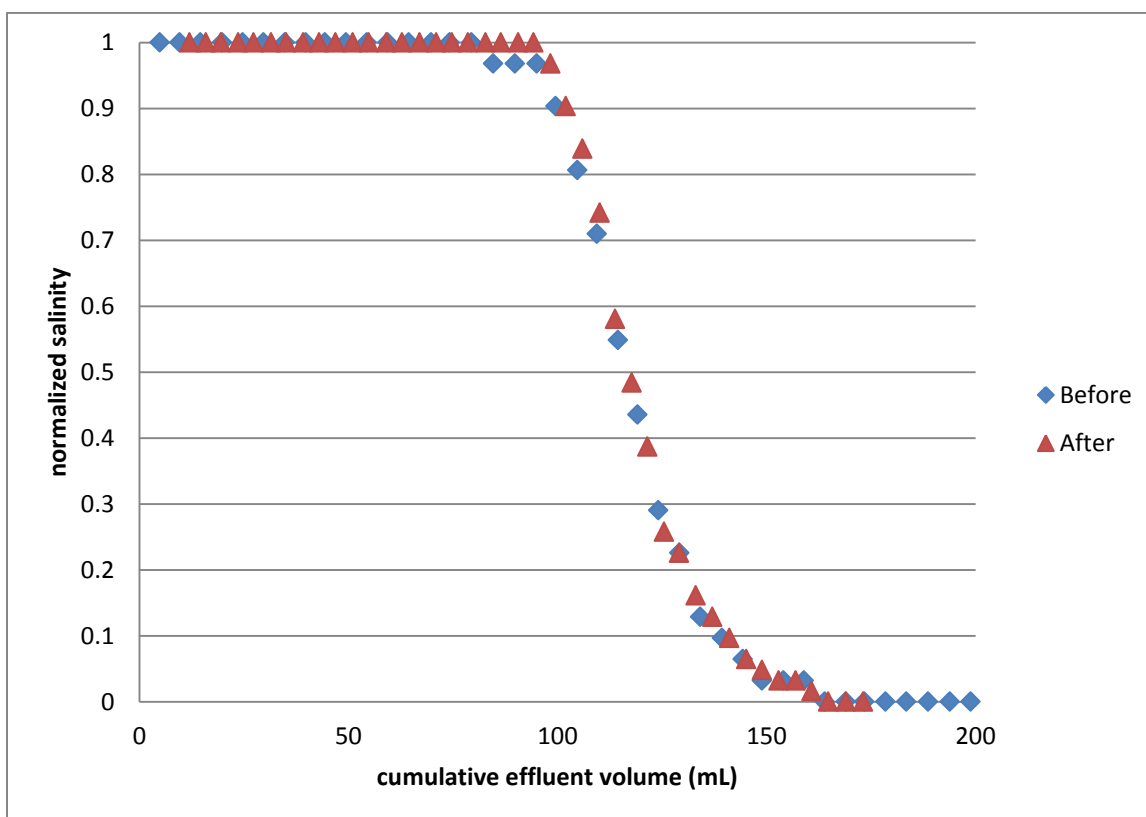


Figure 4-1: Comparison of brine tracers before and after the permeability reduction.

4.2 CARBON DIOXIDE AND BRINE RELATIVE PERMEABILITY EXPERIMENTS

4.2.1 High Density CO₂

Steady-state primary drainage and imbibition relative permeability measurements at several fractional flows of water were performed for high density CO₂ gas and brine. Table 4-4 lists the floods in chronological order, the corresponding flow rates for each fluid, the pressure at the outlet end of the core, and the Rapoport-Leas and capillary numbers. The outlet pressure in these experiments varied as shown in Table 4-4, with an average value of 1876 psi. For simplicity, these experiments will be referred as the 1900 psi experiments. Both brine-saturated CO₂ and CO₂-saturated brine were injected via piston accumulators. The flow rates shown in Table 4-4 correspond to the volumetric rate set at the pumps. The viscosity of pure CO₂ at those conditions varies less than 2%, from 0.0614 cP to 0.0624 cP. A value of 0.068 cP was used as the viscosity of brine-saturated CO₂ gas.

Table 4-4: Flooding parameters for CO₂/brine relative permeability measurements at 1900 psi and 40C.

Brine fractional flow	Brine flow rate (mL/min)	CO ₂ flow rate (mL/min)	Outlet Pressure (psi)	N_{RL}	N_C
1	4	0	1881	-	-
0.5	3	3	1894	8.29	1.31x10 ⁻⁶
0.114	1.8	14	1900	10.16	2.26x10 ⁻⁶
0.125*	2	14	1858	16.93	2.67x10 ⁻⁶
0	0	34	1875	3.93	1.93x10 ⁻⁶
0.25	0.5	1.5	1876	11.61	1.85x10 ⁻⁶
0.5	0.75	0.75	1859	12.44	2.00x10 ⁻⁶
1	1.5	0	1868	-	6.31x10 ⁻⁶

*Core was restored to $S_w = 1$ before this flood

Some of the pressure ports became plugged during injection of brine with a fractional flow of 0.114. The core was depressurized, evacuated to remove the remaining CO₂, and re-pressurized with 6% brine. A salinity tracer with 3% brine was run before proceeding with the rest of the relative permeability measurements.

As detailed in the Methods section, the aqueous pore volume after reaching steady state at each fractional flow was measured using a salinity tracer. The average water saturation in the core was calculated from the aqueous pore volume. Since no sectional water saturations were measured, only the relative permeability values calculated from the pressure drop across the whole core are plotted as a function of saturation.

4.2.1.1 Drainage Relative Permeability Measurement

The primary drainage relative permeabilities for the high density CO₂ and brine at the flow rates given in Table 4-5 are shown in Figure 4-2. The corresponding pressure drop data as a function of time (expressed in pore volumes of injected fluid) are shown in the appendix. The curves shown in Figure 4-2 were determined by fitting the data to the Corey models (see equations 13 through 16 in section 2.4).

Table 4-5: CO₂ and brine flooding parameters for drainage measurements.

Brine fractional flow	Brine rate (mL/minute)	CO ₂ rate (mL/minute)	Outlet Pressure (psi)	N_{RL}	N_C
1	4	0	1881	-	-
0.5	3	3	1894	8.29	1.31x10 ⁻⁶
0.114	1.8	14	1900	10.16	2.26x10 ⁻⁶
0.125	2	14	1858	16.93	2.67x10 ⁻⁶
0	0	34	1875	3.93	1.93x10 ⁻⁶

The Corey model parameters for the high density CO₂ and brine relative permeability curves are shown below:

Table 4-6: High density CO₂ and brine Corey parameters.

Fluid	Drainage Corey Exponent	Imbibition Corey Exponent	Residual Saturation	Endpoint Relative Permeability
brine	1.925	2.528	0.435	0.103
CO ₂	3.902	2.528	0.315	0.691

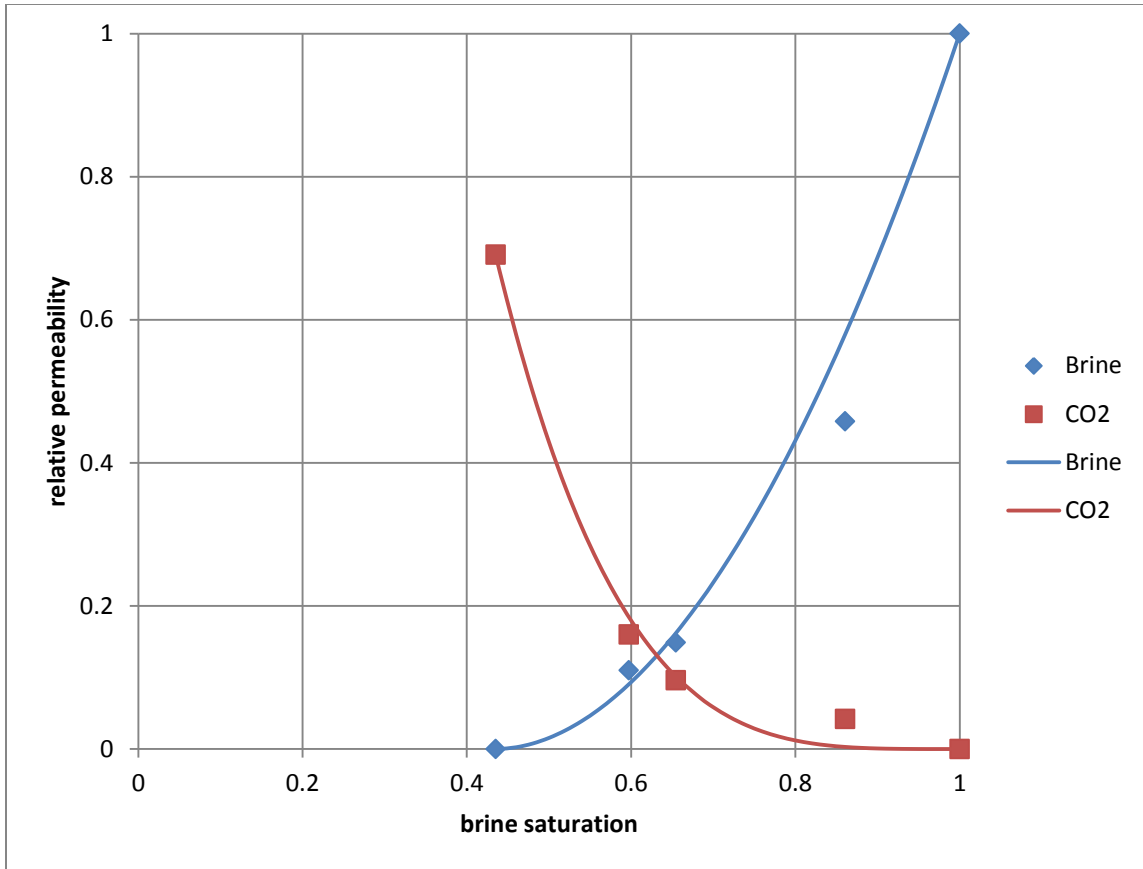


Figure 4-2: CO₂ and brine drainage relative permeabilities at 1900 psi.

Although no sectional saturations were measured, the sectional permeabilities were calculated from the pressure drops across each section. Figures 4-3 and 4-4 show the primary drainage permeabilities to brine and CO₂ for each section of the core. The relative permeability values are uniform across the core except for a brine fractional flow of zero (the gas endpoint). This suggests that the water saturation across the core is uniform for these measurements except for the end point. However, for the case of zero brine flow, the CO₂ relative permeability is higher for the inlet section than the outlet section of the core. Although this behavior could correspond to the presence of end effects, the injection rates were selected to diminish end effects (see Theory chapter).

Instead, it is likely that the 34 pore volumes of CO₂ injected during the flood were not enough to reach residual water saturation throughout the whole core. A fractional flow calculation using the Corey model parameters obtained for the high density CO₂/brine experiment indicates that more than 100 pore volumes of CO₂ gas would be needed to reach the true residual brine saturation.

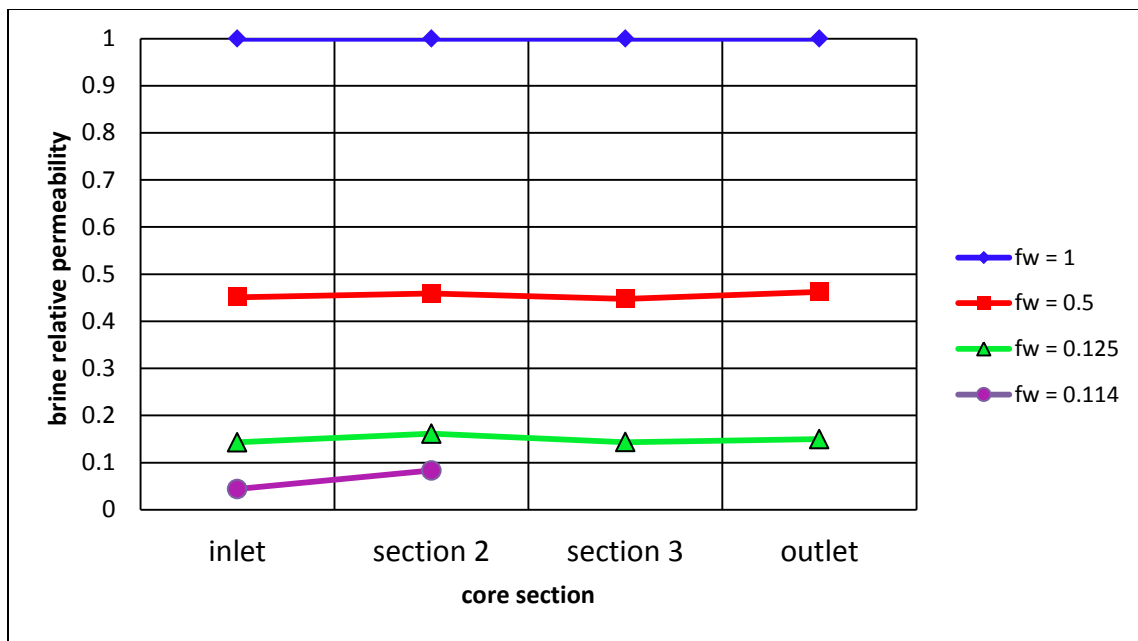


Figure 4-3: Brine drainage relative permeabilities at 1900 psi for each section of the core.

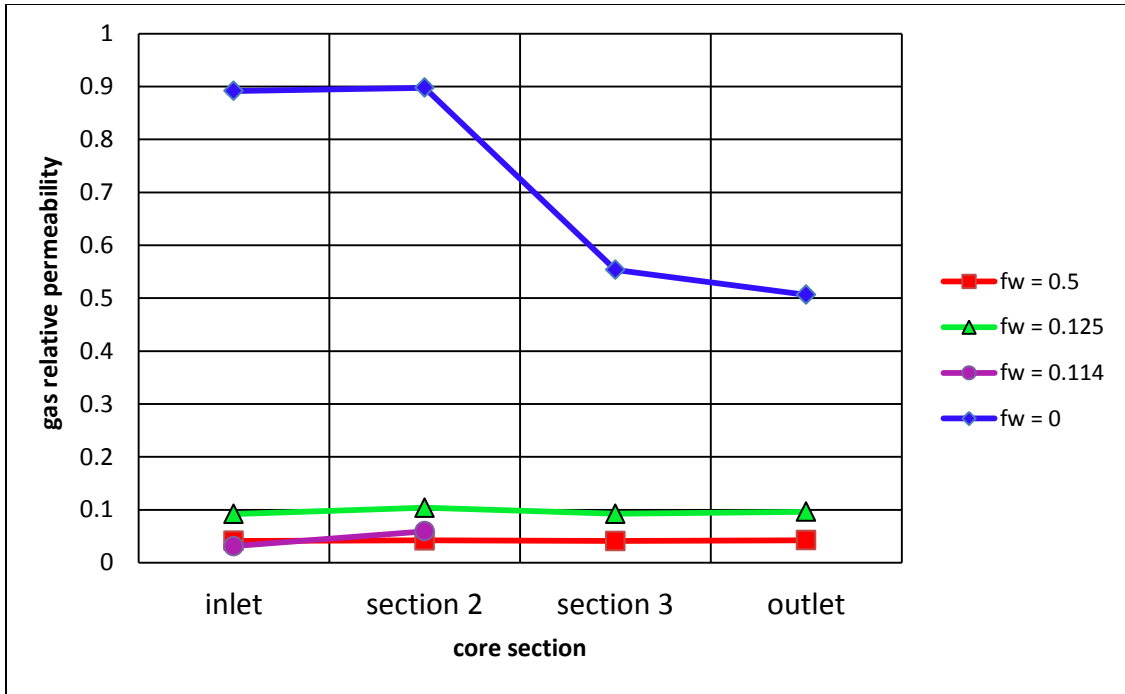


Figure 4-4: CO₂ drainage relative permeabilities at 1900 psi for each section of the core.

4.2.1.2 Imbibition Relative Permeability Measurement

The primary imbibition relative permeabilities for the CO₂ and brine floods were calculated for different fractional flows of brine listed in Table 4-7 and shown in Figure 4-5. The corresponding pressure drops versus injected pore volumes are shown in the Appendix.

Table 4-7: 1900 psi CO₂ and brine imbibition flooding parameters.

Brine fractional flow	Brine rate (mL/minute)	CO ₂ rate (mL/minute)	Outlet Pressure (psi)	N_{RL}	N_C
0	0	34	1875	3.93	1.93×10^{-6}
0.25	0.5	1.5	1876	11.61	1.85×10^{-6}
0.5	0.75	0.75	1859	12.44	2.00×10^{-6}
1	1.5	0	1868	-	6.31×10^{-6}

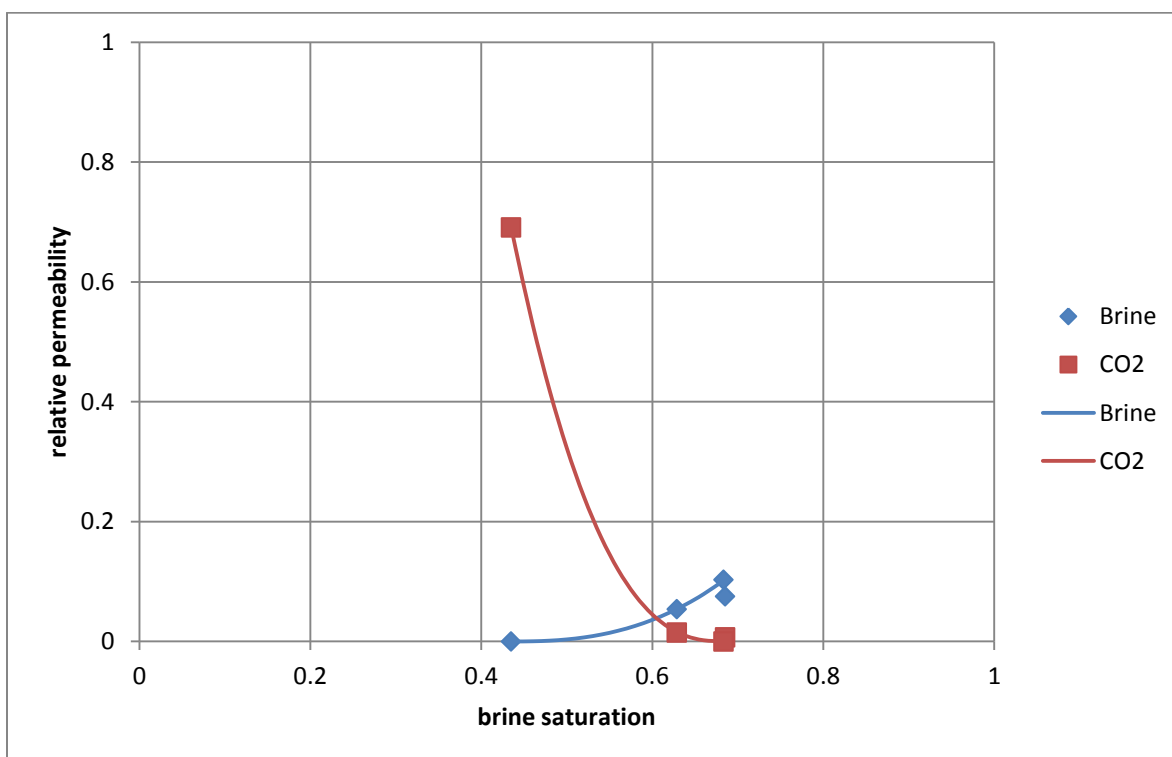


Figure 4-5: CO₂ and brine imbibition relative permeabilities at 1900 psi.

Figures 4-6 and 4-7 show the brine and CO₂ sectional relative permeabilities for each fractional flow of water used during imbibition. In this case, the sectional permeabilities are less uniform across the core; nevertheless, the largest relative standard error of the mean was 16%.

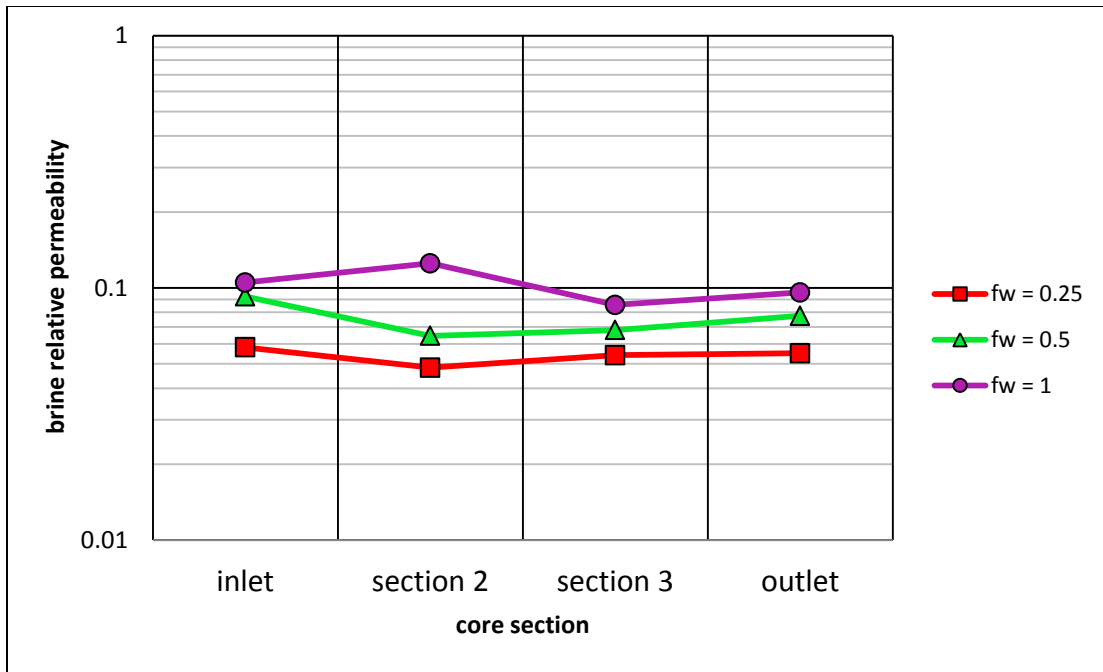


Figure 4-6: Brine imbibition relative permeabilities at 1900 psi for each section of the core.

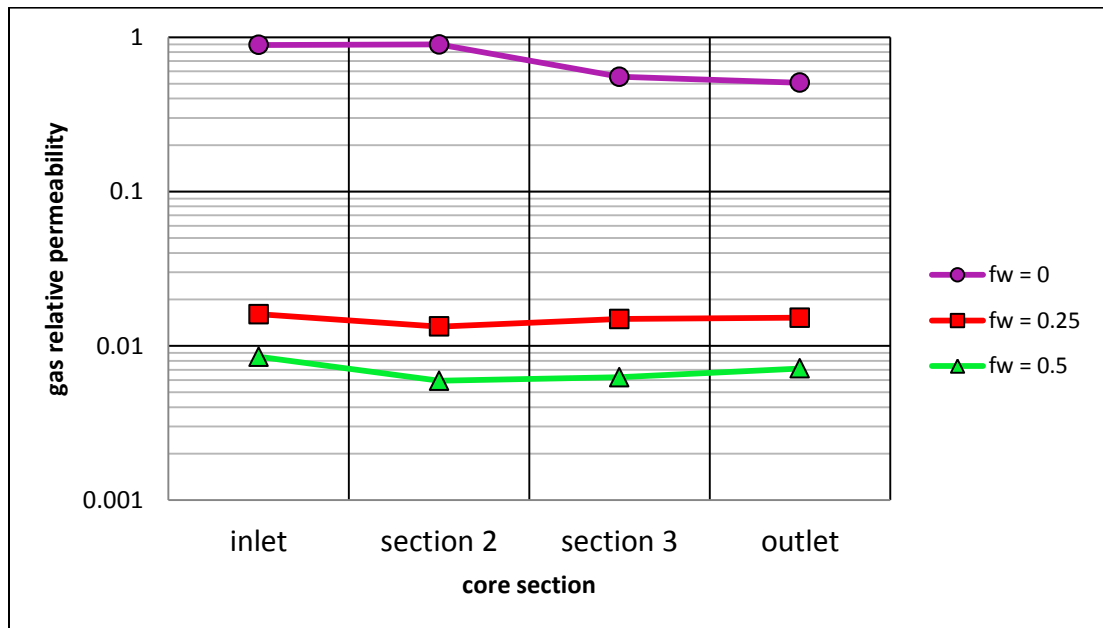


Figure 4-7: CO₂ imbibition sectional relative permeabilities at 1900 psi.

4.2.2 Low Density CO₂

A second set of steady-state relative permeability measurements was performed with CO₂ at the same temperature of 40 C, but at a lower pressure than the experiments of the previous section. Table 4-8 lists the fractional flows in chronological order, the corresponding flow rates for each fluid, the pressure at the outlet end of the core and the Rapoport-Leas and capillary numbers. These experiments will be referred to as the 1200 psi floods. Here again, both brine-saturated CO₂ and CO₂-saturated brine were injected using piston accumulators.

Table 4-8: CO₂ and brine drainage flooding parameters at low pressure.

Brine fractional flow	Brine rate (mL/minute)	CO ₂ rate (mL/minute)	Outlet Pressure (psi)	N_{RL}	N_C
1	2	0	1170	-	-
0.25	2.5	7.5	1178	10.26	1.87×10^{-6}
0	0	80	1180	3.28	1.48×10^{-6}

As discussed before, when co-injecting a compressible gas using a piston accumulator, the gas needs to be pressurized to the inlet core pressure before it can flow into the core. As opposed to the CO₂ and brine co-injections performed at the higher pressure, this effect was significant for the 1200 psi floods. Only the drainage flood at a brine fractional flow of 0.25 resulted in reliable data. Only the end point for primary imbibition was measured for the same reason.

The Corey model parameters for the low density CO₂ and brine relative permeability curves are shown below:

Table 4-9: Low density CO₂ and brine Corey parameters.

Fluid	Drainage Corey Exponent	Imbibition Corey Exponent	Residual Saturation	Endpoint Relative Permeability
brine	3.051	-	0.501	0.0976
CO ₂	1.888	-	0.270	0.380

4.2.2.1 Drainage Relative Permeability Measurement

Figure 4-8 shows the relative permeabilities to CO₂ and brine as a function of water saturation. The Corey curves were determined using only three data points so they are less reliable than previous curves.

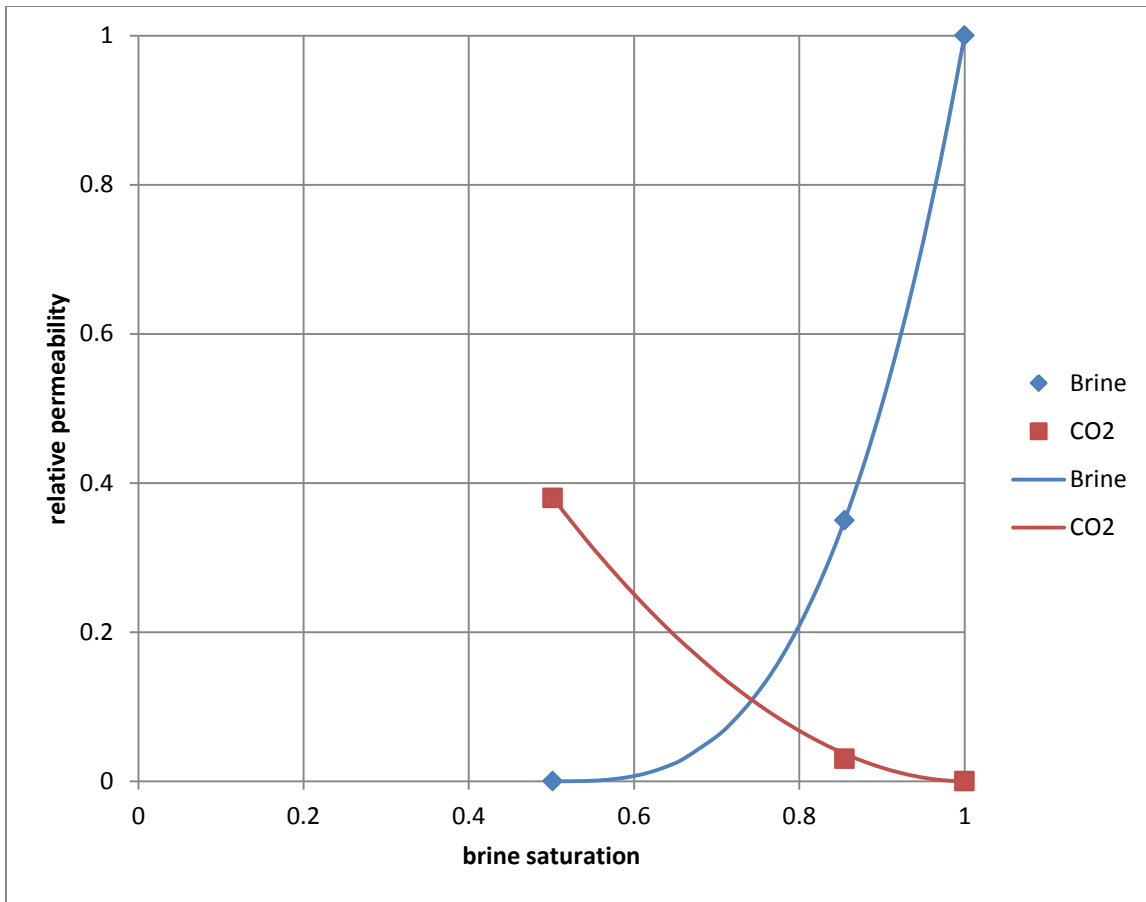


Figure 4-8: CO₂ and brine drainage relative permeabilities at 1200 psi.

Figures 4-9 and 4-10 show the drainage relative permeabilities to brine and CO₂ for each section of the core.



Figure 4-9: Brine drainage sectional relative permeabilities at 1200 psi.

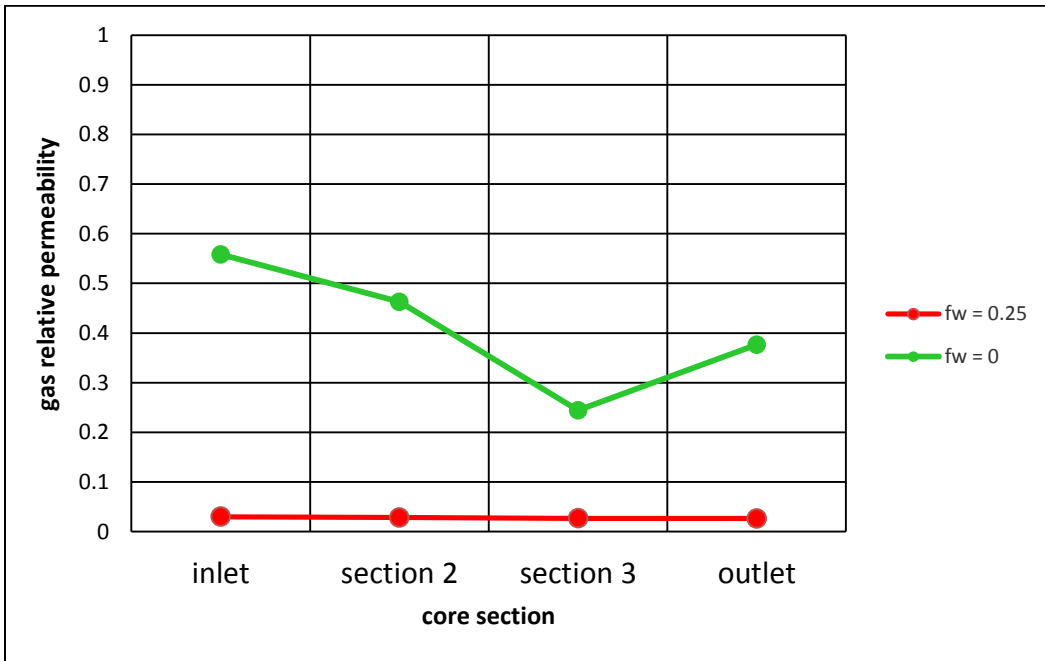


Figure 4-10: CO₂ drainage sectional relative permeabilities at 1200 psi.

In this case, for the measurements performed at a brine fractional flow of 0.25, both the brine and CO₂ sectional relative permeabilities are uniform across the core. However, for the drainage end point flood, a significant variation was observed. Due to the lower viscosity of CO₂ at around 1200 psi than at around 1900 psi, more pore volumes are required to reach steady state at any given fractional flow. This effect is even more pronounced at a brine fractional flow of zero. However, only 57.6 pore volumes of low density CO₂ were able to be injected into the core. Clearly, this amount was not enough to displace all the brine and thus the reported end point is only an apparent value. The true end point permeability is expected to be equal or greater than the value measured in the inlet section of the core, i.e. $k_{rg}^{end} \geq 0.56$. Furthermore, the apparent residual water saturation in this set of experiments is higher than that obtained in the high density CO₂/brine floods, $S_{wr}^{low-\rho} - S_{wr}^{high-\rho} = 0.06$. This difference is larger than the tracer measurement error of ± 0.03 .

4.2.2.2 Imbibition Relative Permeability Measurement

As discussed above, only the end point primary imbibition relative permeability for the CO₂ and brine pair at 1200 psi was calculated and shown in Figure 4-11. A Corey-type curve was not calculated due to the lack of data between the end point relative permeabilities.

Table 4-10: 1200 psi CO₂ and brine imbibition flooding parameters.

Brine fractional flow	Brine rate (mL/minute)	CO ₂ rate (mL/minute)	Outlet Pressure (psi)	N_{RL}	N_C
0	0	80	1180	3.28	1.48×10^{-6}
1	1	0	1176	-	2.32×10^{-6}

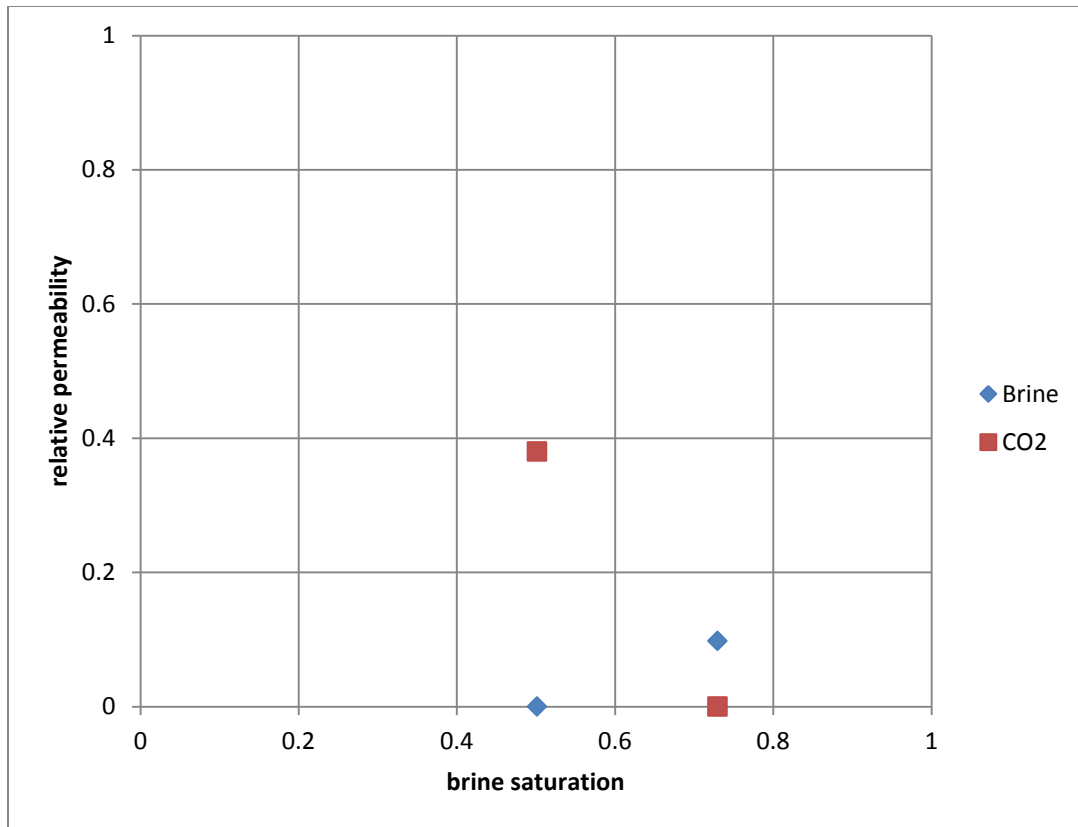


Figure 4-11: CO₂ and brine imbibition relative permeabilities at 1200 psi.

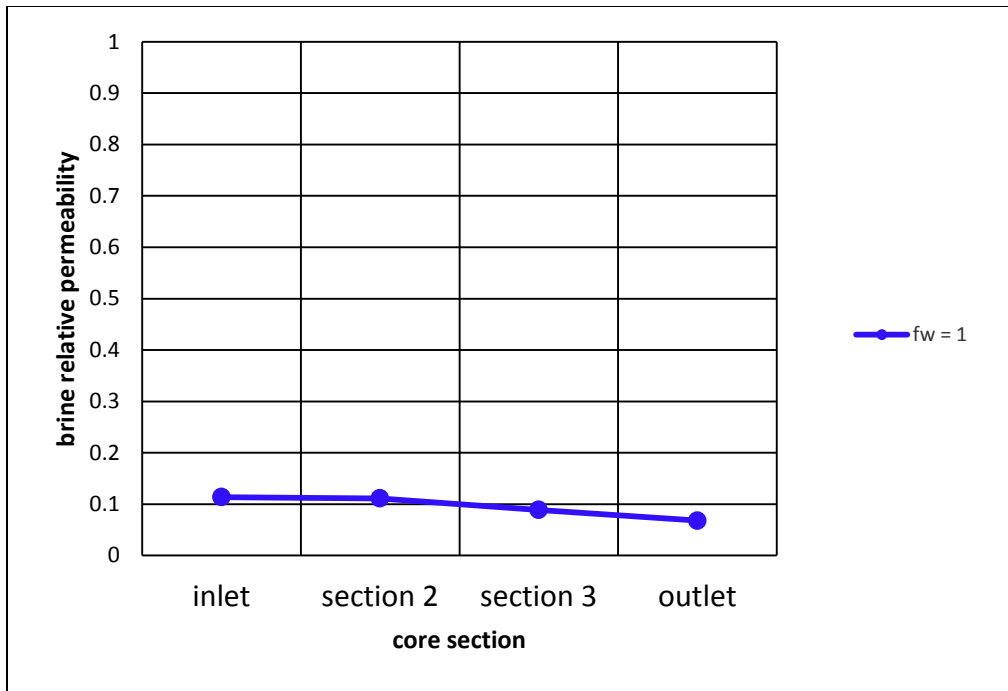


Figure 4-12: Brine imbibition sectional relative permeabilities at 1200 psi.

4.3 NITROGEN AND BRINE RELATIVE PERMEABILITY EXPERIMENTS

4.3.1 Drainage Relative Permeability Measurement

In order to study the effect of composition on relative permeability, steady-state relative permeability measurements were performed with high pressure nitrogen gas and brine using the same core at the same temperature and pressure. Primary drainage and imbibition measurements were performed at several fractional flows of water. Table 4-11 lists the floods in chronological order. In the CO₂ experiments, both CO₂-saturated brine and brine-saturated CO₂ were injected by pumping into piston accumulators. For the N₂/brine experiments, a mass flow controller was used to inject N₂ into the core (see Methods for more details). While the volumetric flow rate at the inlet of the core was set at the pump in the CO₂ experiments, the mass flow rate at the inlet was set in the N₂ floods. The volumetric flow rate corresponding to a given mass flow rate depends on pressure and temperature. The volumetric flow rates listed in Table 4-11 correspond to those at the core outlet.

Table 4-11: Experimental parameters used for the N₂/brine drainage measurements.

Brine fractional flow	Brine rate (mL/minute)	N ₂ rate (mL/minute)	Outlet Pressure (psi)	N_{RL}	N_C
1	3	0	1833	-	-
0.498	3	3.03	1853	5.74	5.33×10^{-7}
0.103	1	8.71	1855	4.76	4.43×10^{-7}
0.0451	2	42.3	1848	19.32	1.66×10^{-6}
0	0	116	1889	4.17	7.86×10^{-7}
1	3	0	1854	-	-
0	0	178	1854	6.41	1.11×10^{-6}

An initial end point flow rate of 116 mL/min was chosen since that resulted in a Rapoport-Leas number larger than three. The brine saturation was determined to be 0.512 at the conclusion of this flood, and using the Leverett J function (Pentland, 2011) for a brine saturation of 0.5, the capillary pressure was estimated to be 1.33 psi. The pressure drop across the core was 31.5 psi, leading to a 23.7 $\Delta P/P_C$ ratio. A second endpoint permeability measurement was repeated at a higher flow rate (178 ml/min), resulting in a higher relative permeability of 0.563 and lower residual brine saturation of 0.443 with a whole core pressure drop of 44.6 psi, leading to a 33.5 $\Delta P/P_C$ ratio.

The Corey model parameters for the N₂ and brine relative permeability curves are shown below:

Table 4-12: N₂ and brine Corey parameters

Fluid	Drainage Corey Exponent	Imbibition Corey Exponent	Residual Saturation	Endpoint Relative Permeability
brine	3.354	1.946	0.443	0.560
N ₂	1.978	2.552	0.369	0.0889

Figure 4-13 shows the drainage relative permeabilities for the N₂ and brine experiments.

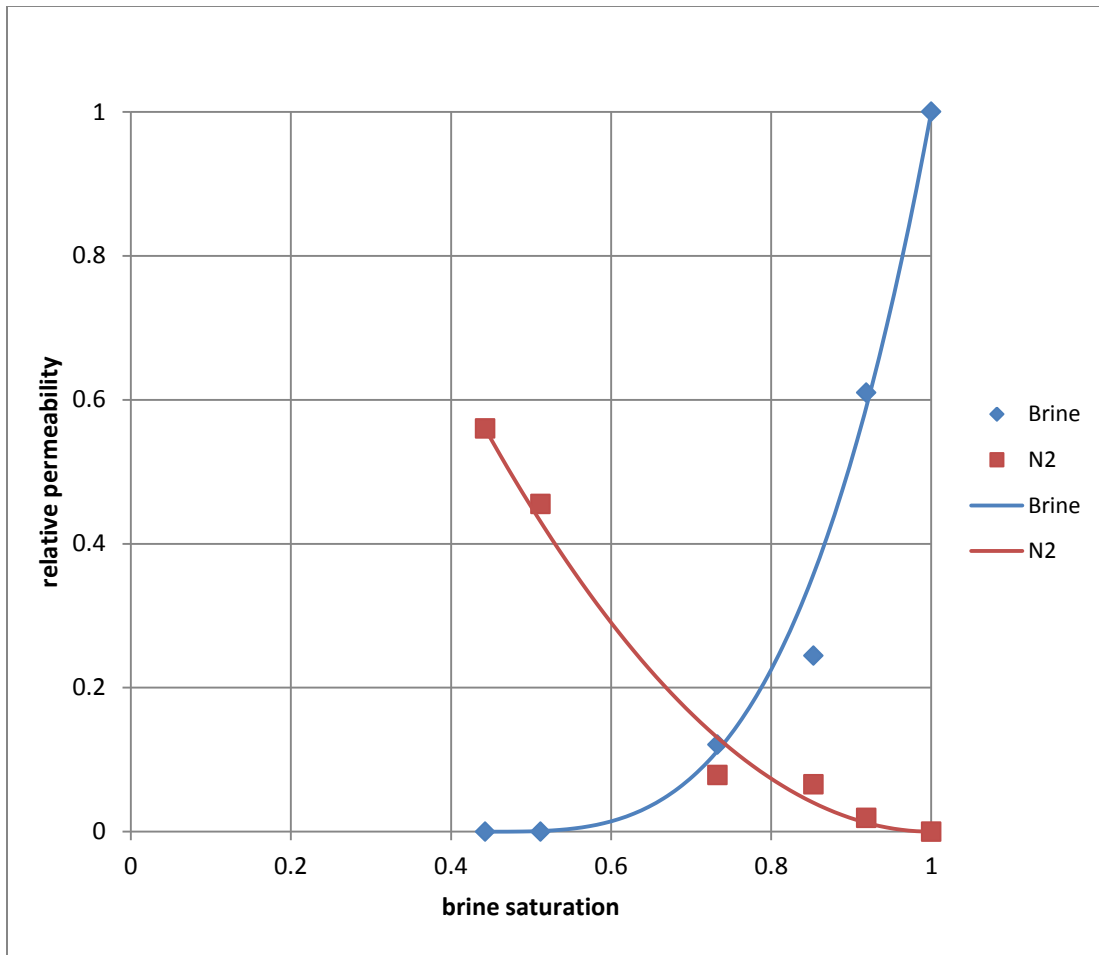


Figure 4-13: N₂ and brine drainage relative permeabilities at 1800 psi.

The drainage sectional permeabilities to brine and N₂ are shown in Figures 4-14 and 4-15, respectively. Except for the brine fractional flow of zero, both the brine and N₂ sectional permeabilities are uniform throughout the core. On the other hand, the N₂ relative permeability is higher for the inlet section than for the outlet during the end point relative permeability measurement. Figure A-17 shows that steady state was not reached

since the pressure drop across the core was still decreasing with injected pore volumes of nitrogen. This again suggests that the lower outlet N_2 relative permeability is due to fractional flow effects, even though approximately 180 pore volumes of nitrogen were injected into the core. Assuming that sections 1 and 2 are at, or close to, residual saturation, the end point relative permeability is about 0.62 ± 0.05 . The water saturation measured was 0.443, which agrees within experimental error to that measured with the dense CO_2 phase.

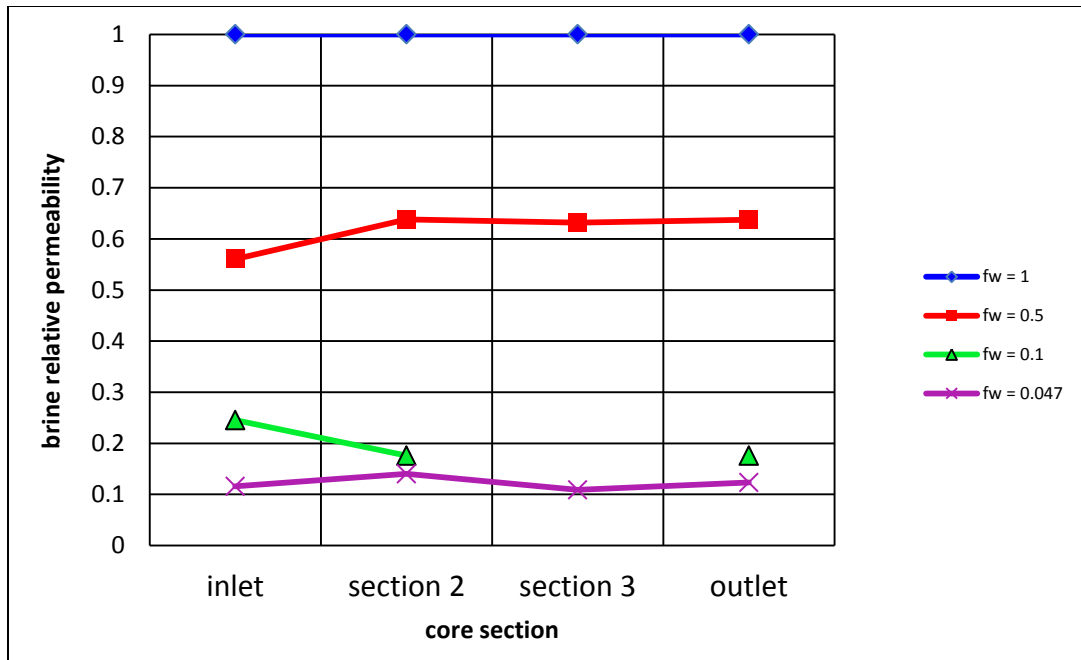


Figure 4-14: Brine drainage sectional relative permeabilities at 1800 psi.

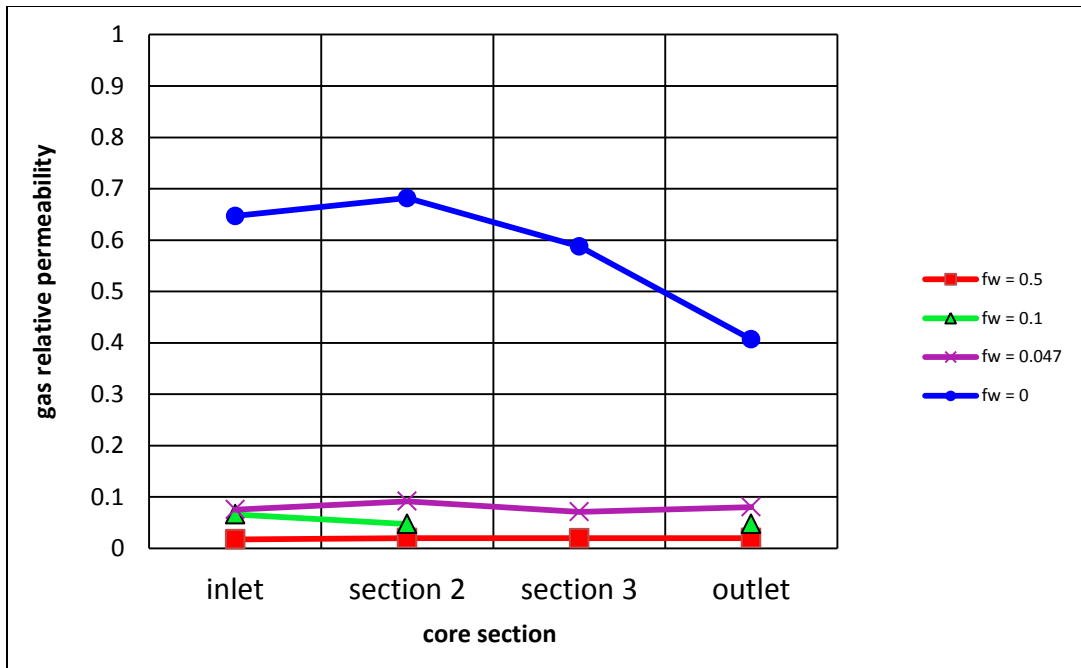


Figure 4-15: N₂ drainage sectional relative permeabilities at 1800 psi.

4.3.2 Imbibition Relative Permeability Measurement

Relative permeability measurements were also performed during imbibition. The fractional flows chosen are listed in Table 4-13.

Table 4-13: N₂ and brine imbibition flooding parameters.

Brine fractional flow	Brine rate (mL/minute)	N ₂ rate (mL/minute)	Outlet Pressure (psi)	N_{RL}	N_C
0	0	178	1854	6.41	1.11×10^{-6}
0.0559	0.75	12.67	1845	20.72	1.94×10^{-6}
0.198	0.75	3.04	1843	14.21	1.37×10^{-6}
1	0.75	0	1842	-	9.37×10^{-7}

Figure 4-16 shows the primary imbibition relative permeabilities to brine and N₂.

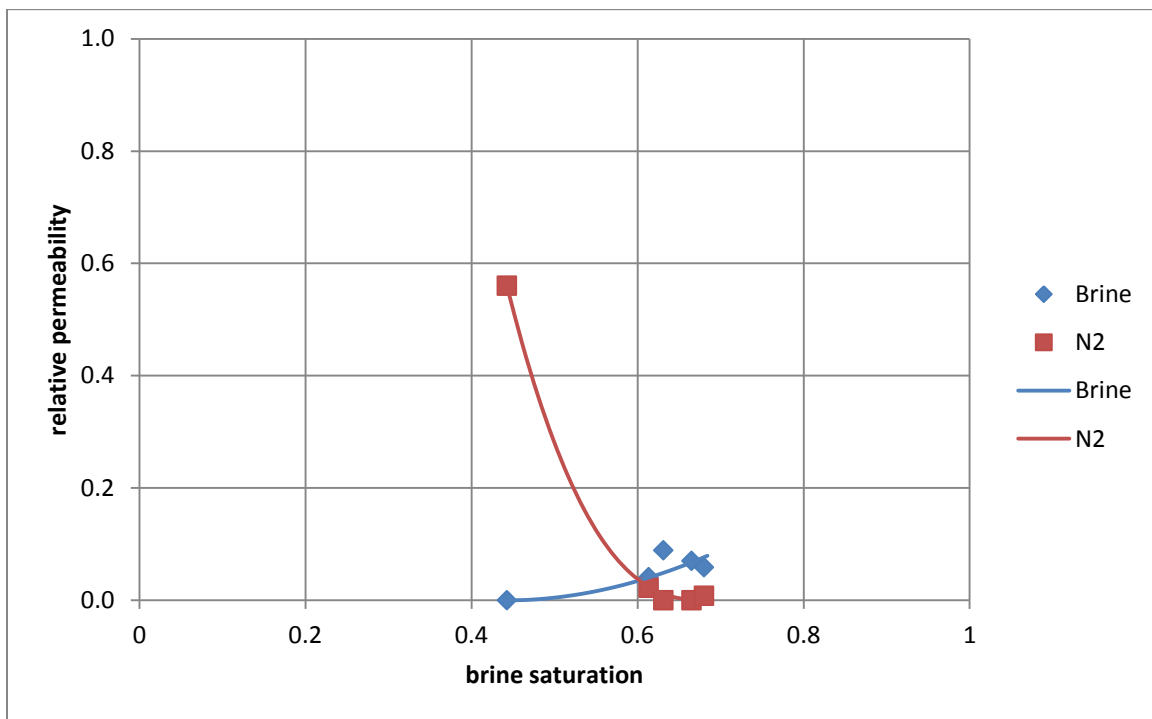


Figure 4-16: N₂ and brine imbibition relative permeabilities at 1800 psi.

Figures 4-17 and 4-18 show the primary imbibition relative permeabilities of each section of the core. As shown in Figure A-20, the pressure drop in section 1 continued to decrease after the pressure drops across the other sections reached steady state. This effect was observed in the two imbibition end point experiments. It did not appear to be caused by pressure port plugging. The cause might be an entry capillary pressure effect.

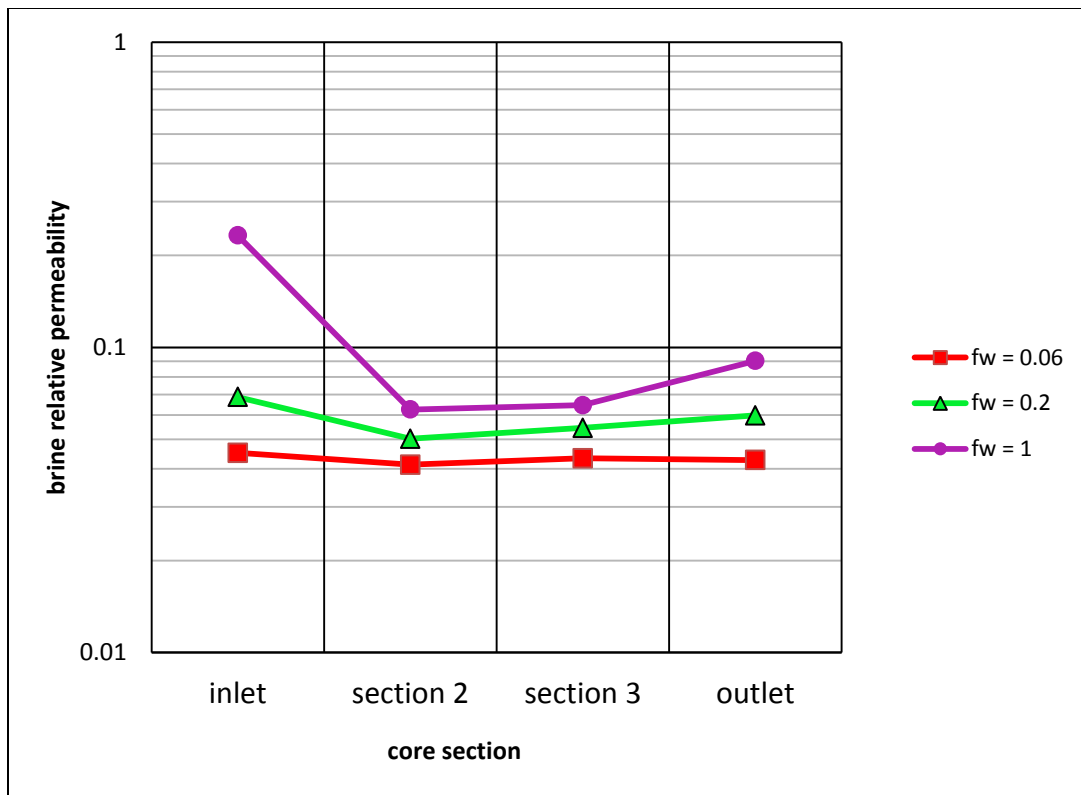


Figure 4-17: Brine imbibition sectional relative permeabilities at 1800 psi.

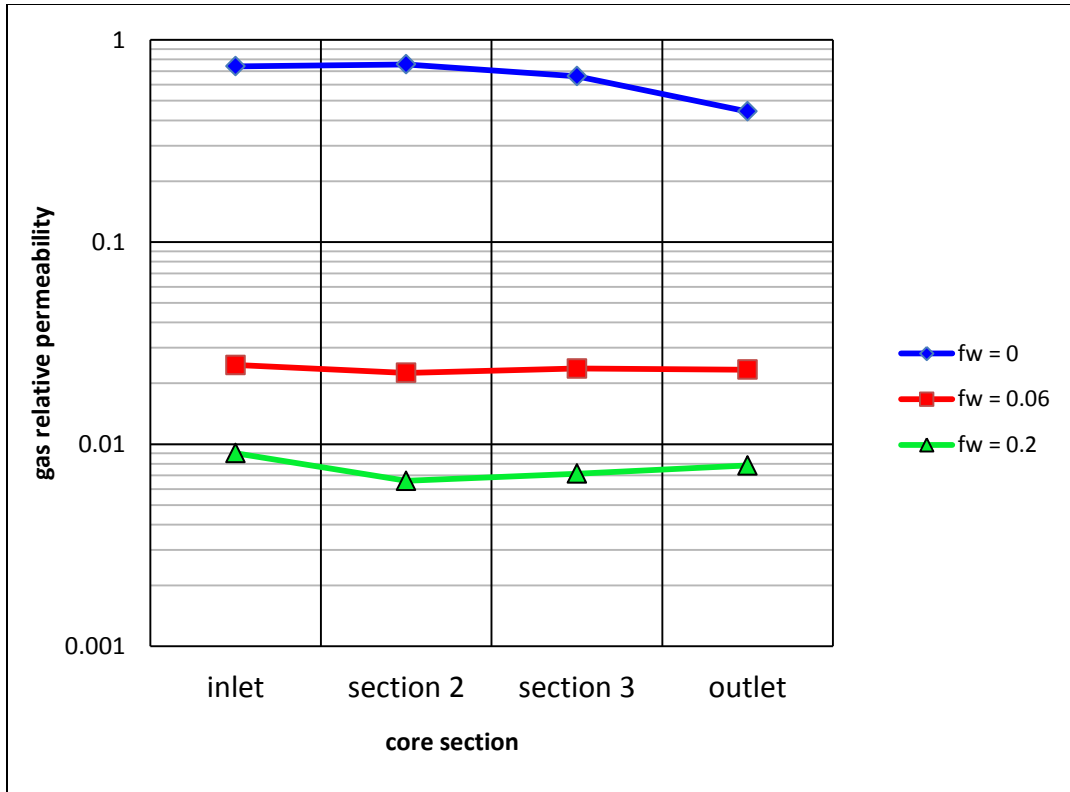


Figure 4-18: N₂ imbibition sectional relative permeabilities at 1800 psi.

4.4 DECANE AND BRINE RELATIVE PERMEABILITY EXPERIMENTS

Steady-state relative permeability measurements were also performed for n-decane and brine at 1500 psi and 70 C. At these conditions, the density of n-decane is similar to that of the dense CO₂ used in the previous experiments. As opposed to CO₂ and N₂, only primary drainage relative permeability measurements were performed for this case. Table 4-14 lists the n-decane and brine floods performed in chronological order:

Table 4-14: Brine and oil flooding parameters.

Brine fractional flow	Brine rate (mL/minute)	Oil rate (mL/minute)	Outlet Pressure (psi)	N_{RL}	N_C
1	2	0	1527	-	-
0.95	1.9	0.1	1536	3.12	3.62×10^{-7}
0.75	1.5	0.5	1553	4.69	5.30×10^{-7}
0.25	0.6	1.8	1549	6.49	7.21×10^{-7}
0	0	7	1547	6.56	8.01×10^{-7}

The Corey model parameters for the n-decane and brine relative permeability curves are shown below:

Table 4-15: n-decane and brine Corey parameters.

Fluid	Drainage Corey Exponent	Imbibition Corey Exponent	Residual Saturation	Endpoint Relative Permeability
brine	3.377	-	0.455	-
n-decane	1.844	-	-	0.860

Both brine and oil tracers were used during each co-injection experiment except oil tracer was used for the brine fractional flow of 0.95 experiment since that would have

required the co-injection of a volume of brine larger than the available accumulators. Figure 4-19 shows the primary drainage relative permeabilities to brine and n-decane. For comparison, the saturations obtained with both tracers at each fractional flow are shown. Corey-type curves were fitted to the data using the brine saturations obtained with both the brine and oil tracers.

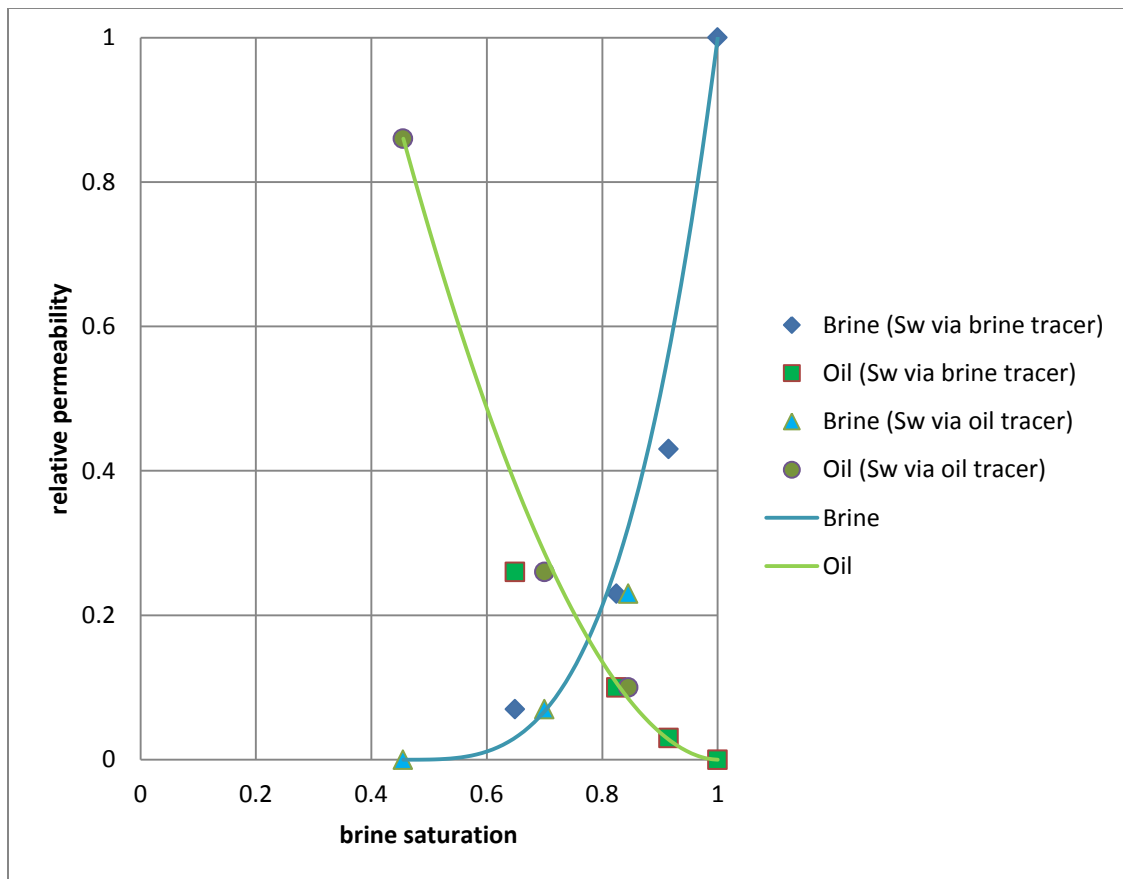


Figure 4-19: Oil and brine drainage relative permeabilities at 1500 psi.

The sectional relative permeabilities to brine and to oil are shown in Figures 4-20 and 4-21.

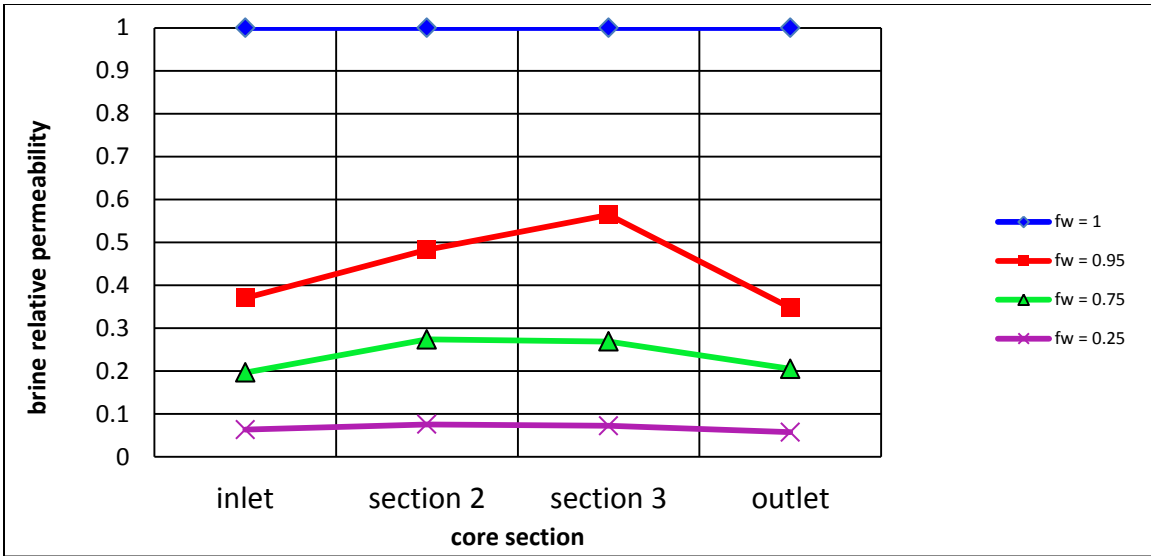


Figure 4-20: Brine drainage sectional relative permeabilities at 1500 psi.

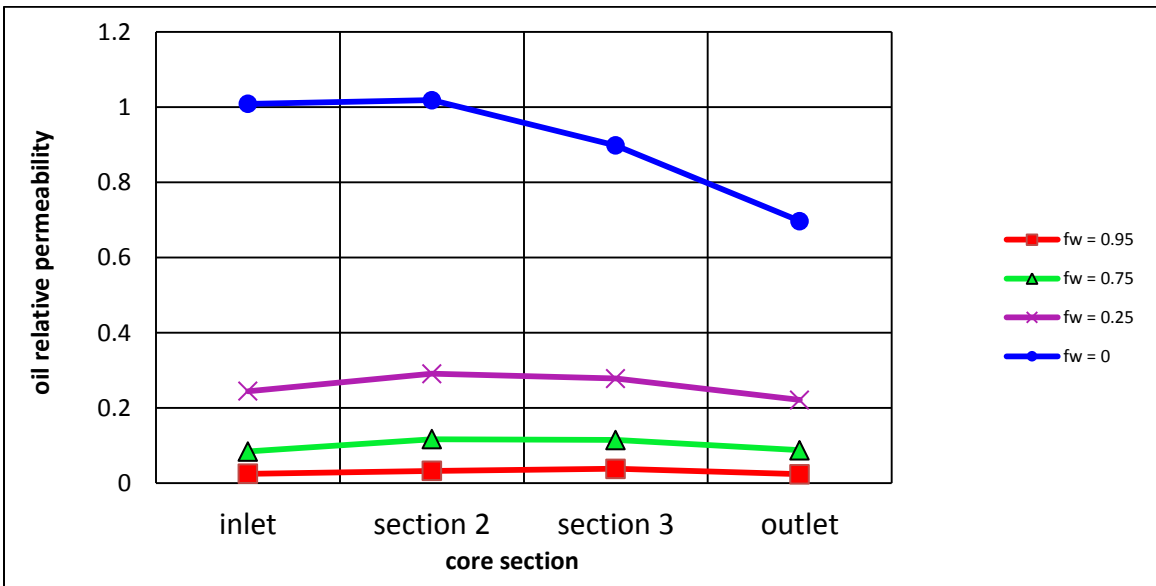


Figure 4-21: Oil drainage sectional relative permeabilities at 1500 psi.

4.5 COMPARISON OF RELATIVE PERMEABILITY DATA

The measured relative permeability for the different fluid pairs and pressures are compared in this section.

4.5.1 Relative Permeabilities

4.5.1.1 High Density CO₂ versus N₂

As shown in Figure 4-22, several significant differences in the relative permeabilities were found between the high density CO₂/brine and N₂/brine cases. First, the water saturation at which the non-wetting phase equals the wetting phase relative permeability is lower for the high density CO₂/brine case than that of the N₂/brine. A similar shift of the wetting and non-wetting relative permeability crossover point is expected with varying rock wettability (Krevor, 2012), suggesting a difference in wettability for the CO₂/brine case. Indeed, Chiquet et al. (2007) showed that the wettability of both mica and quartz transition from a water-wet to a more intermediate-wet condition for CO₂ pressures above 10 MPa.

In addition, N₂ has a lower endpoint relative permeability than the high density CO₂. At 1900 psi and 40 C, CO₂ has a density and an interfacial tension with water similar to that of oil (see Table 4-1). This is the case for the endpoint relative permeability calculated from the pressure drop across the whole core (Figures 4-2 and 4-13) as well as the relative permeabilities measured in the inlet section (Figures 4-4 and 4-15). This observation is consistent with the higher endpoint relative permeability for oil than for nitrogen gas measured by Oak (1990).

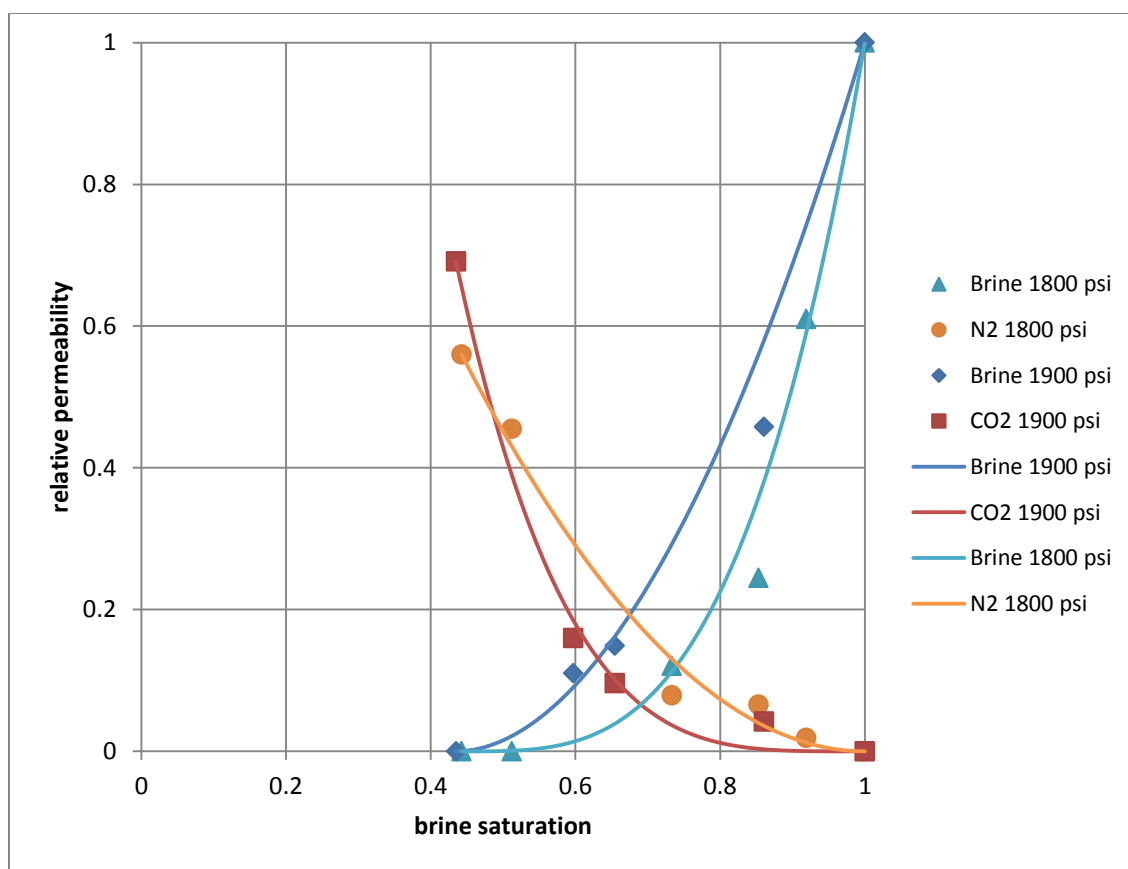


Figure 4-22: Comparison of drainage relative permeabilities of high density CO₂/brine versus N₂/brine.

Figure 4-23 shows the relative permeabilities measured during primary imbibition for the high density CO₂/brine, as well as the N₂/brine, cases. It is difficult to see from Figure 4-23; however, as shown in Table 4-16, the wetting and non-wetting primary imbibition relative permeabilities measured for the high density CO₂/brine were also higher than those for N₂/brine at any given saturation. The only exception was the brine relative permeability in the inlet section during the imbibition endpoint flood (Figure A-20). However, as mentioned above, the pressure drop across the first section continued to decrease with injected volumes of brine while the rest of the sections appeared to be at steady state for the N₂/brine flood.

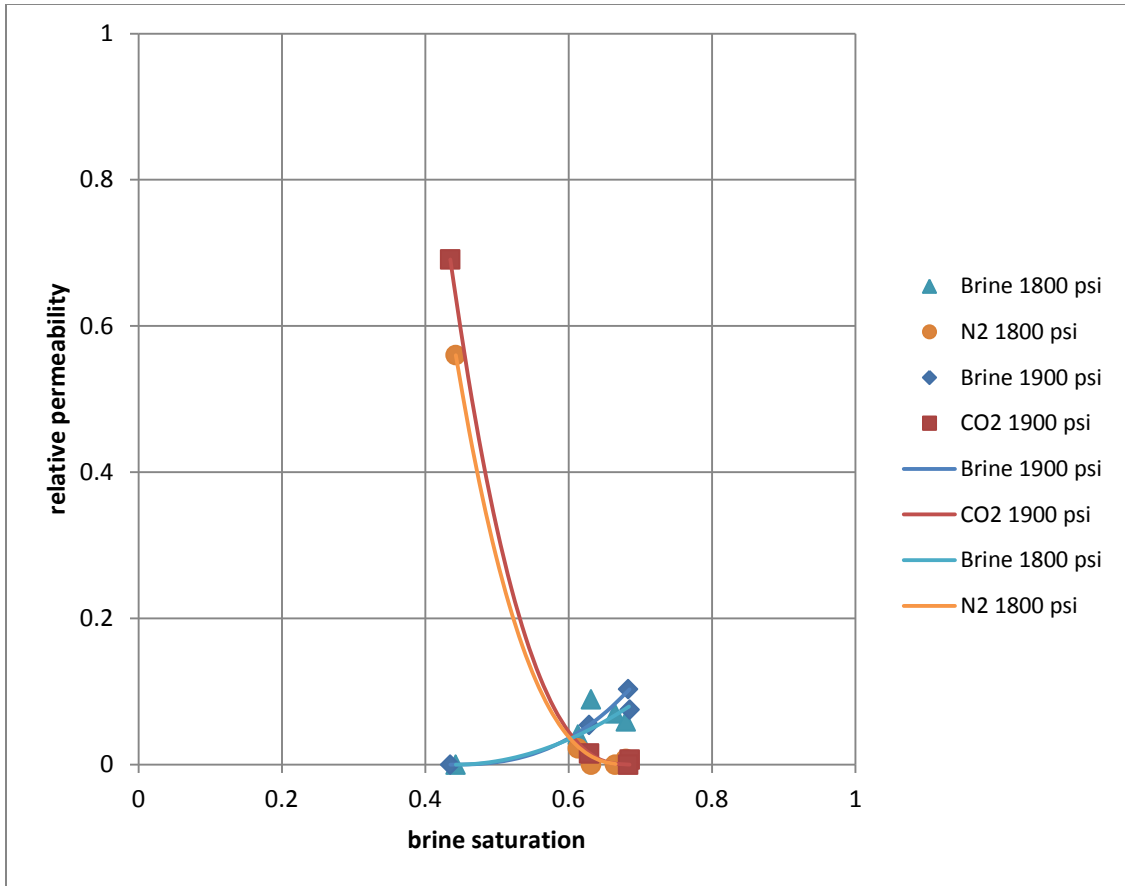


Figure 4-23: Comparison of imbibition relative permeabilities of high density CO₂/brine versus N₂/brine.

Table 4-16: Imbibition relative permeabilities for high density CO₂/brine and N₂/brine.

high density CO ₂ /brine				N ₂ /brine			
f _w	S _w	k _{rw}	k _{rg}	f _w	S _w	k _{rw}	k _{rg}
0	0.43	0.000	0.691	0.000	0.443	0.000	0.560
0.25	0.63	0.054	0.015	0.059	0.613	0.041	0.022
0.5	0.69	0.075	0.007	0.198	0.680	0.059	0.008
1	0.68	0.103	0.000	1.000	0.631	0.089	0.000

4.5.1.2 Low Density CO₂ versus N₂

As opposed to the high density CO₂ case, no significant differences were observed for low density CO₂ compared to N₂. For example, the wetting and non-wetting relative permeability crossover point during primary drainage appears to be similar in this case (Figure 4-24). Interestingly, the experimental pressure for the low density CO₂ floods is below the transition pressure from water-wet to intermediate-wet reported by Chiquet et al. (2007) for CO₂, brine and mica or quartz, suggesting a similar wettability for low density CO₂ and N₂ at this pressure.

On the other hand, although both the drainage endpoint permeability and residual water saturation are different between the two cases, it is likely that the lower endpoint, and higher residual water saturation measured in the low density CO₂ experiments is due to a fractional flow effect since the viscosity for the two gases is almost identical, but only 57.6 pore volumes of CO₂ were injected during the endpoint flood compared to the over 180 pore volumes of N₂ injected.

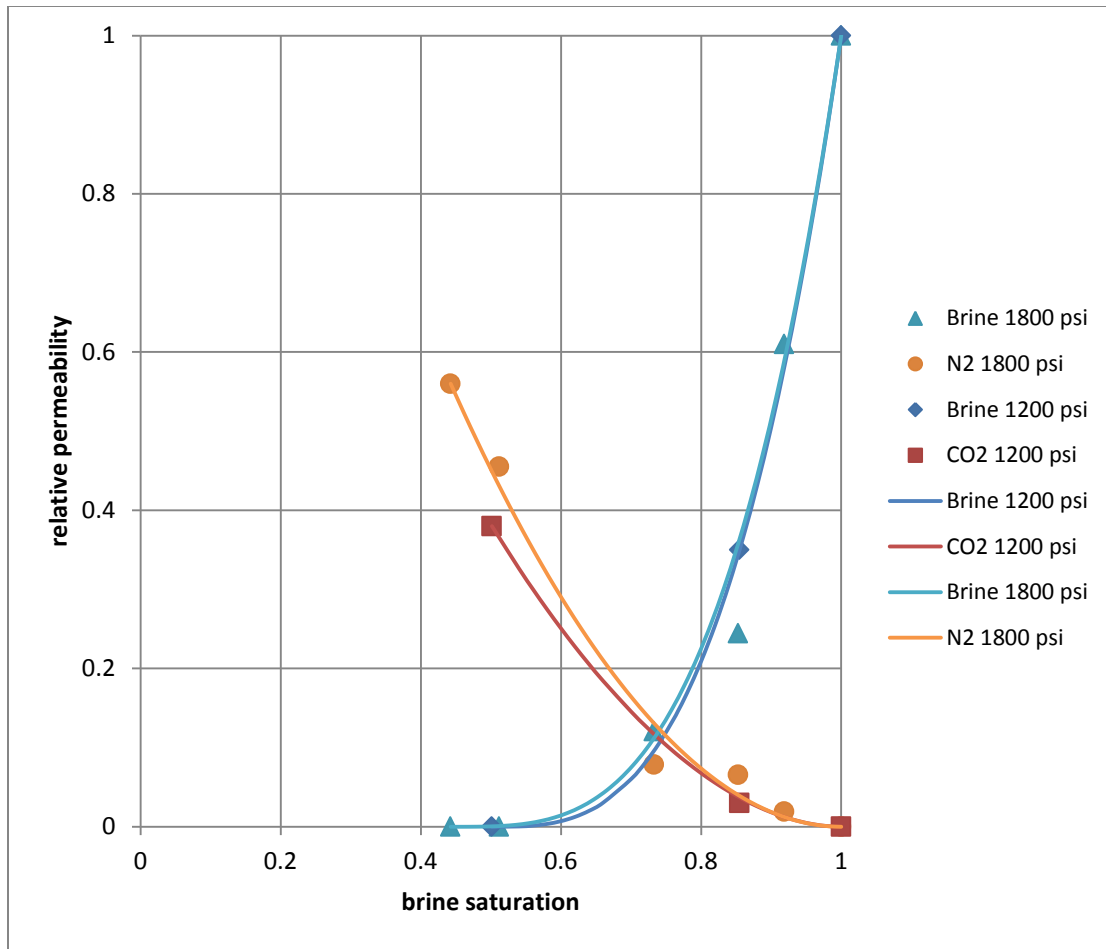


Figure 4-24: Comparison of drainage relative permeabilities of low density CO₂/brine versus N₂/brine.

A lower residual gas saturation and a higher brine endpoint relative permeability were measured during primary imbibition in the low density CO₂/brine experiments than in the N₂/brine experiments. However, due to the higher residual water saturation obtained during drainage, a lower residual gas saturation is expected during imbibition. Therefore, while the difference in residual gas saturation is larger than the experimental error, it is likely not representative of the true residual gas saturation difference, if any, for primary imbibition.

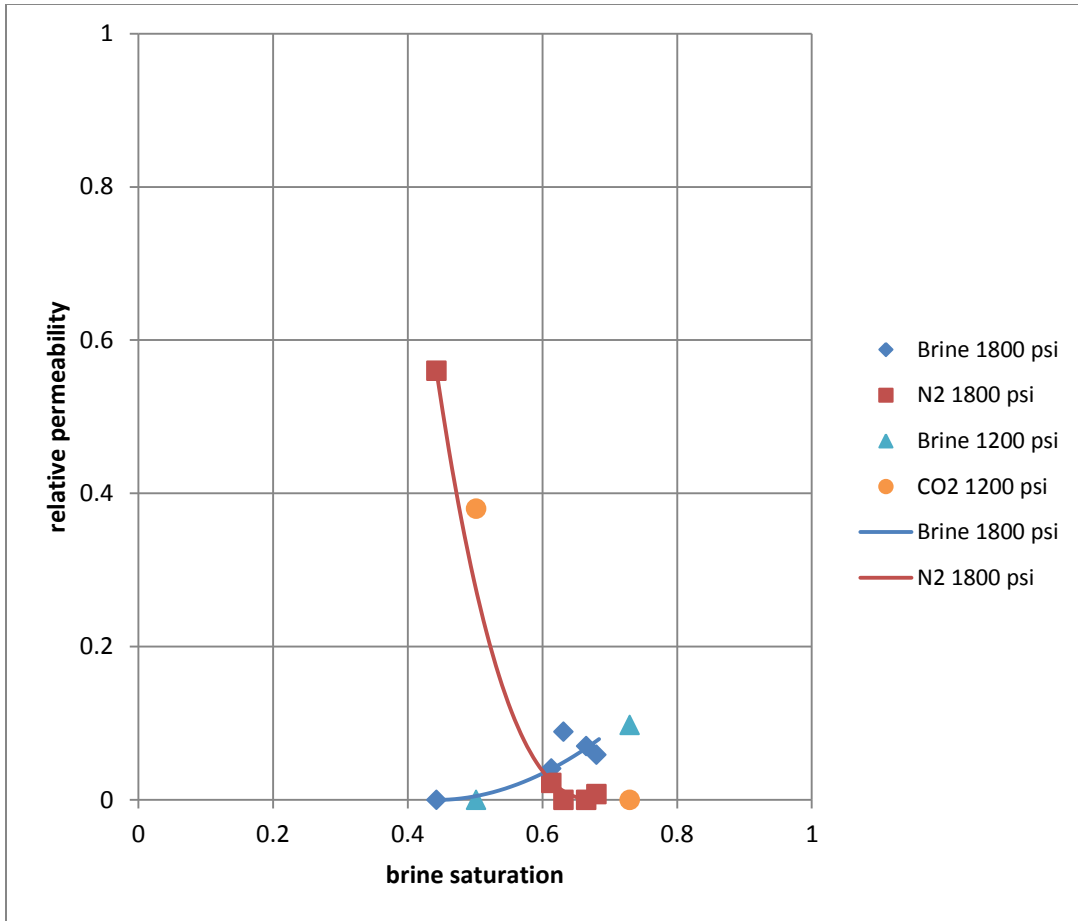


Figure 4-25: Comparison of imbibition relative permeabilities of low density CO₂/brine versus N₂/brine.

4.5.1.3 High Density CO₂ versus Low Density CO₂

Due to the striking similarities between the low density CO₂/brine relative permeabilities and the N₂/brine relative permeabilities, most of the differences discussed in section 4.5.1.1 are applicable here. As discussed in section 4.5.1.2, the residual gas saturation for the low density CO₂/brine experiments was higher than that for the N₂/brine experiments. Similarly, the brine endpoint relative permeability was higher in the low density CO₂/brine experiment than in the N₂/brine. However, the brine endpoint relative permeability obtained for the low density CO₂/brine experiments within 6% of each other.

The drainage data for high density CO₂ and low density CO₂ fit moderately well within each other's Corey-type curves. The high density CO₂ resulted in a lower residual brine saturation than the low density CO₂ as well as a higher endpoint relative permeability. This is expanded upon in section 4.5.3.

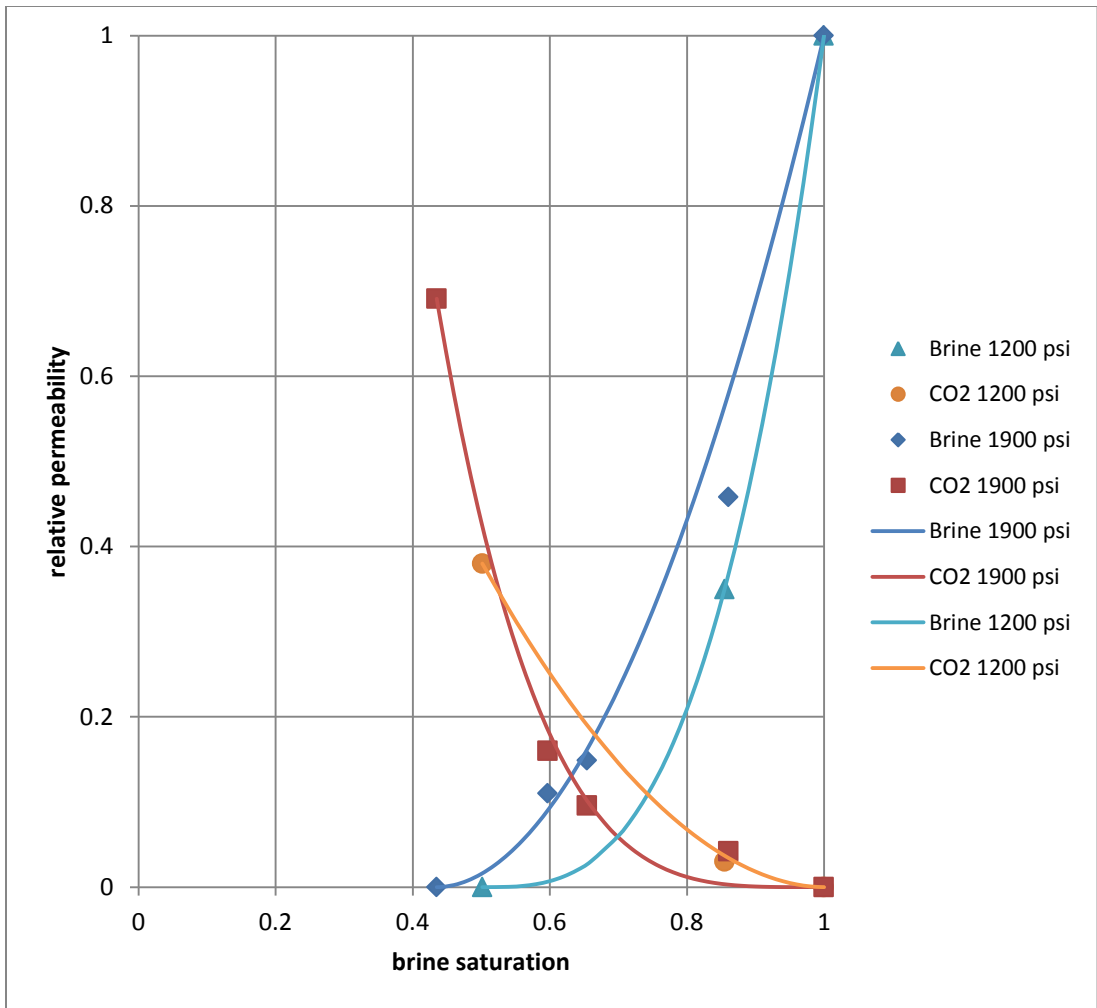


Figure 4-26: Drainage comparisons of high density CO₂ versus low density CO₂ flooding.

The imbibition data that exists for the low density CO₂/brine fits well on to the curve of the high density CO₂/brine imbibition curve, with a slight shift in residual saturations.

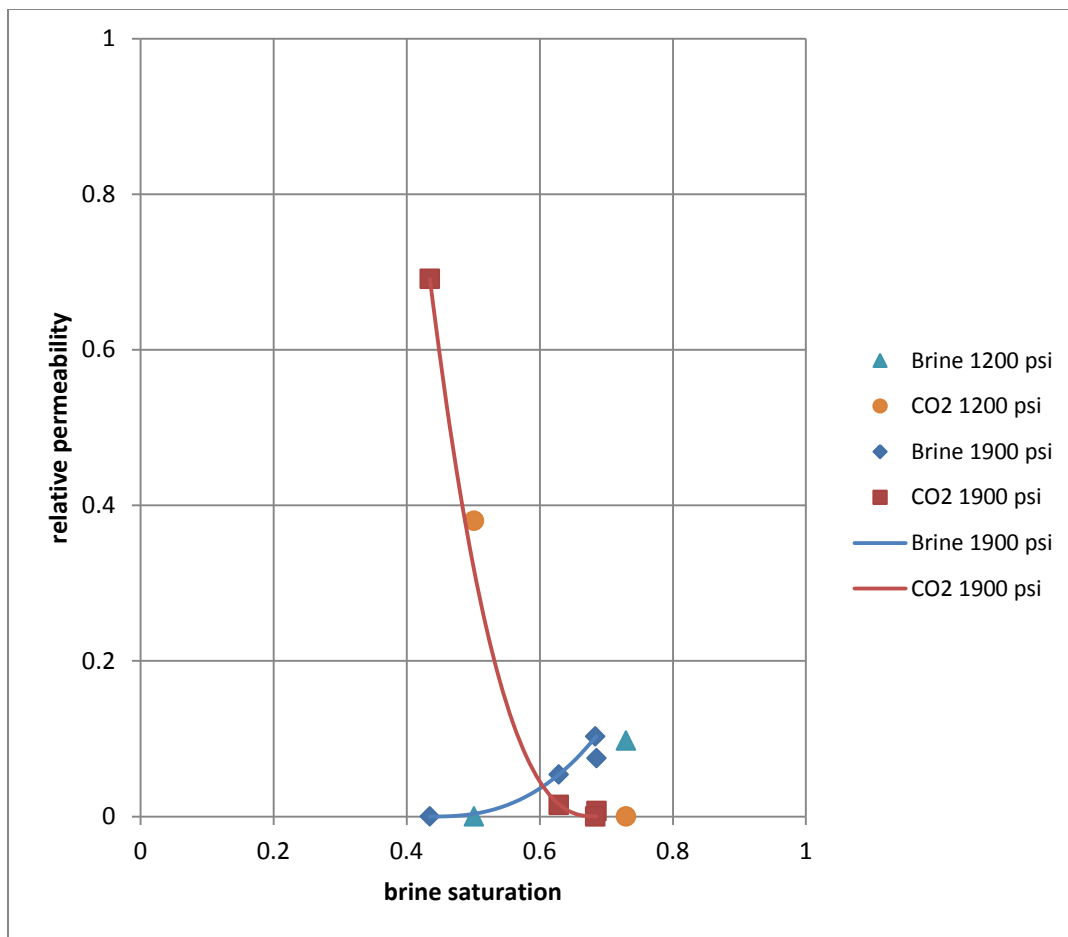


Figure 4-27: Imbibition comparisons of high density CO₂ versus low density CO₂ flooding.

4.5.1.4 N_2 versus *n*-Decane

Only primary drainage relative permeabilities were measured in the decane/brine experiments. While the brine relative permeabilities are essentially identical for the oil/brine and the gas/brine experiments, significant differences were found for the non-wetting phase relative permeabilities as shown in Figure 4-28. As mentioned in section 4.4, the fluid saturations were measured with both a brine tracer and an oil tracer. As seen in Figure 4-28, the water saturations calculated from the oil tracer are slightly higher than those obtained with the brine tracer. The crossover saturation for the oil/brine relative permeabilities is within experimental error of the crossover saturation for the N_2 /brine relative permeabilities suggesting similar wettabilities for both the oil and the gas experiments.

The *n*-decane endpoint relative permeability is significantly higher than that for N_2 . While *n*-decane has a higher viscosity than N_2 , it is also denser. Interestingly, a similar effect was observed for the high density CO_2 when compared to N_2 , even though their viscosities are closer. This suggests that denser non-wetting phases have a higher endpoint relative permeability. However, the oil endpoint is higher than the high density CO_2 , even though the CO_2 has a slightly higher density than *n*-decane at experimental conditions (Table 4-1). Therefore, while density appears to affect relative permeability, it is not necessarily a good correlating parameter by itself.

Due to the similarities between the low density CO_2 /brine and the N_2 /brine results, all of the analysis presented in this section also applies to the low density CO_2 /brine case.

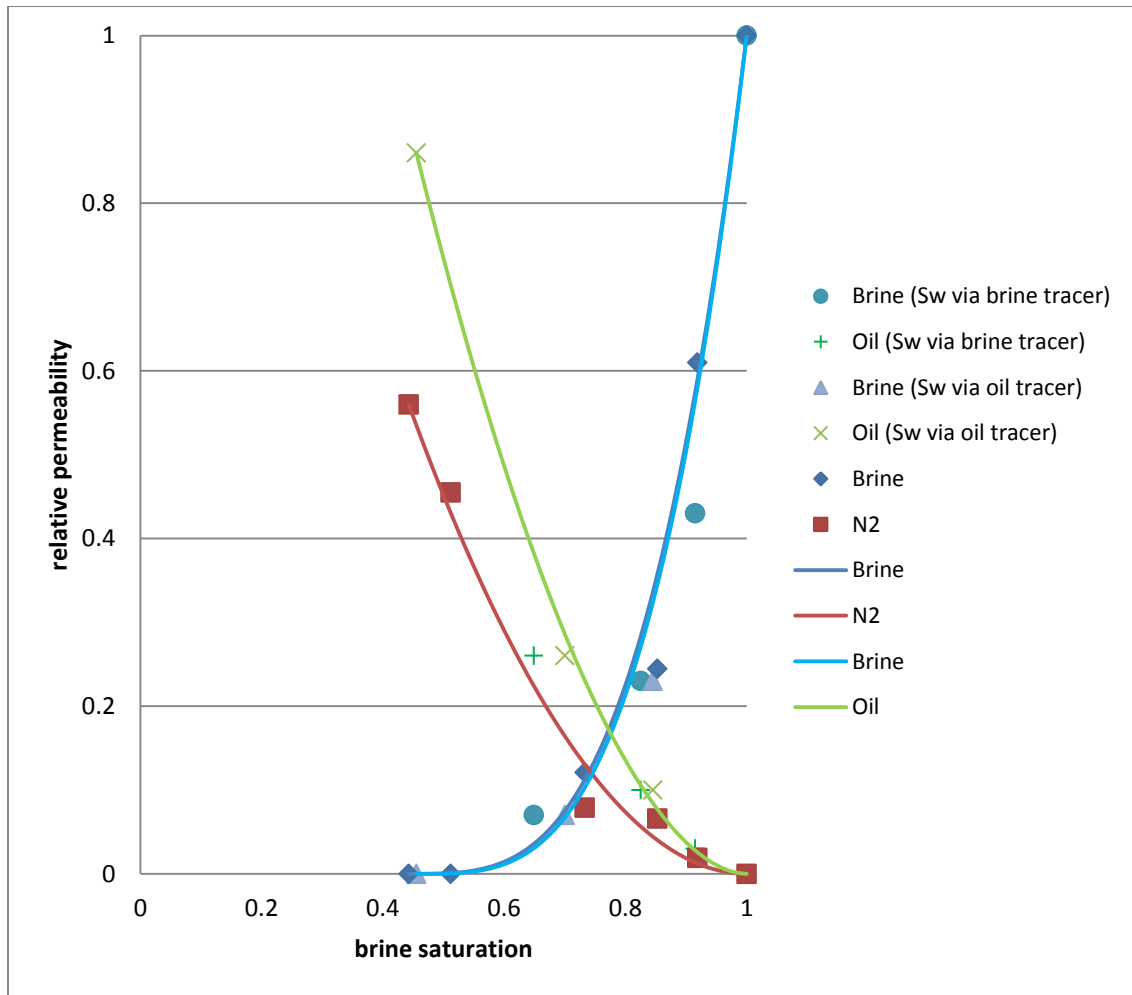


Figure 4-28: Comparison of drainage relative permeabilities of n-decane/brine versus N₂/brine.

4.5.1.5 High Density CO₂ versus n-Decane

Significant differences were observed for both the wetting and the non-wetting phase relative permeabilities. The crossover saturation for the high density CO₂/brine relative permeability curves is lower than that of oil, suggesting a more water-wet condition for the oil/brine experiments. Although the residual water saturations for the two cases are within experimental error, both the overall (across the whole core) as well as the inlet section endpoint relative permeabilities are higher for oil than for the high density CO₂.

As mentioned above, while denser non-wetting phases have a higher end point relative permeability, the apparent difference in wettability between the experiments makes it difficult to establish a correlating parameter for relative permeability. Nevertheless, these results suggest that composition has an effect on relative permeability.

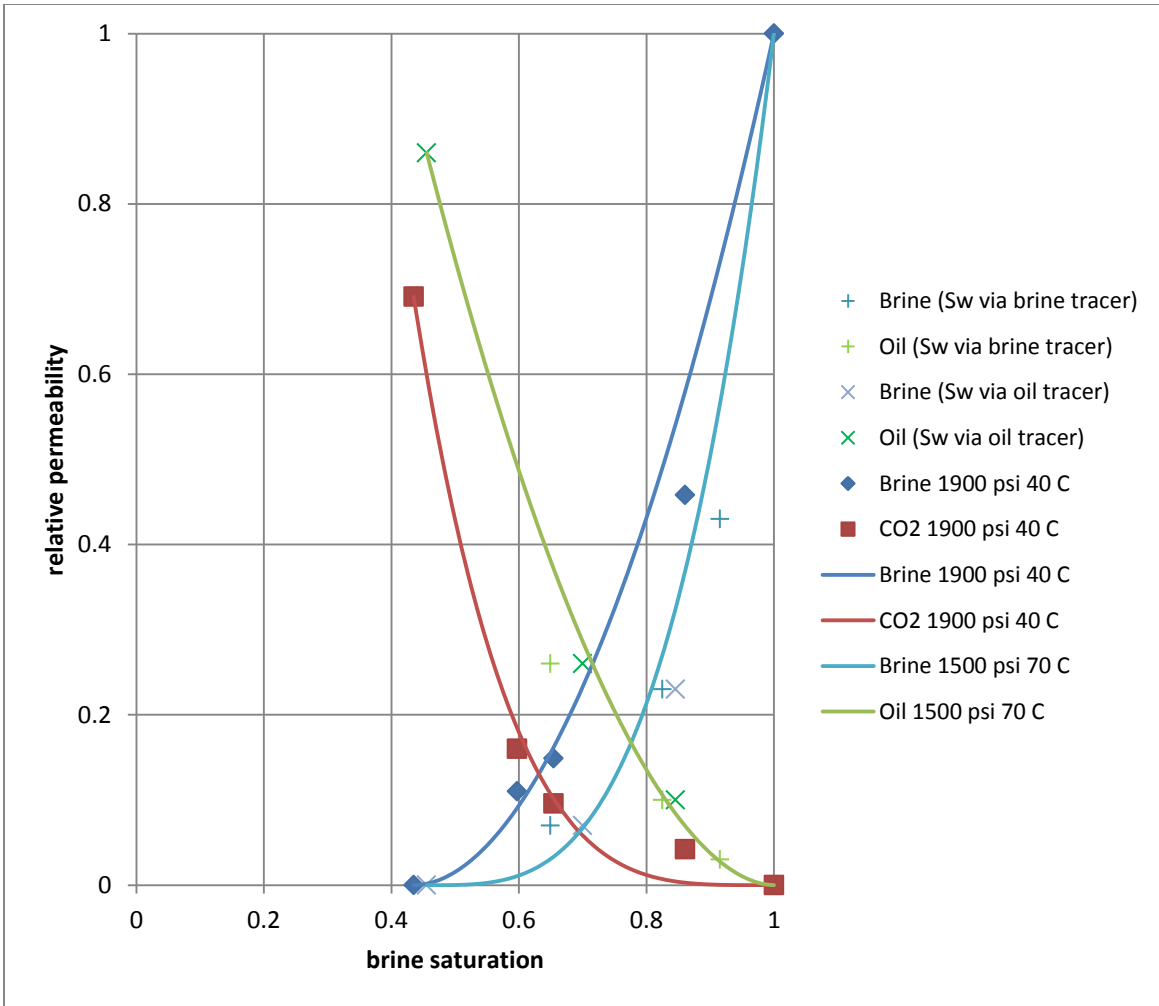


Figure 4-29: Comparison of drainage relative permeabilities of n-decane/brine versus high density CO₂/brine.

4.5.2 Corey Parameters

4.5.2.1 Exponents

A comparison of the Corey exponents for all the drainage experiments is shown in Figure 4-30. Only the exponents for the high density CO₂/brine experiments are significantly different than the other three experiments. As mentioned in the previous sections, it is possible that the high density CO₂ changes the wettability to a less water-wet condition. Whether that is responsible for the difference in drainage Corey exponents is unknown. If that is indeed the case, these results would imply that composition affects relative permeability since wettability is itself a function of composition.

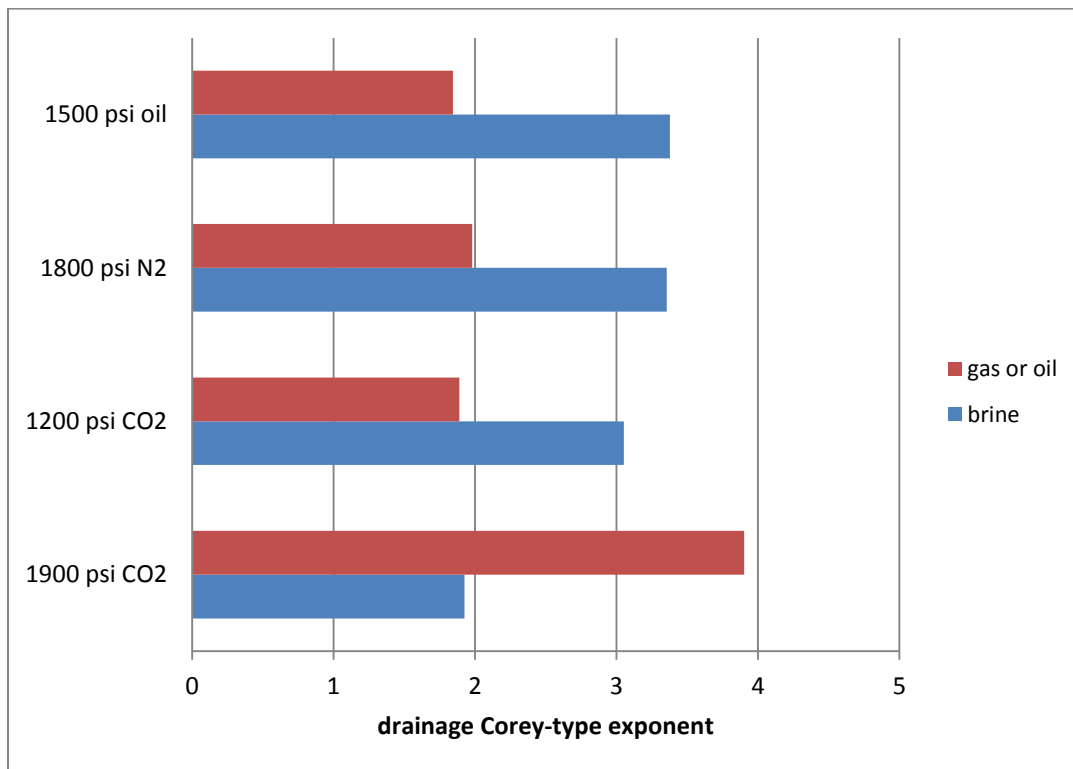


Figure 4-30: Comparison of Corey-type drainage exponents for all experiments.

Only the high density CO₂/brine and the N₂/brine experiments had enough data points during imbibition to fit to a Corey-type curve. The imbibition exponents for those experiments are shown in Figure 4-31. The two non-wetting phase exponents are essentially equal, while a small difference was obtained between the wetting phase exponents. However, as shown in Figure 4-23, the imbibition relative permeability measurements correspond to water saturations closer to 1-S_{gr}. It is not clear if relative permeability measurements performed at water saturations closer to S_{wr} would result in differences for the non-wetting phase exponents.

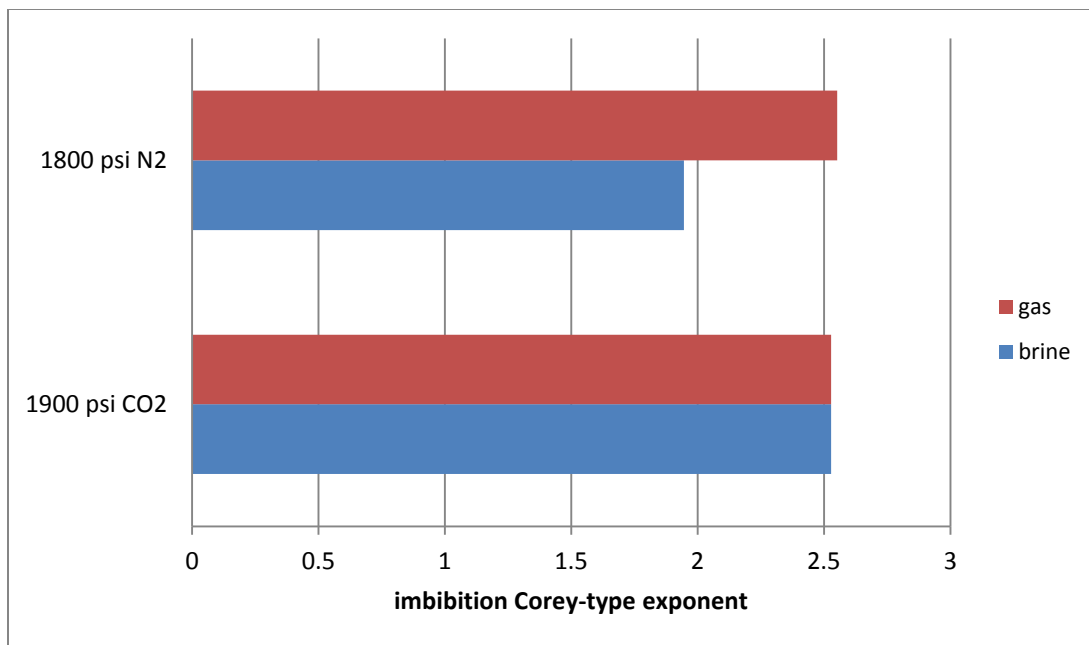


Figure 4-31: Comparison of Corey-type imbibition exponents for the high density CO₂/brine and N₂/brine experiments.

4.5.2.2 Residual Saturations

The residual saturations obtained during the endpoint corefloods were used as the parameters for the Corey-type curve fits. Figure 4-32 shows the values for residual water and residual gas saturations for all experiments. Tracer tests have a typical water saturation error of $\pm 3\%$. Although no tracer tests were performed for the drainage endpoint floods, the residual water saturation was determined by mass balance after the first imbibition flood following the drainage endpoint flood.

All of the residual water saturations were the same within experimental error, except for the low density CO₂/brine experiment. Similarly, the residual gas saturations were the same within experimental error except for the low density CO₂/brine experiment. Since only 57.6 pore volumes of low density CO₂ were injected during the drainage endpoint flood, the higher residual water saturation is likely the result of a fractional flow effect. A lower residual gas saturation would also be expected in that case.

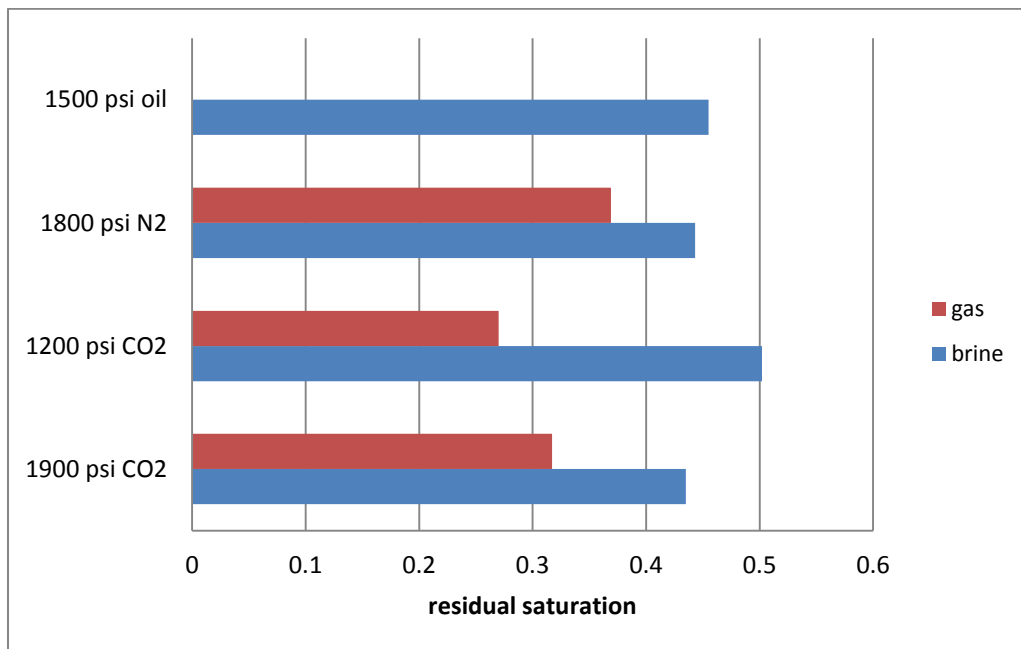


Figure 4-32: Comparison of the residual saturations for all experiments.

These results suggest that compositional changes do not affect residual saturations. Indeed, residual saturations are known to be dependent on capillary number. As shown in Tables 4-4 through 4-14, all of the floods were performed at capillary numbers below 10^{-5} , the critical capillary number for desaturation of the non-wetting phase in Berea sandstone.

No trend emerges between the residual saturations versus the non-wetting phase density nor the non-wetting phase viscosity.

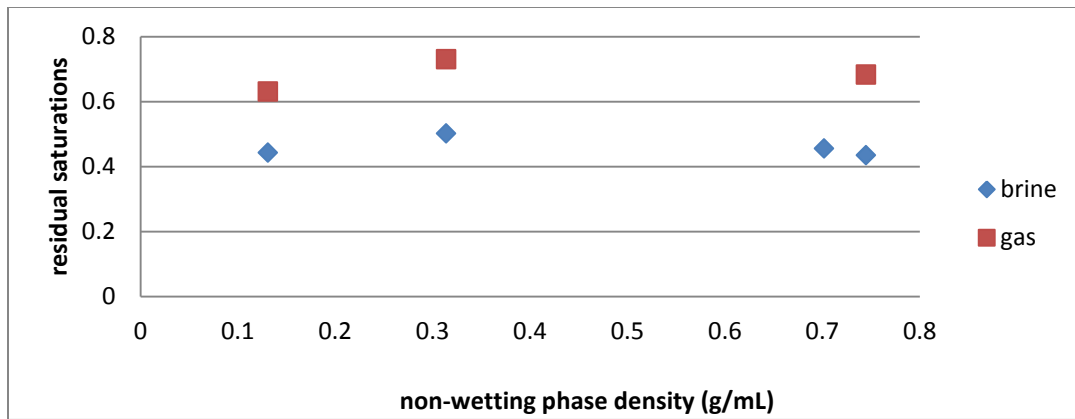


Figure 4-33: Residual saturations versus the non-wetting phase density.

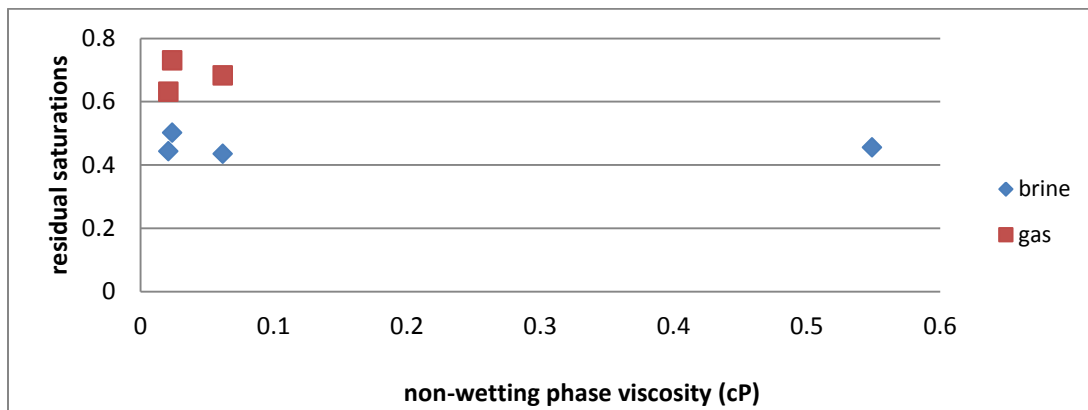


Figure 4-34: Residual saturations versus the non-wetting phase viscosity.

4.5.2.3 Endpoint Relative Permeabilities

The overall (across the whole core) endpoint relative permeabilities obtained during the corefloods were used as parameters for the Corey-type curve fits. Figure 4-35 shows the values for wetting and non-wetting phase endpoint relative permeabilities for all experiments. Although the brine endpoint relative permeability (imbibition) appears to be unaffected by fluid compositions, the non-wetting phase endpoint relative permeabilities (drainage) show significant differences. As discussed in section 4.5.1.4, the true endpoint for the low pressure CO₂ phase is likely higher than that measured during the flood due to fractional flow effects. Nevertheless, these results suggest that at non-wetting phase relative permeability depends on composition.

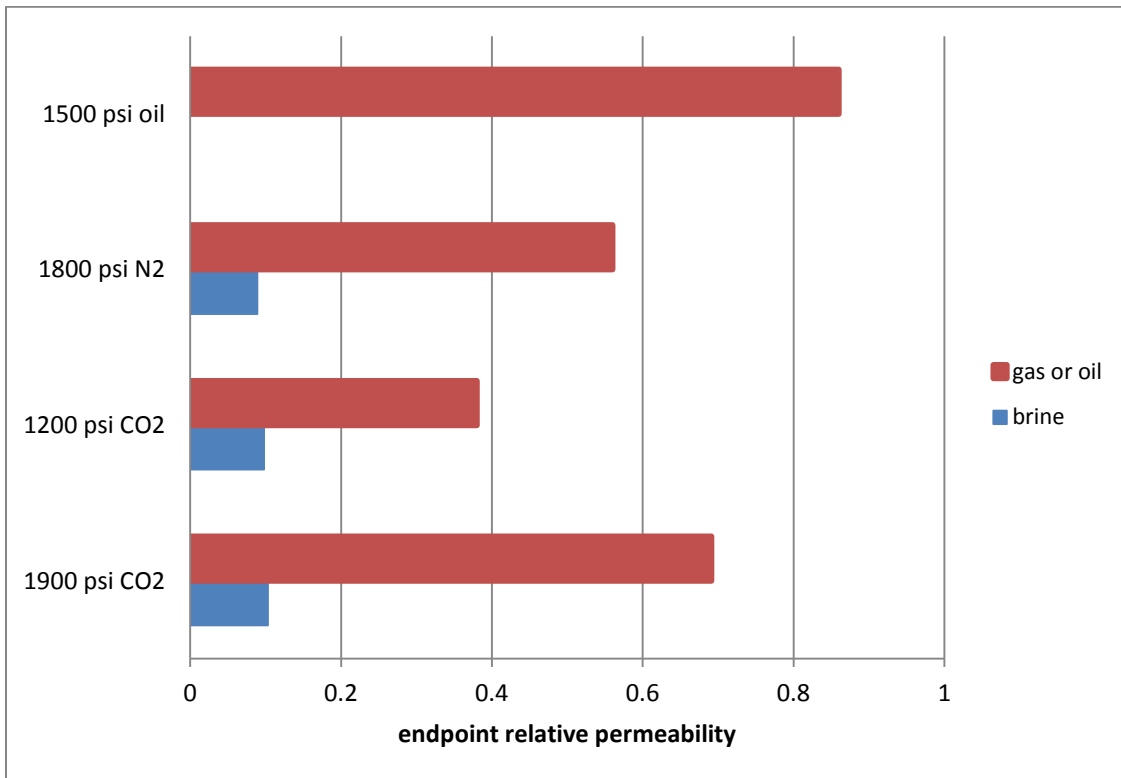


Figure 4-35: Comparison of endpoint relative permeabilities for all experiments.

4.5.3 Sectional Permeabilities

The sectional non-wetting phase permeabilities during drainage were uniform across the core for all brine fractional flows except zero. During the drainage endpoint floods, the relative permeability decreased towards the core outlet (Figure 4-36). Several possibilities could explain this behavior. On one hand, the presence of capillary end effects would result on lower non-wetting phase permeabilities towards the core outlet. However, as detailed in the Methods, the flow rates were chosen to minimize end effects. Another possibility is a fractional flow effect, where for high mobility ratios (as is the case for the CO₂/brine and N₂/brine experiments) not enough pore volumes of the non-wetting were injected. In this case, brine would still be flowing out of the core but at a very low water cut. In addition, the pressure drop across the core would continue to decrease with increasing injected pore volumes. This is one advantage of measuring sectional pressure drops as opposed to only the pressure drop across the core: the inlet section of the core is swept more than the outlet section for every pore volume of fluid injected. Indeed, Figure 4-36 shows a clear difference between the non-wetting phase relative permeabilities measured in the inlet section. In this case, the inlet section saw about 64 pore volumes of n-decane, 136 pore volumes of high density CO₂, 720 pore volumes of N₂, and 228 pore volumes of low density CO₂ during each of the corresponding drainage endpoint floods. Therefore, a comparison of the relative permeabilities for the non-wetting phases measured at the inlet section is likely representative of the true drainage endpoint. Figure 4-36 shows a clear and significant difference between the measured endpoints. Since the viscosity ratio between of the low density CO₂ and brine is essentially equal to that between N₂ and brine (0.035 vs 0.03, respectively), fractional flow theory dictates that about same number of pore volumes are

needed to reach a given saturation. Unfortunately, due to experimental limitations, the number of injected pore volumes of low density CO₂ was significantly less.

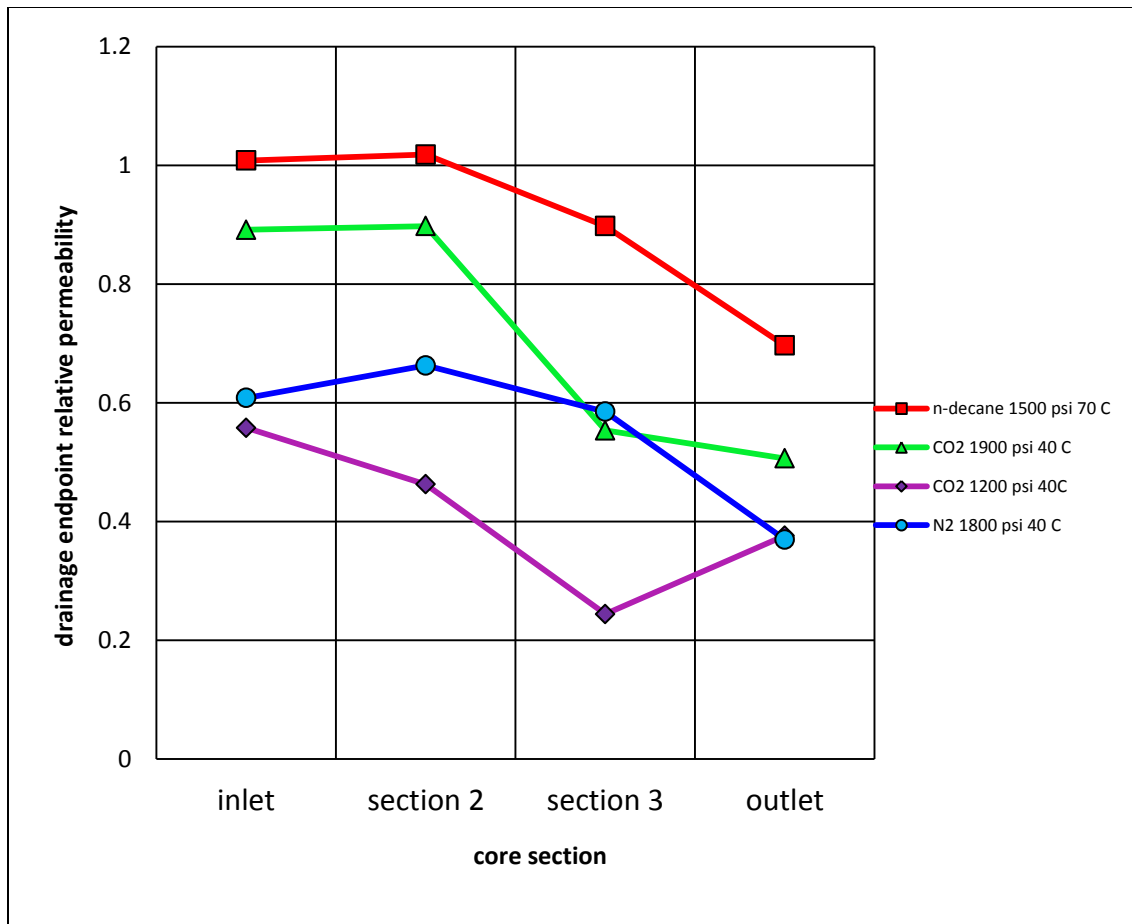


Figure 4-36: Drainage endpoint (at residual brine saturation) sectional comparisons.

Although the data are sparse, non-wetting phase density shows a correlation to the non-wetting phase relative permeability endpoint:

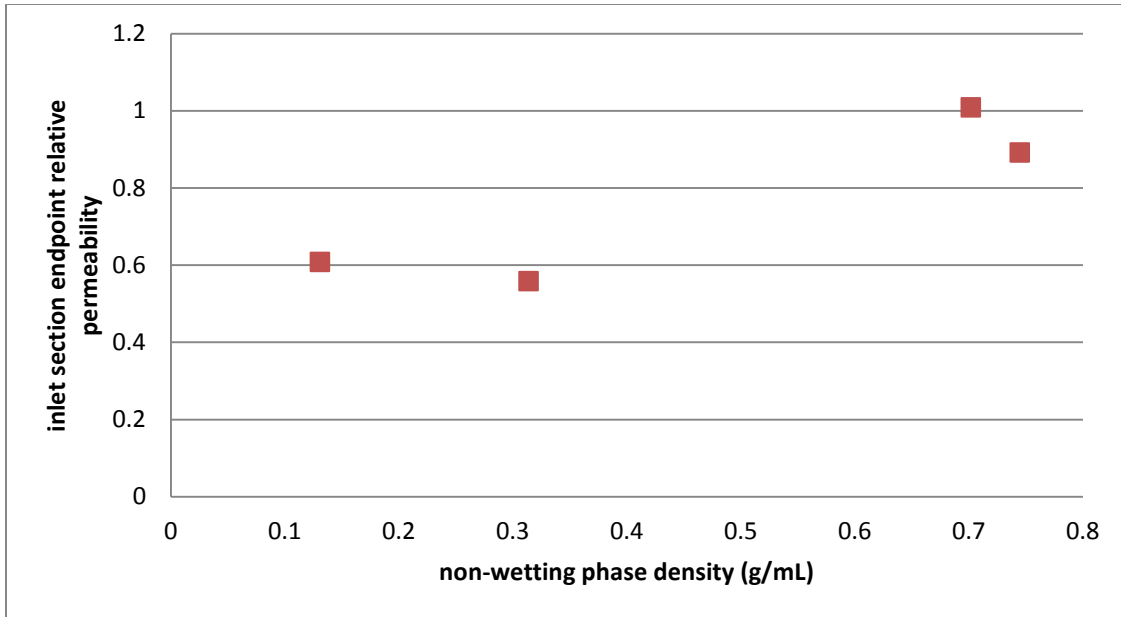


Figure 4-37: Inlet section drainage endpoint relative permeability versus non-wetting phase density.

4.6 LITERATURE COMPARISONS

Several published studies have measured the two-phase relative permeabilities for CO₂, N₂, or oil as the non-wetting phase and brine as the wetting phase. Many of these measurements were done in Berea sandstone. A summary of the fluids and their corresponding fluid properties, the experimental conditions and the authors is listed in Table 4-17. Comparisons of the relative permeabilities measured in this work to those reported in the literature for fluids with similar chemical and physical composition are shown in the following sections.

Table 4-17: Experimental fluid parameters for the research sets.

Fluid	Temperature	Pressure (psi)	Density (g/mL)	Viscosity (cP)	Source
3 wt% Brine	40 C	1200	1.02	0.687	This research
3 wt% Brine	40 C	1800	1.02	0.687	This research
3 wt% Brine	40 C	1900	1.02	0.687	This research
3 wt% Brine	70 C	1500	1.01	0.431	This research
15 wt% Brine	21 C	800	1.18	1.06	Oak, 1990
0.39 wt% Brine	50 C	1798	not listed	not listed	Perrin, 2009
2 wt% NaCl	20 C	1500	1.04	1.04	Chen, 2014
2 wt% CaCl ₂	26 C	1500	not listed	not listed	Dria, 1989
CO ₂	40 C	1200	0.314	0.0240	This research
CO ₂	40 C	1900	0.745	0.0624	This research
CO ₂	50 C	1798	0.608	0.0461	Perrin, 2009
CO ₂	20 C	1500	0.860	0.0850	Chen, 2014
N ₂	40 C	1800	0.131	0.0210	This research
N ₂	21 C	800	0.0635	0.0187	Oak, 1990
n-decane	70 C	1500	0.702	0.549	This research
n-decane	26 C	1500	0.734	0.941	Dria, 1989
mineral oil	21 C	800	0.850	1.77	Oak, 1990

4.6.1 High Density scCO₂/Brine versus Liquid CO₂/Brine Relative Permeabilities in Berea Sandstone

Chen et al. (2014) performed liquid CO₂/brine steady state relative permeability measurements at 1500 psi and 20 C in Berea sandstone. At these conditions, liquid CO₂ has a density of 0.860 g/mL and a viscosity of 0.0824 cP. Water saturations were determined by volume balances at the end of each flood. Chen et al. (2014) measured sectional pressure drops in addition to the whole core pressure drop. The measured liquid CO₂ relative permeabilities during primary drainage varied from about 0.8 for the inlet section to 0.4 for the outlet section. Significant end effects were reported in their work. Although a Rapoport-Leas number of 7.87 was reported for the drainage endpoint flood, instead of using the Darcy velocity ($u = q/A$), they used the interstitial velocity ($v = u/\phi$) to calculate the Rapoport-Leas number. Therefore, the actual Rapoport-Leas number was less than 3. On the other hand, the lower relative permeability for the outlet section could also be the result of fractional flow effects as discussed in this thesis.

Chen et al. (2014) reported lower residual brine saturations and higher residual gas saturations than those found in this thesis. As mentioned in the Methods, determining the correct dead volume for mass balance and/or tracer methods during high pressure floods requires accounting for the expansion of highly compressible fluids (such as CO₂). It is not clear whether that was necessary in the case of Chen et al. (2014). However, if not taken into account, it could explain the lower residual brine saturation reported.

Figure 4-38 shows the primary drainage relative permeability measurements for the high density CO₂/brine studied in this work and those obtained by Chen et al. (2014) for liquid CO₂/brine. The reported liquid CO₂/brine relative permeabilities correspond to those measured for the middle sections of the core and could explain the lower relative permeabilities for liquid CO₂ at water saturations less than 50%. Interestingly, the

crossover point for the liquid CO₂/brine relative permeabilities appears to take place near that for the high density CO₂/brine case. Similar to the high density CO₂/brine experiments, the liquid CO₂/brine measurements were performed above the pressure where CO₂ appears to affect the wettability of quartz (Chiquet, 2007).

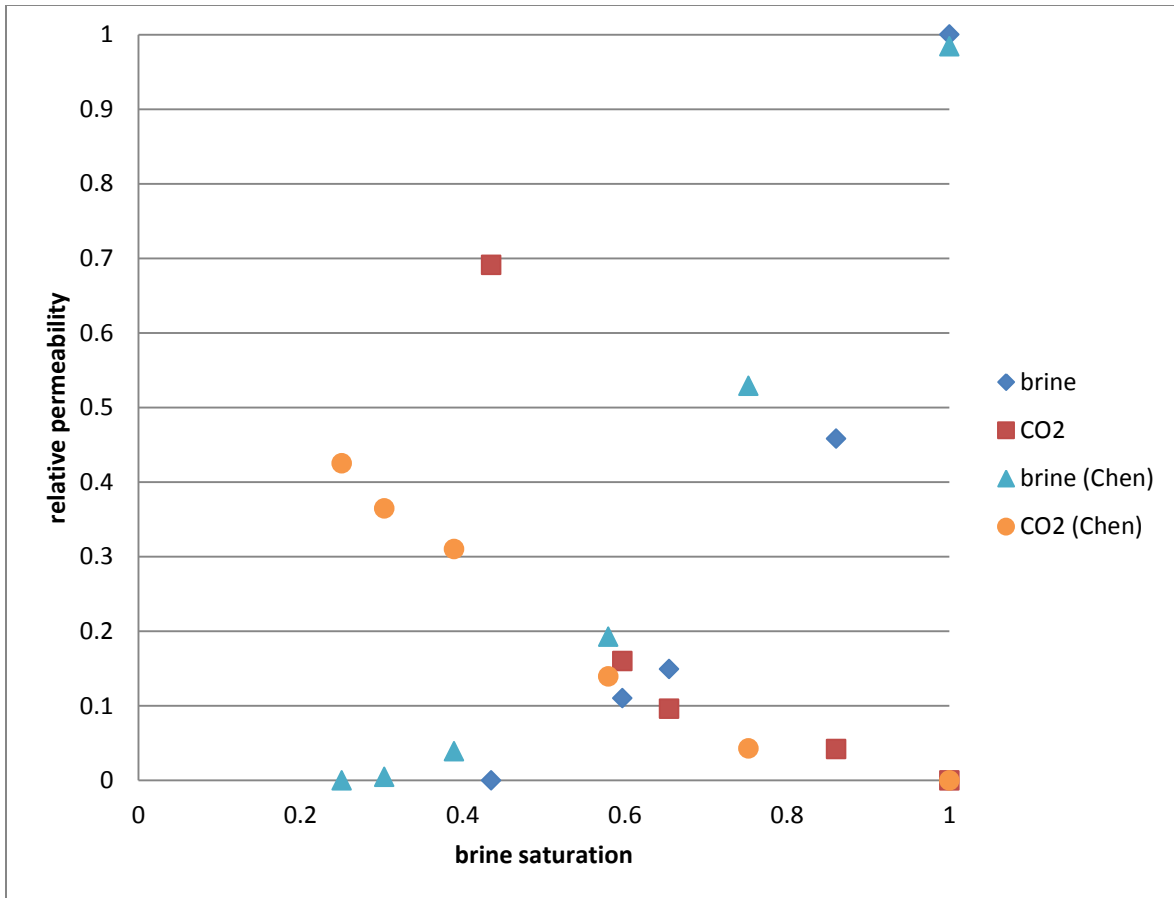


Figure 4-38: High density (1900 psi and 40 C) CO₂ drainage comparison to liquid CO₂ (Chen, 2014).

The primary imbibition relative permeability data of Chen et al. (2014) and this work are significantly different. As shown in Figure 4-39, the water saturation changes from 0.25 at residual water to 0.40 at residual liquid CO₂ saturation, as opposed to a change from 0.435 at residual water to 0.683 at residual high density CO₂ found in this work. On the other hand, the brine endpoints during imbibition varied from 0.08 for sections near the outlet to 0.04 for sections near the inlet of the core. The reason for this trend is not clear since end effects are not expected during imbibition of the wetting phase.

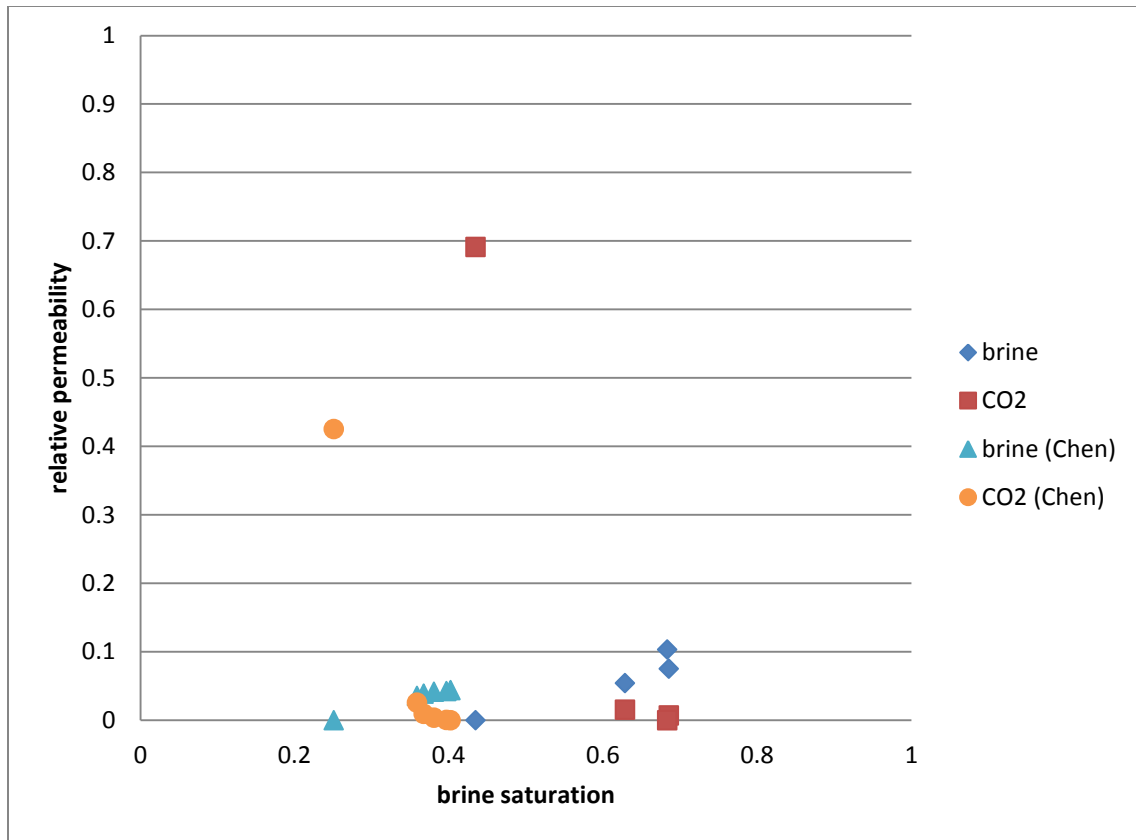


Figure 4-39: High density (1900 psi and 40 C) CO₂ imbibition comparison to liquid CO₂ (Chen, 2014).

4.6.2 n-Decane/Brine in Guelph Dolomite versus High Density CO₂/Brine in Berea Sandstone.

Dria (1989) performed steady state relative permeability measurements using n-decane and brine at room temperature and atmospheric pressure in Guelph dolomite. Only the primary drainage endpoint was measured in the work of Dria (1989); however, primary imbibition data is available. Since no imbibition relative permeabilities were measured for n-decane/brine in this work, the primary imbibition relative permeabilities for the high density CO₂/brine experiments will be used for comparison since the density of CO₂ at those experimental conditions is similar to that of n-decane. Figure 4-40 shows the high density CO₂/brine relative permeabilities in Berea sandstone and the n-decane/brine relative permeabilities in Guelph dolomite (Dria, 1989). Surprisingly, the two experiments show good agreement even though the measurements were done in different rocks. Several similarities might be responsible for the observations; both cores are water-wet at experimental conditions, the densities of the non-wetting phases are similar, and both rocks are fairly well-sorted clastics.

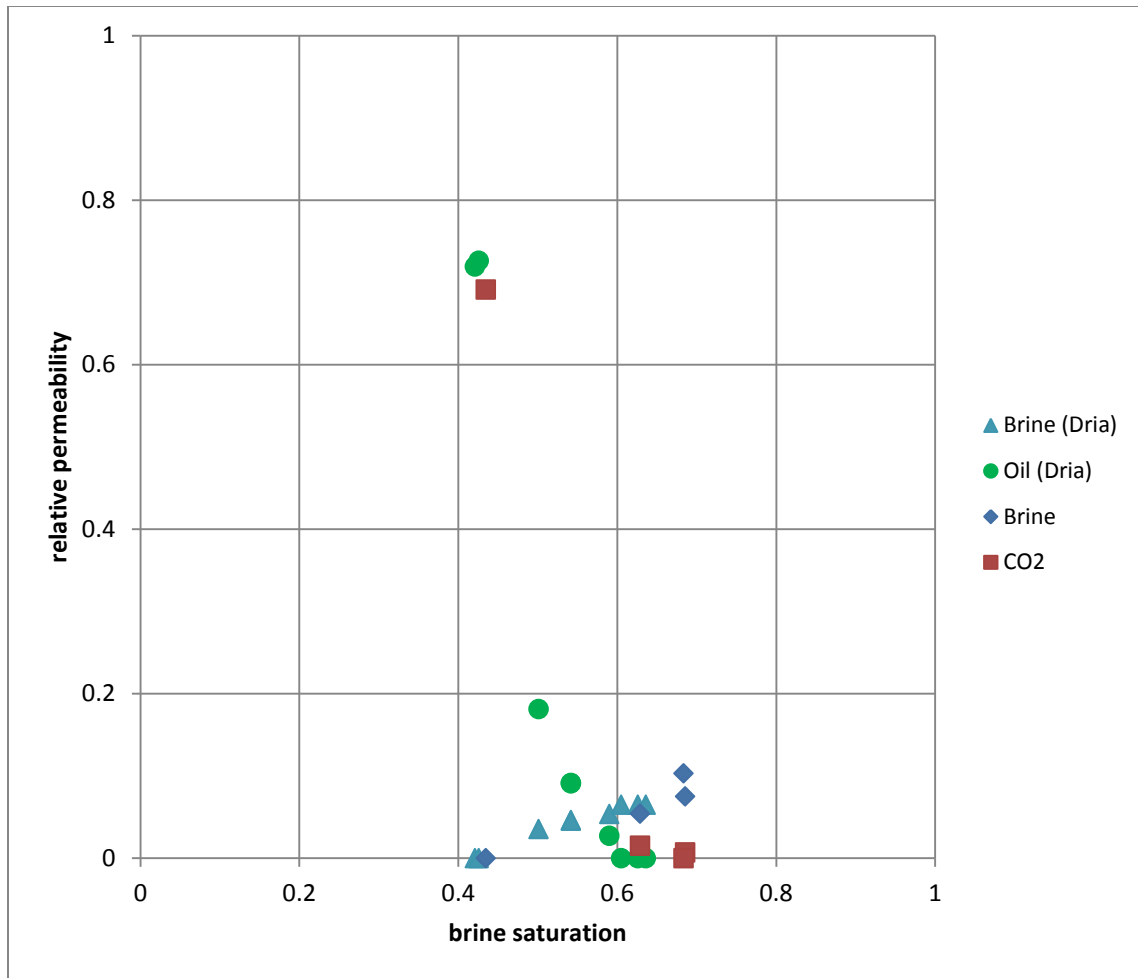


Figure 4-40: n-Decane/brine in Guelph dolomite (Dria, 1989) versus high density CO₂/brine in Berea sandstone.

4.6.3 High Density CO₂/Brine in Berea Sandstone

Perrin et al. (2009) measured steady state primary drainage relative permeabilities for CO₂ and brine in a Berea sandstone core at 1798 psi and 50 C. X-ray scanning was used to determine fluid saturations. Only the pressure drop across the whole core was measured in their experiments. Perrin et al. (2009) reported a flow rate dependent CO₂ endpoint relative permeability, with higher CO₂ relative permeabilities for the higher flow rate. They attributed this to a better displacement efficiency at higher flow rates. Nevertheless, the CO₂ endpoint relative permeability was 0.098 for a CO₂ flow rate of 2.6 ml/min, and 0.063 for a CO₂ flow rate of 1.2 ml/min. These values are strikingly low for Berea sandstone. Careful analysis of their data suggests the presence of significant end effects. For example, the viscosity of CO₂ at their experimental conditions is about 0.046 cP, so at the higher flow rate of 2.6ml/min, the Rapoport-Leas number is only 0.09. This is much smaller than the critical value of 3 required to eliminate end effects. Similarly, the pressure drop across the core during the endpoint flood can be calculated using the reported CO₂ relative permeability, together with the core dimensions and fluid properties. The calculated pressure drop across the core is 0.48 psi. The capillary pressure at residual water saturation can be estimated from the Leverett J-function (Pini and Benson, 2013) and is around 0.5 – 1 psi. This is comparable to the estimated pressure drop across the core and thus corroborates the presence of end effects. The low CO₂ endpoint relative permeability, the high apparent residual water saturation ($S_{wr} = 0.62$) and the observed flow dependence of the CO₂ relative permeability obtained by Perrin et al. (2009) are all consistent with the presence of end effects.

Figure 4-37 shows relative permeabilities for the high density CO₂/brine experiments as well as those measured by Perrin et al. (2009) using CO₂/brine at a flow

rate of 1.2 ml/min. Figure 4-38 shows a comparison with the low density CO₂/brine experiments performed in this research.

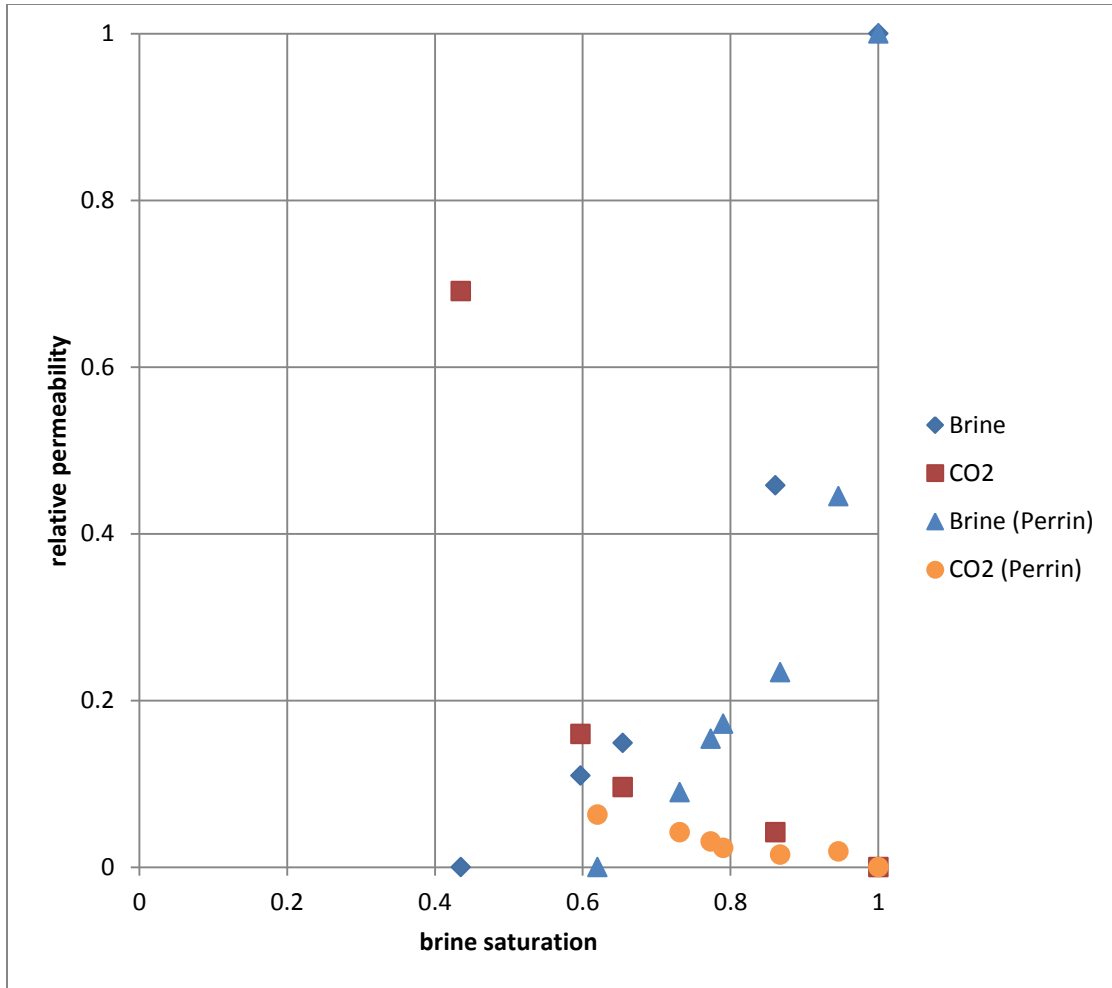


Figure 4-41: Drainage relative permeabilities for high density scCO₂/brine and scCO₂/brine (Perrin, 2009).

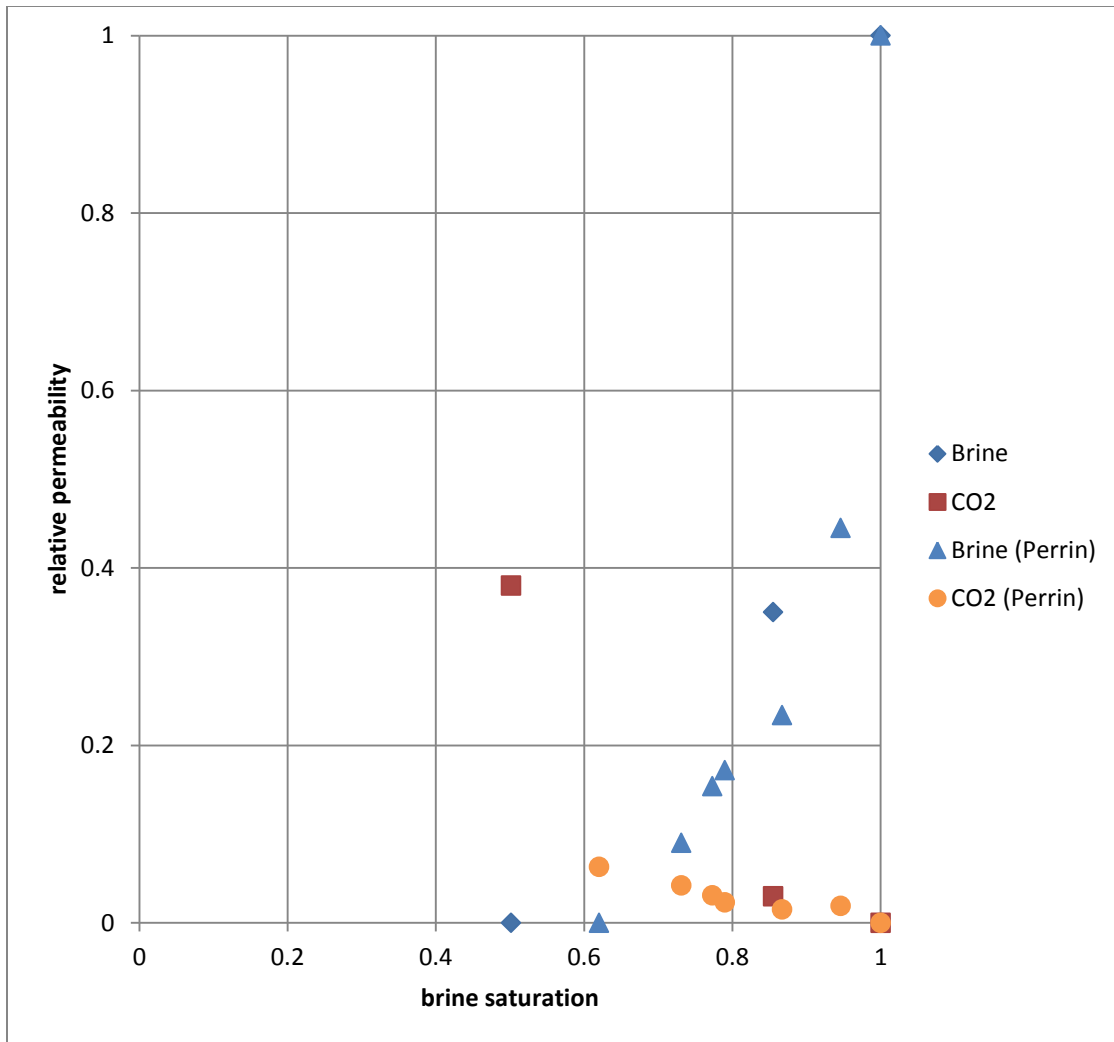


Figure 4-42: Drainage relative permeabilities for low density scCO₂/brine and scCO₂/brine (Perrin, 2009).

4.6.4 N₂/Brine in Berea Sandstone

4.6.4.1 Drainage

Oak et al. (1990) measured steady state primary drainage relative permeabilities for N₂ and brine in a Berea sandstone core at 800 psi and 21 C. X-ray scanning was used to determine fluid saturations. Although only one pressure drop was measured in these experiments, the core was placed in between two other cores made of the same rock. The pressure drop was measured across the center core, away from the inlet and outlet, reducing the influence of end effects on the measurement.

Figure 4-43 shows the N₂/brine primary drainage relative permeabilities measured by Oak et al. (1990) and those measured in this thesis. The two experiments show good agreement in general. However, the residual water saturation measured by Oak et al. (1990) is lower than that measured in this work. Similarly, the N₂ endpoint relative permeability is higher in experiments of Oak et al. (1990). As mentioned above, the core sections closer to the outlet showed lower gas endpoint relative permeability, likely due to fractional flow effects. However, the sections closer to the inlet had an endpoint relative permeability closer to that measured by Oak et al. (1990). This suggests that the differences between the data in this thesis and that by Oak et al. (1990) are due to fractional flow effects.

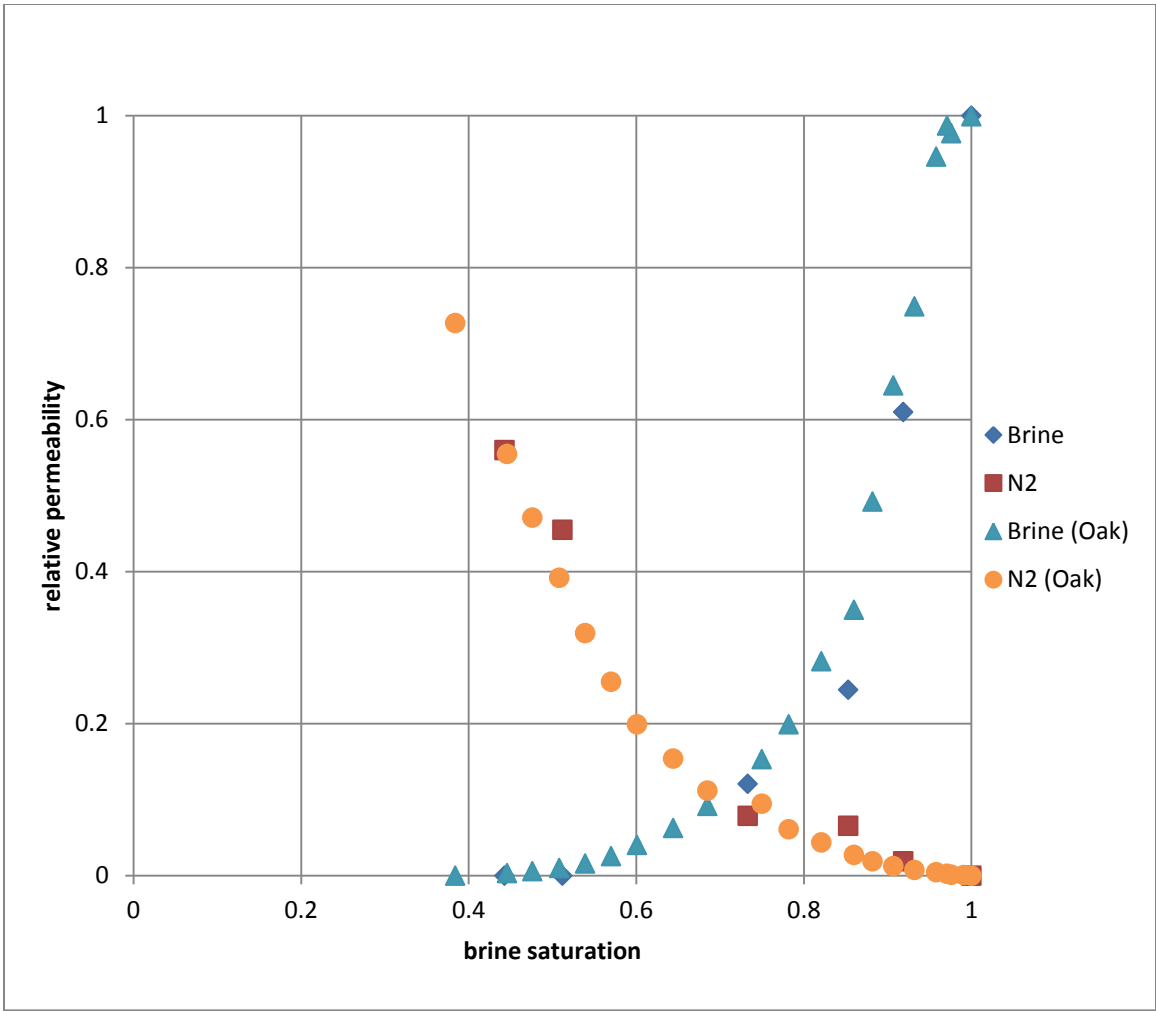


Figure 4-43: Drainage relative permeabilities for N₂/brine from this research and N₂/brine (Oak, 1990).

Figure 4-44 shows the low density CO₂/brine relative permeabilities measured in this work and the N₂/brine relative permeabilities measured by Oak et al. (1990). As discussed above, the physical properties of the low density CO₂ are closer to those of N₂ at experimental conditions. Although the data for the CO₂/brine experiment are scarce, a good agreement between the two can be seen.

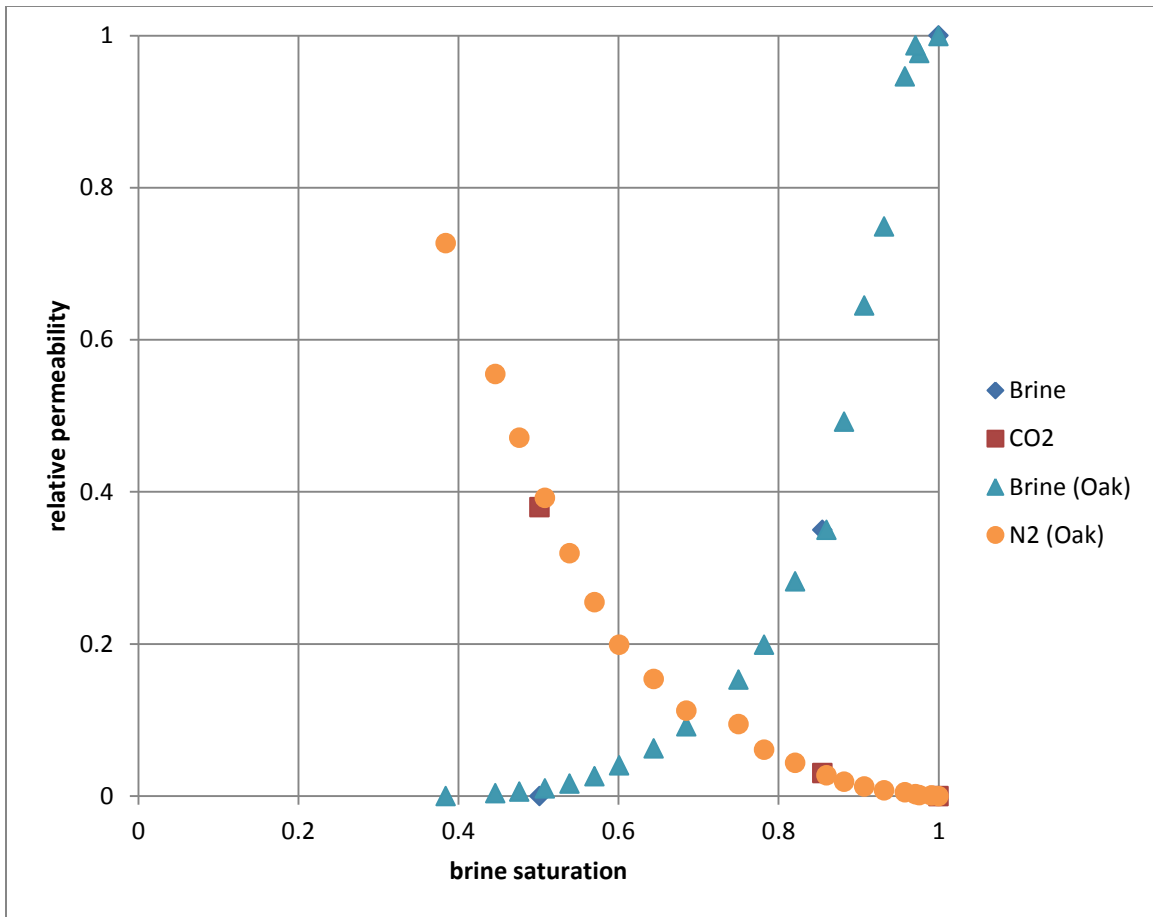


Figure 4-44: Drainage relative permeabilities for low density CO₂/brine from this research and N₂/brine (Oak, 1990).

4.6.4.2 Imbibition

The imbibition relative permeabilities measured in this research also show good agreement with those measured by Oak et al. (1990) (Figure 4-45). The residual water saturation is higher than that measured by Oak et al. (1990), while the residual gas saturation is lower than that measured by Oak et al. (1990). This is consistent with hysteretic effects due to the sections closer to the core outlet being at a higher than residual brine saturation.

Overall, a good agreement between the two N₂/brine relative permeability measurements was found.

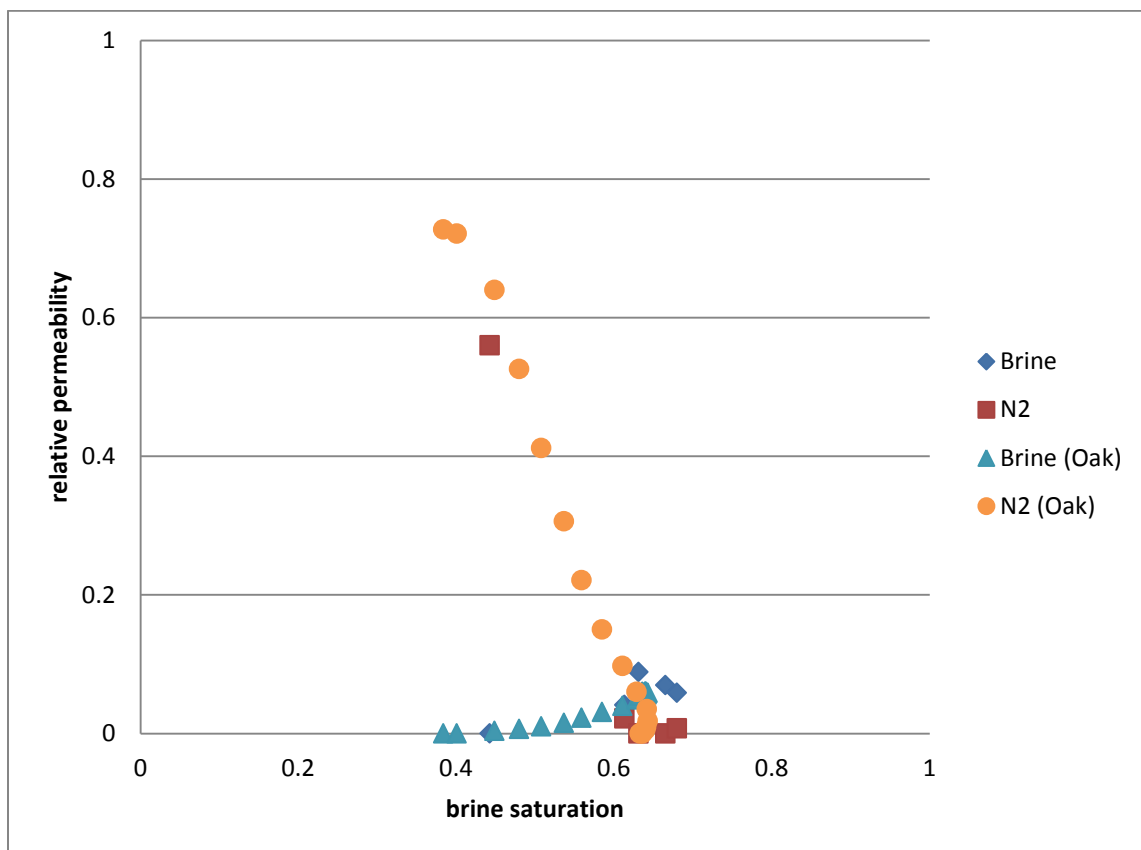


Figure 4-45: Imbibition relative permeabilities for low density CO₂/brine from this work and N₂/brine (Oak, 1990).

4.6.5 Oil/Brine Drainage in Berea Sandstone

Oak et al. (1990) also measured the relative permeabilities for oil/brine. Figure 4-46 shows the n-decane/brine drainage relative permeabilities measured in this research, for comparison, the oil/brine data by Oak et al. (1990) is also shown. Several interesting features can be seen. First, the oil endpoint relative permeabilities agree with each other. However, the corresponding water saturations appear to be significantly different as shown in Table 4-18. On the other hand, if the water saturations measured using the salinity tracer are used, the n-decane/brine relative permeabilities show good agreement with those measured by Oak et al. (1990). The residual water saturation for the n-decane/brine experiments was measured using the oil tracer (see Methods for more details). As seen in it Figure 4-46, the water saturations obtained with the salinity tracer are slightly lower than that obtained with the oil tracer for the same flood. Therefore, it is possible that the disagreement in residual saturations is due to the discrepancy between the salinity and the oil tracer. This remains to be investigated.

Table 4-18: Comparison of oil and brine flooding residual brine saturations.

Oil	Temperature	Pressure (psi)	Residual Brine Saturation	Source
n-decane	70 C	1500	0.46	This research
mineral oil	21 C	800	0.26	Oak 1990

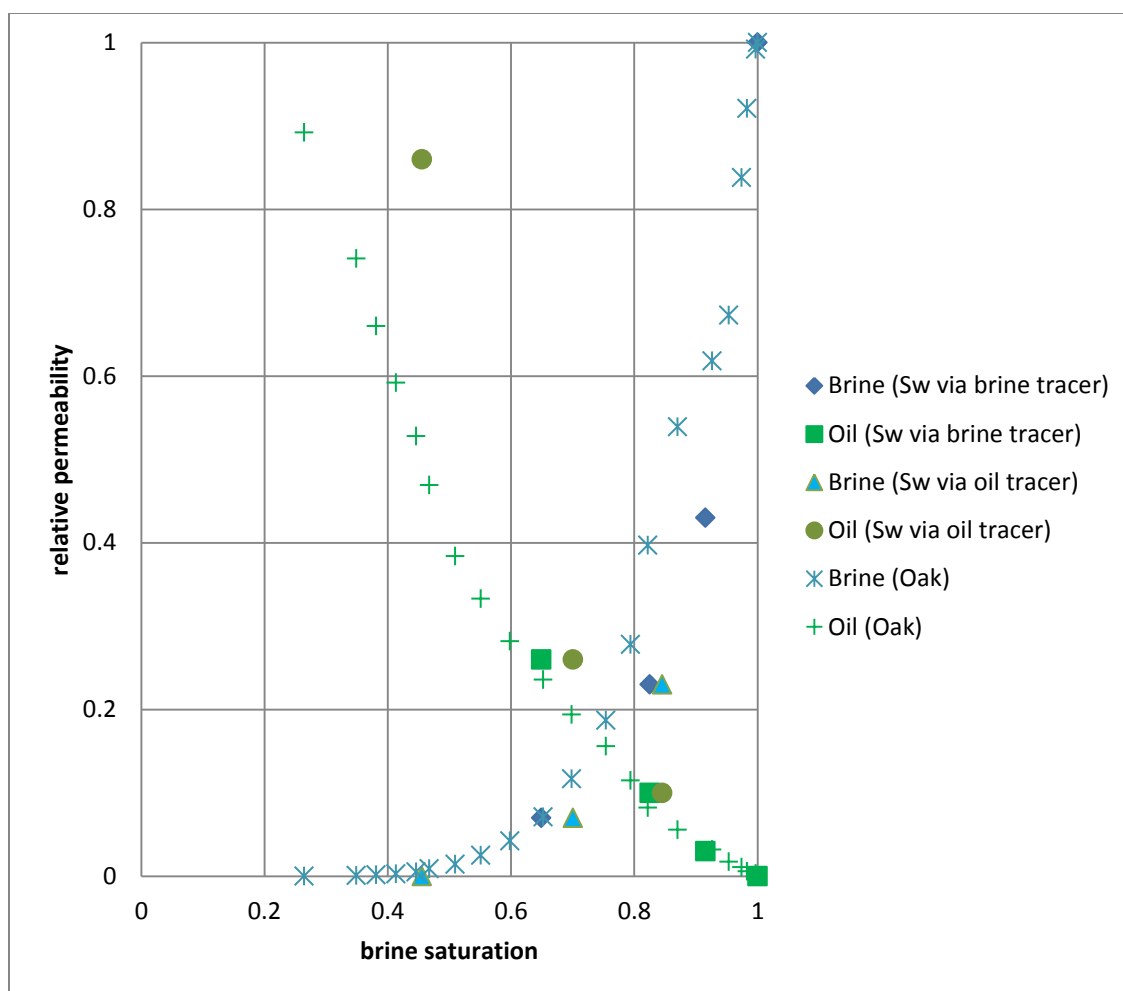


Figure 4-46: Drainage relative permeabilities for n-decane/brine from this research and mineral/oil brine (Oak, 1990).

Chapter 5 - Summary, Conclusions, and Future Work

5.1 SUMMARY AND CONCLUSIONS

Several previous studies suggested a dependence of the relative permeability on fluid composition. However, no single study focused on that objective was available in the literature and no rigorous assessment was possible based on available data. The goal of this research was to explore the role of composition on relative permeability by performing two-phase steady-state relative permeability measurements. The effect of changing fluid composition was studied by using different fluid pairs: CO₂/brine, N₂/brine and n-decane/brine. In addition, the experiments were performed at two different pressures for the same fluid pair, CO₂/brine since pressure also changes fluid properties such as density that may have an effect on the relative permeability. To reduce the complexity of the problem, the same brine was used in all experiments.

A very important part of this study was the establishment of the experimental procedures needed to ensure accurate measurements of the relative permeability. These are difficult measurements subject to many experimental artifacts and complications. For example, a special effort was made to reduce capillary end effects in these experiments. These procedures are described in detail in Chapter 3.

The longer term goal of this research is to extend the measurements to three-phase flow and to explore more significant compositional changes associated with less common but still important fluids such as solvents used to remediate liquid blocking in both conventional and unconventional reservoirs.

Although many studies have reported relative permeability measurements for N₂/brine, CO₂/brine or oil/brine, this is the first experimental study where the relative

permeability for different fluids was measured using precisely the same methodology. The same core was used for all experiments allowing for a direct comparison between the different fluids. Furthermore, special care was taken in this study to eliminate experimental artifacts that affect relative permeability measurements. In particular, experiments were performed at a high Rapoport-Leas number to minimize capillary end effects. Fractional flow effects, e.g. not being able to flow enough pore volumes to reach residual saturation throughout the whole core, while not eliminated, were circumvented by measuring sectional pressure drops, as opposed to only the pressure drop over the whole core. Ideally, the sectional pressure drops would be accompanied by sectional saturation measurements, for example, using resistivity or X-ray scanning methods, and this remains a longer term goal of this research but it also adds significant complications and limitations using currently available equipment.

Comparing the results in this thesis to published relative permeability data clearly shows that if not addressed, these experimental artifacts can lead to significantly lower relative permeabilities, in particular for the end point value, and also in high apparent residual water saturations. Several examples in the literature of unusually low CO₂ endpoint relative permeabilities in Berea sandstone are likely the result of end effects due to a low Rapoport-Leas number: Akbarabadi and Piri (2013) ($N_{RL} = 0.3$), Krevor et al. (2012) ($N_{RL} = 0.345$), Levine et al. (2013) ($N_{RL} = 2.19$), Perrin et al. (2009) ($N_{RL} = 0.09$). This is a very serious limitation of much of the relative permeability data currently available in the literature and was largely overcome by this study using similar fluids and conditions.

Compositional effects could affect relative permeability in a number of different ways. For example, one could imagine that for different interfacial tensions and/or wettabilities, the end point relative permeability could change. On the other hand,

compositional changes could result in different residual saturations and thus different relative permeabilities. It is well known that residual saturation depends on the trapping number, which in turns depends on composition through interfacial tension and density. For the results shown in Chapter 4, the apparent residual saturation for the different experiments varies by about 2%. This is within the experimental error expected from the tracer method. Although residual water saturation depends on the trapping number, all of the measurements were performed within the same order of magnitude for the trapping number. Thus, the results suggest that the compositional effects on residual water saturation are minimal.

On the other hand, the series of corefloods performed in this research showed a difference in the relative permeabilities for the different fluid pairs. In particular, the effect on the non-wetting phase relative permeability appears more pronounced near residual water saturation with the denser fluids displaying a higher endpoint relative permeability (Figure 4-33). At experimental conditions, n-decane is less dense than the dense CO₂, yet the oil has a higher endpoint permeability. Fractional flow effects could be responsible for this behavior; the viscosity of n-decane is about 9 times higher than that of the dense CO₂ and thus fewer pore volumes of n-decane, compared to CO₂ are needed to reach residual water saturation. This can result in an apparent lower end point for CO₂. However, a comparison of the relative permeabilities measured for n-decane and CO₂ in the inlet section of the core, where a sufficient pore volumes have been injected based on the steady state pressure data, shows that the oil relative permeability is higher than that for CO₂. This suggests that density is not a good correlating parameter for relative permeability. Yuan and Pope (2011) proposed the use of the molar Gibbs free energy to correlate relative permeability with composition based on the limited data available at that time under dissimilar conditions. Figure 5-1 shows the endpoint relative

permeability data from this research as a function of molar Gibbs free energy. Although only three reliable end point permeabilities were measured in this study (low density CO₂ is excluded from Figure 5-1), a reasonable correlation between endpoints and the corresponding Gibbs free energy can be seen:

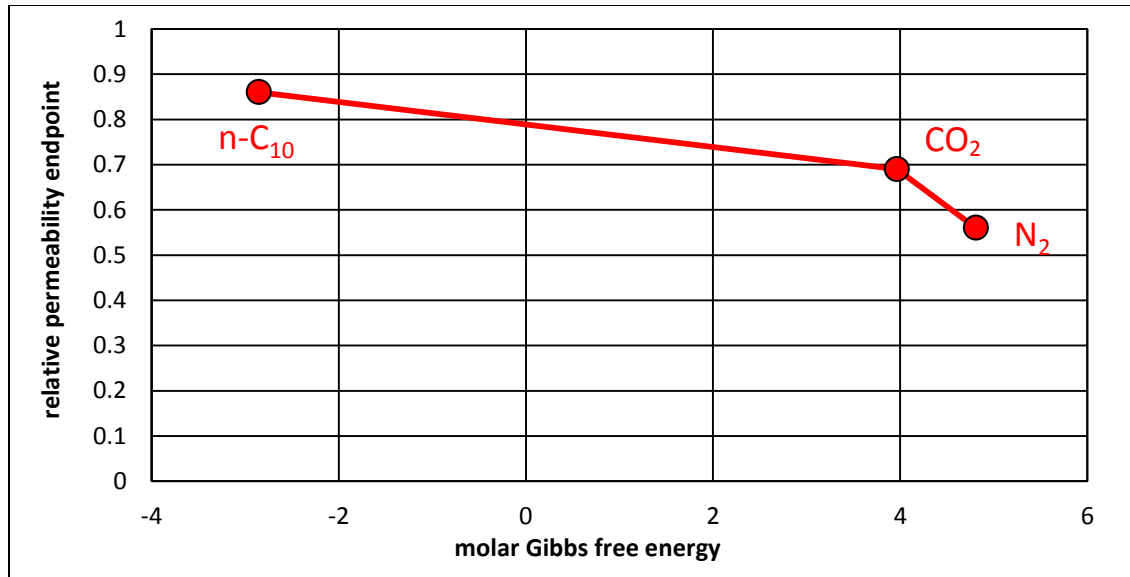


Figure 5-1: Endpoint relative permeability and molar Gibbs free energy for all non-wetting fluids used in this study.

Overall, the results of this research suggest that relative permeability is a function of composition. This concept goes against the standard assumption that relative permeabilities are independent of the fluid composition for a given rock. This possible dependence has important implications for a number of very significant applications and thus warrants the attention and effort of more researchers.

5.2 FUTURE WORK

Although the results of this research suggest the existence of compositional effects on relative permeability, it remains unclear what physical properties of the

fluids/rock system are responsible for these effects. Additional coreflood experiments with other fluids are needed to shed further insight on this complicated phenomena. The study of brine composition should be included in these studies since it is known to affect the relative permeability in some cases (the so called low salinity effect). Relative permeability measurements using solvents such as alcohols, glycols and dimethyl ether now being used as stimulation fluids would be even more interesting and valuable.

Only two-phase flow was studied in this research. The inclusion of an additional phase can result in more complex compositional changes. Previous three-phase relative permeability measurements studies are scarce. Oak (1990) and Dria (1989) measured the relative permeabilities for gas/oil/water. Although differences were observed between N₂/dodecane/brine (Oak, 1990) and CO₂/decane/brine (Dria, 1989), the measurements were performed in different rocks and at different experimental conditions. A systematic three-phase relative permeability study in the same rock while varying the gas and/or brine composition or the pressure would be of significant value considering the importance of the applications to both hydrocarbon recovery and geological storage of greenhouse gases among other applications.

Neshat (2016) recently developed an integrated relative permeability and capillary pressure model that includes the effect of composition and hysteresis for both two and three-phase flow. He used Gibbs free energy to interpolate all of the model parameters and demonstrated the advantage of using this approach in compositional reservoir simulations, especially when there are large compositional and phase behavior changes such as when solvents are injected. This approach needs to be verified or modified using systematic and reliable experimental data, but this remains a difficult and challenging problem.

Appendix

HIGH DENSITY CO₂ AND BRINE FLOODING

Drainage Regime

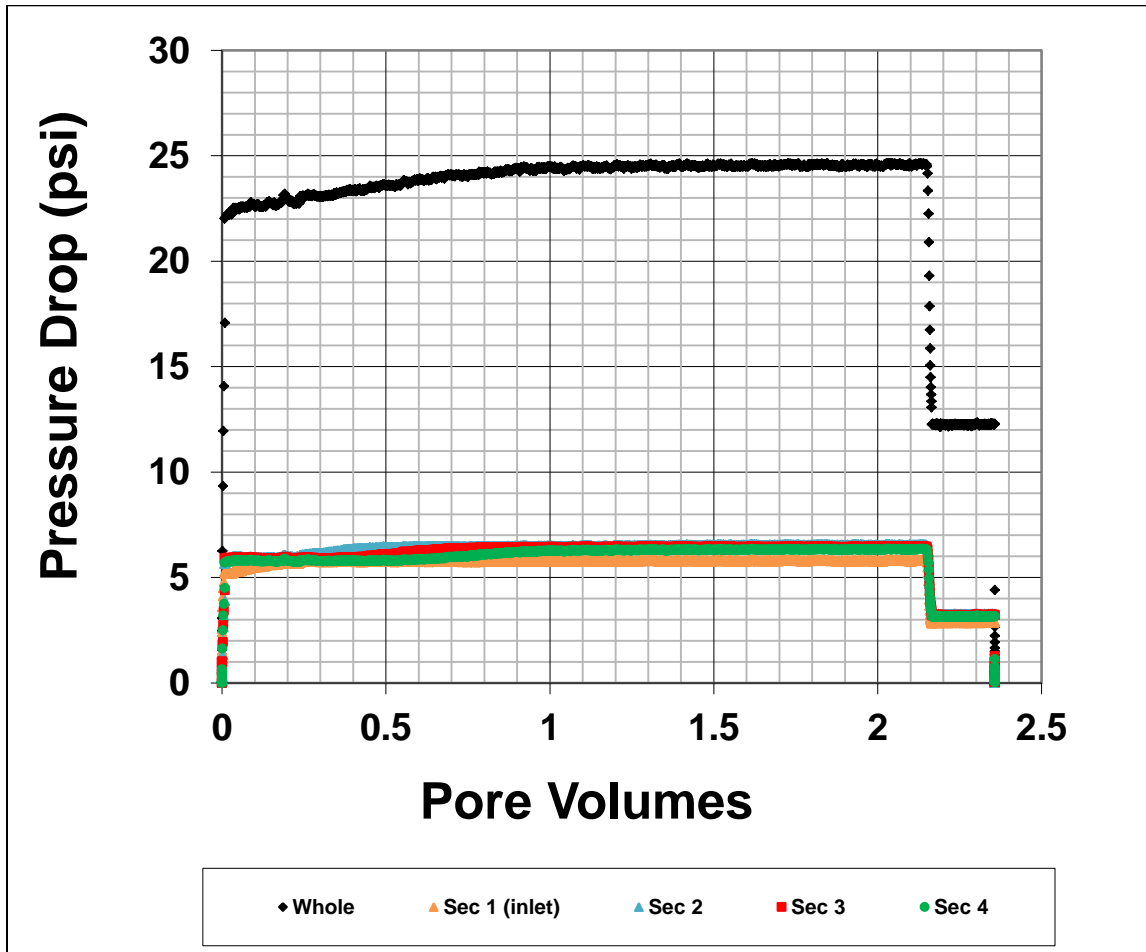


Figure A-1: CO₂-saturated brine flood, 1881 psi 40 C.

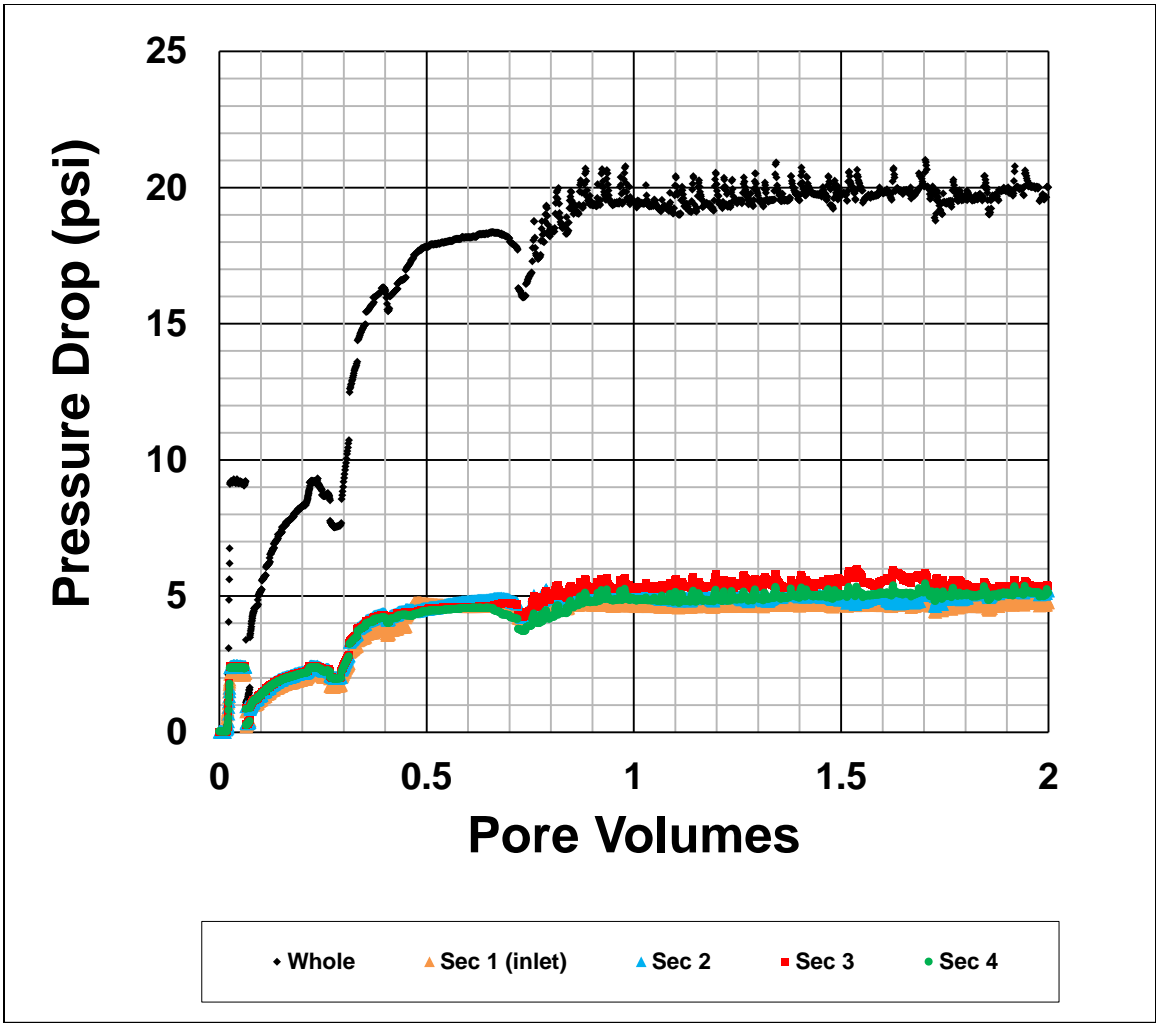


Figure A-2: Brine fractional flow at 0.5, 1894 psi 40 C.

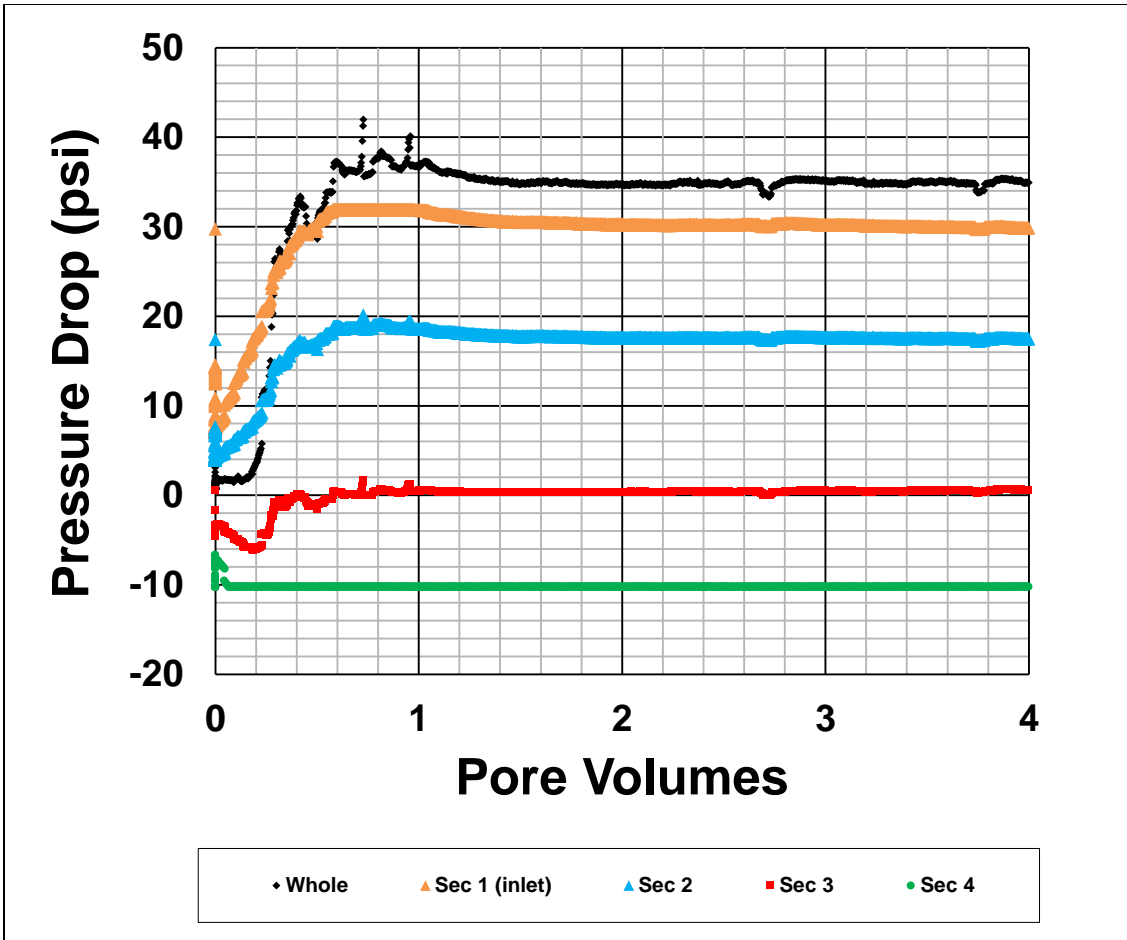


Figure A-3: Brine fractional flow at 0.114, 1900 psi 40 C. Sectional pressure taps became plugged during this flood.

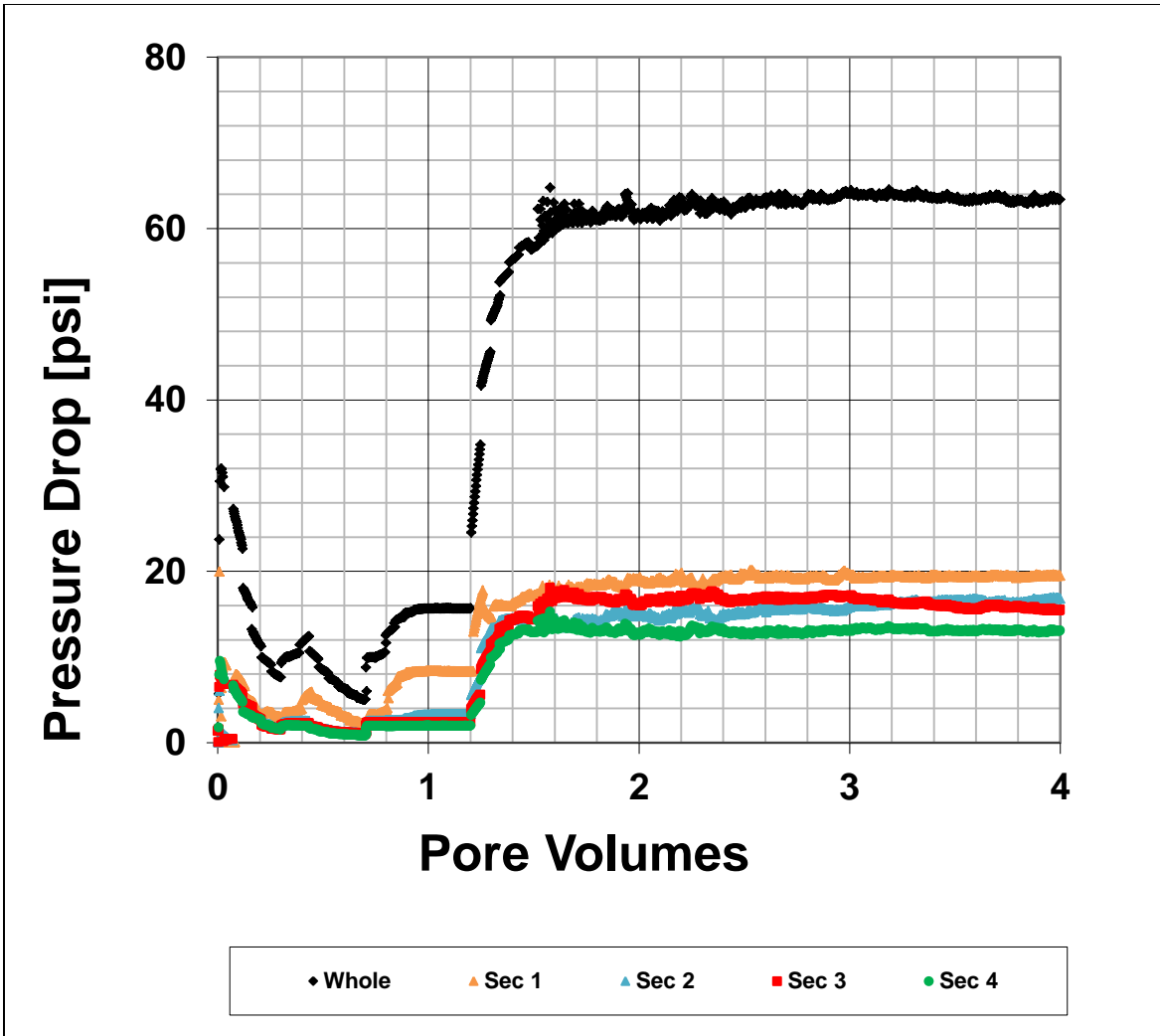


Figure A-4: Brine fractional flow at 0.125, 1858 psi 40 C.

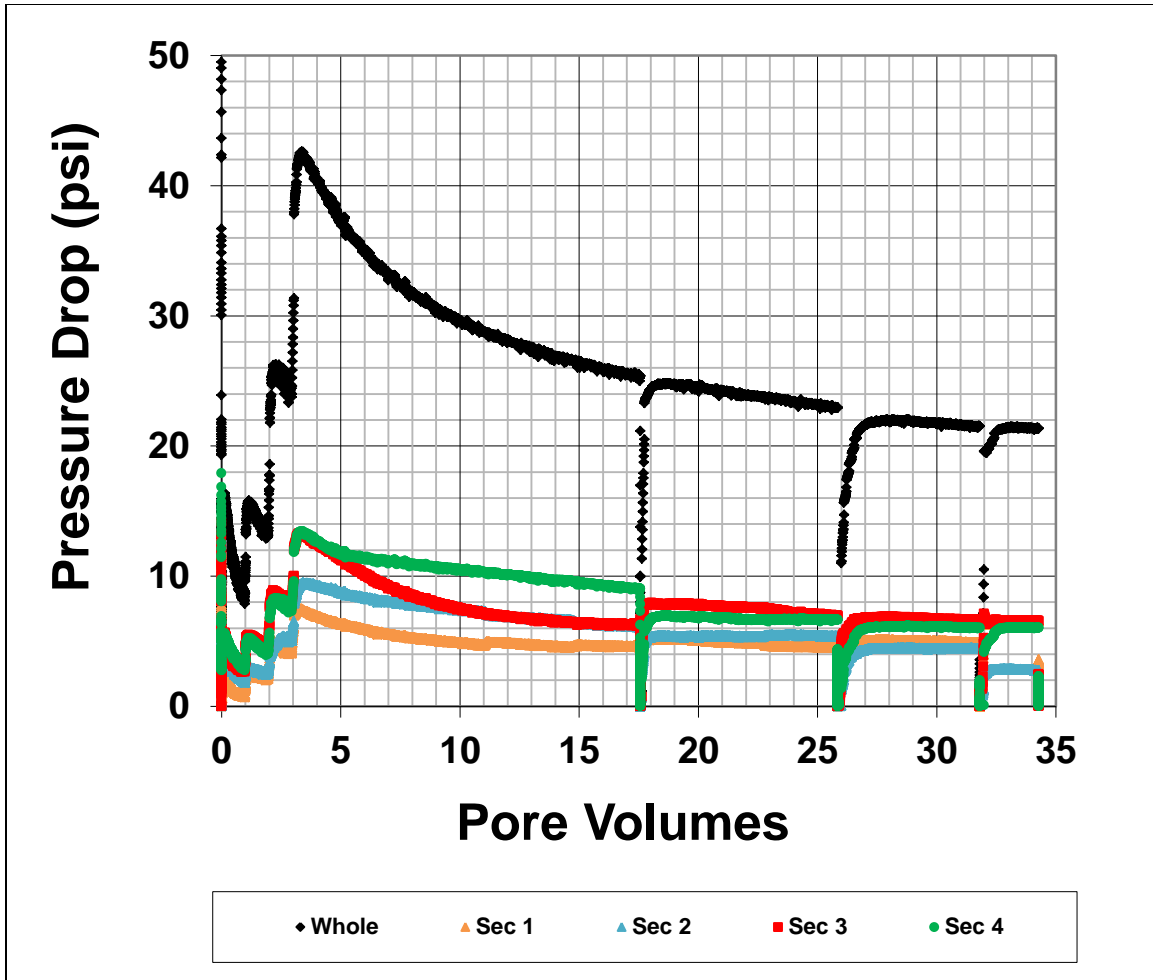


Figure A-5: Brine fractional flow at zero, 1875 psi 40 C. The discontinuities of pressure drop indicate when the apparatus was switched to a full accumulator of CO₂.

Imbibition Regime

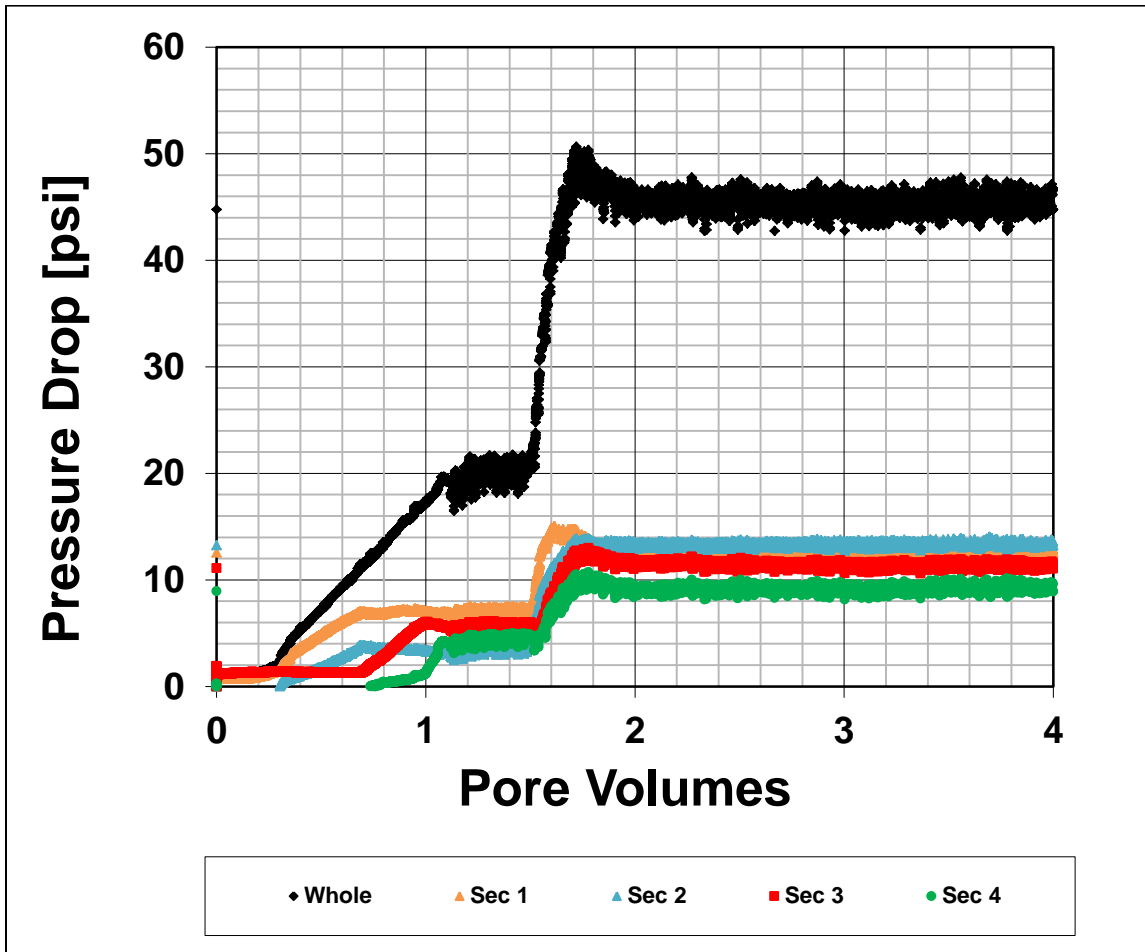


Figure A-6: Brine fractional flow at 0.25, 1876 psi 40 C.

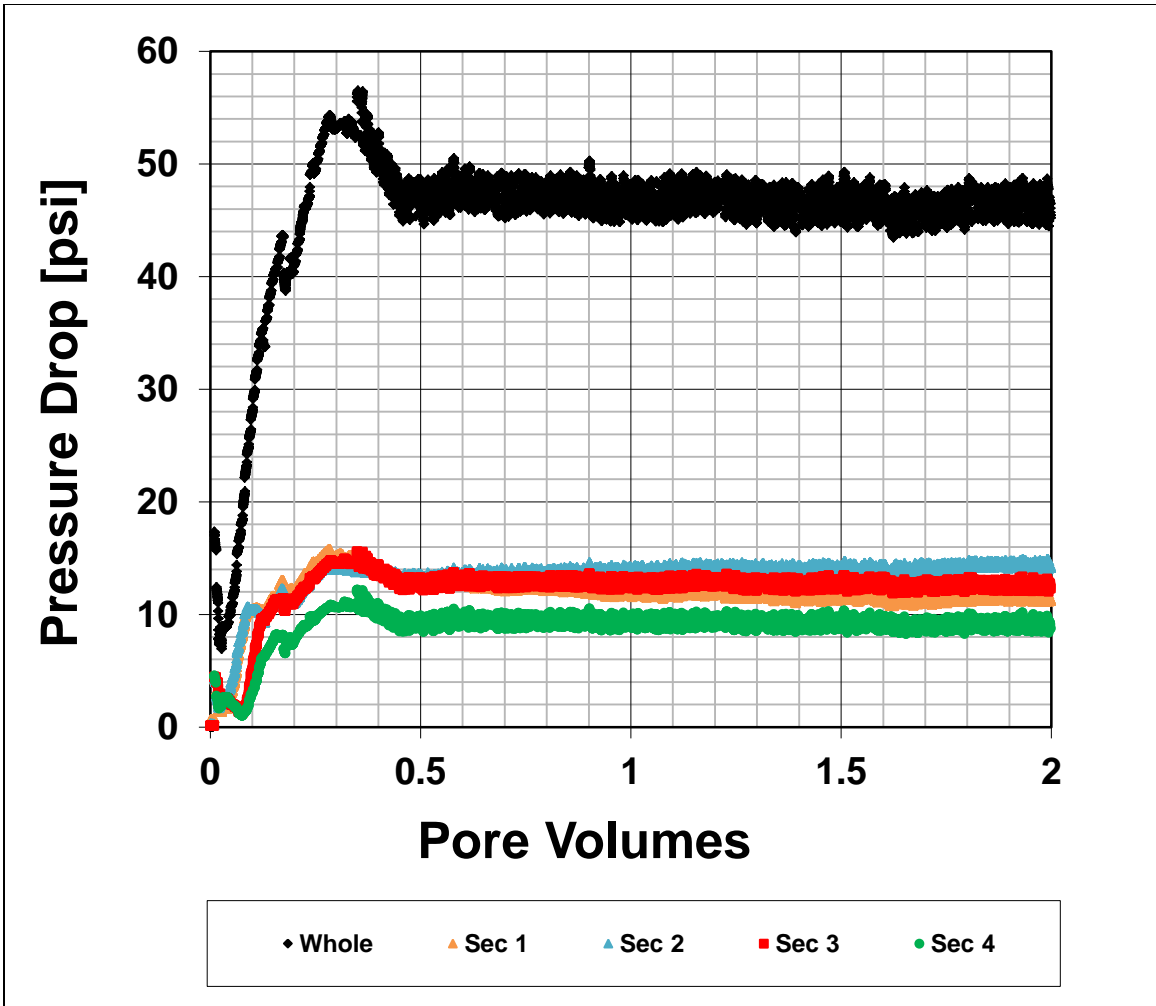


Figure A-7: Brine fractional flow at 0.5, 1859 psi 40 C.

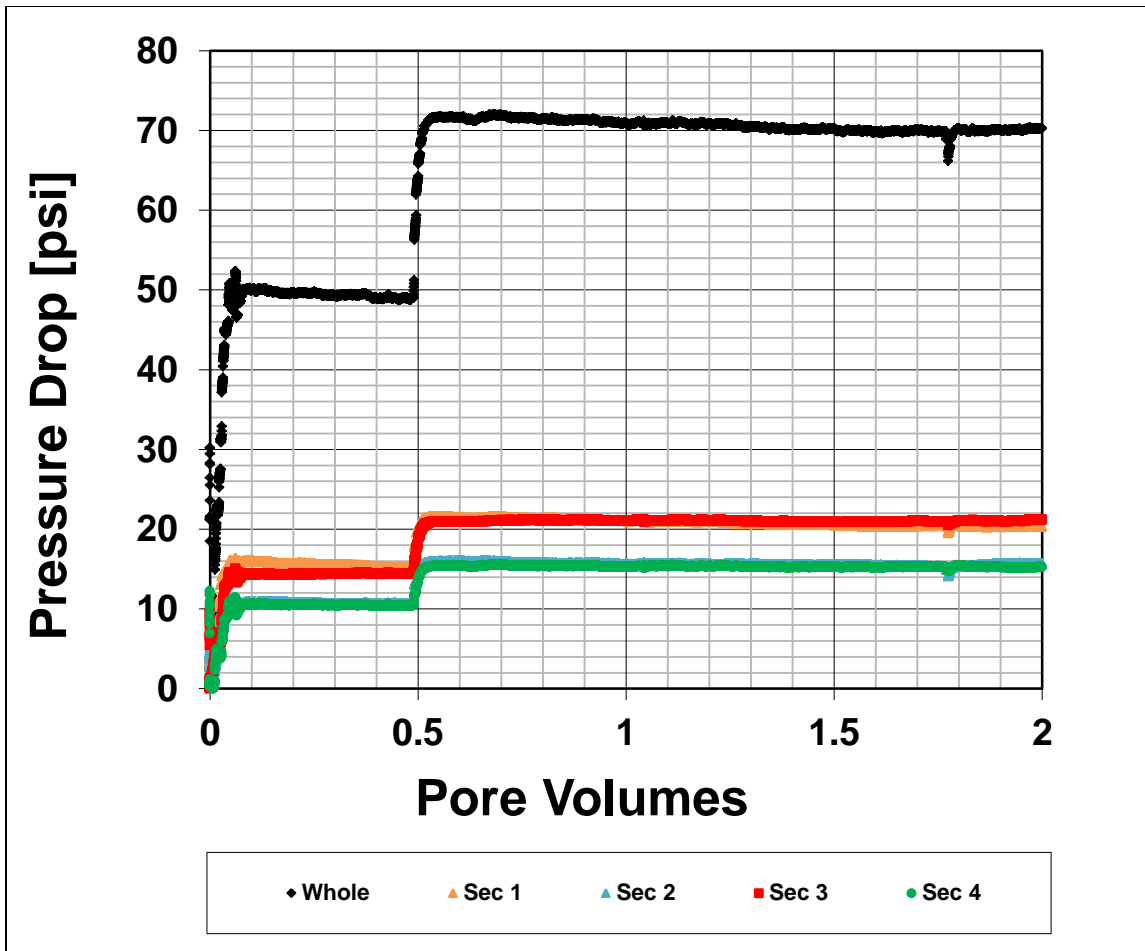


Figure A-8: CO₂-saturated brine flood, 1868 psi 40 C. Flow rate of 1 mL/min followed by 1.5 mL/min.

LOW DENSITY CO₂ AND BRINE FLOODING

Drainage Regime

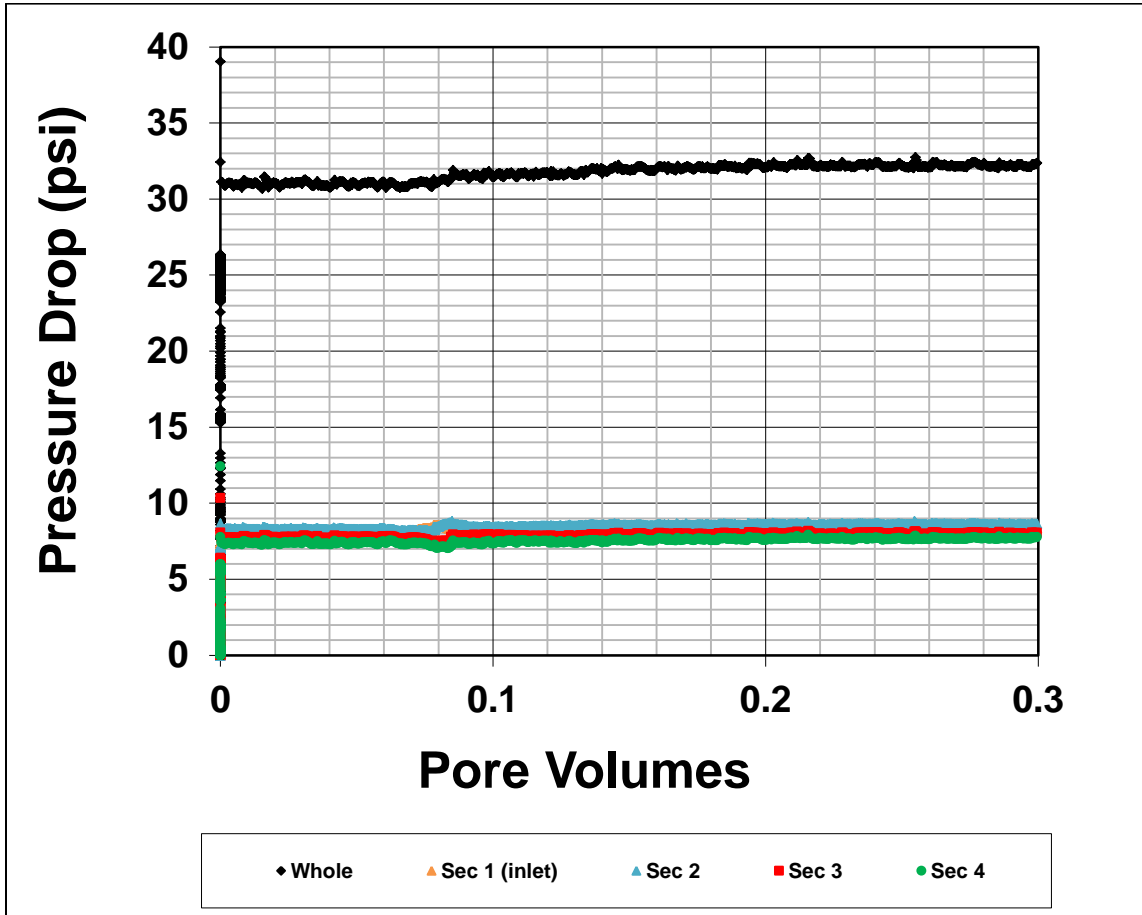


Figure A-9: CO₂-saturated brine flood, 1170 psi 40 C.

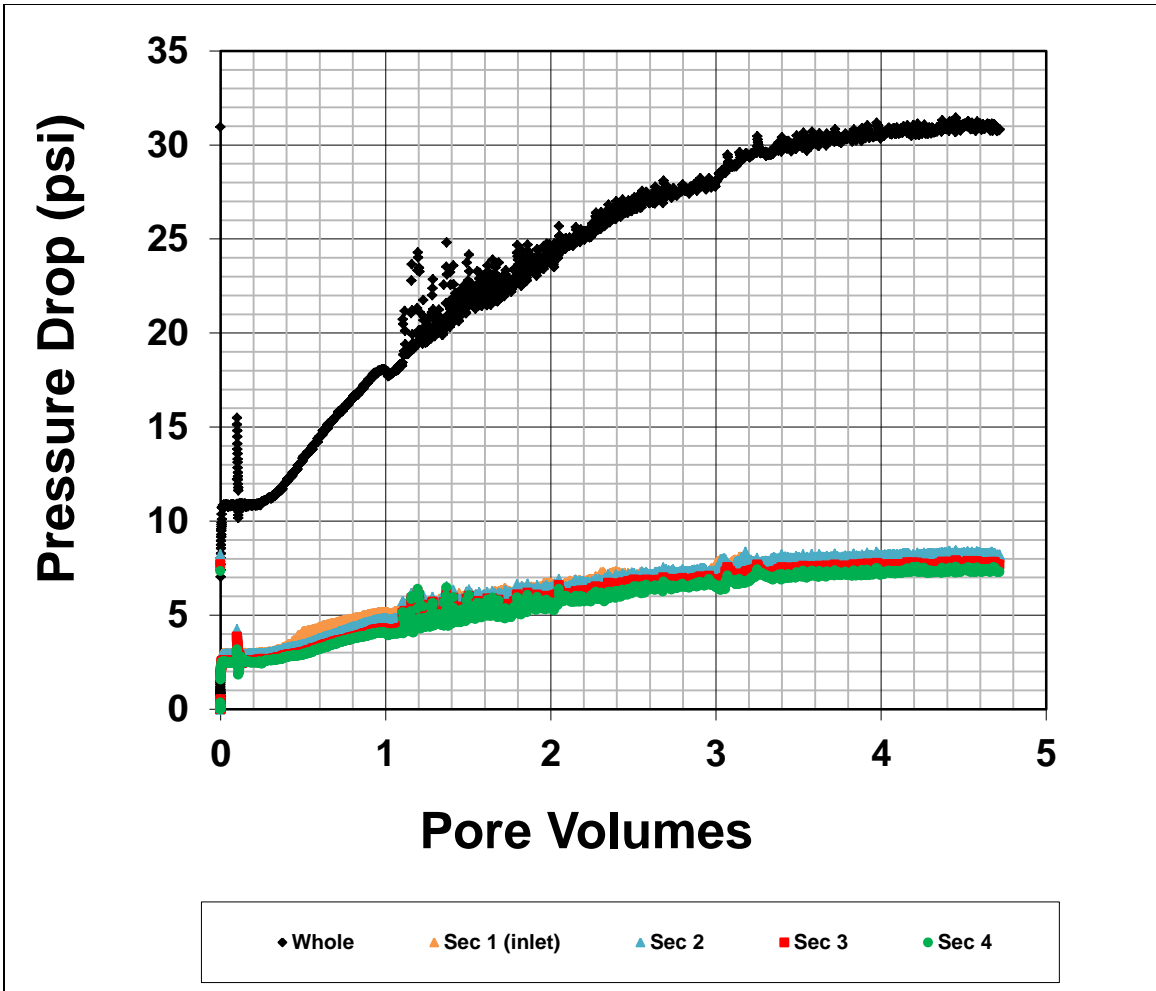


Figure A-10: Brine fractional flow at 0.25, 1178 psi 40 C.

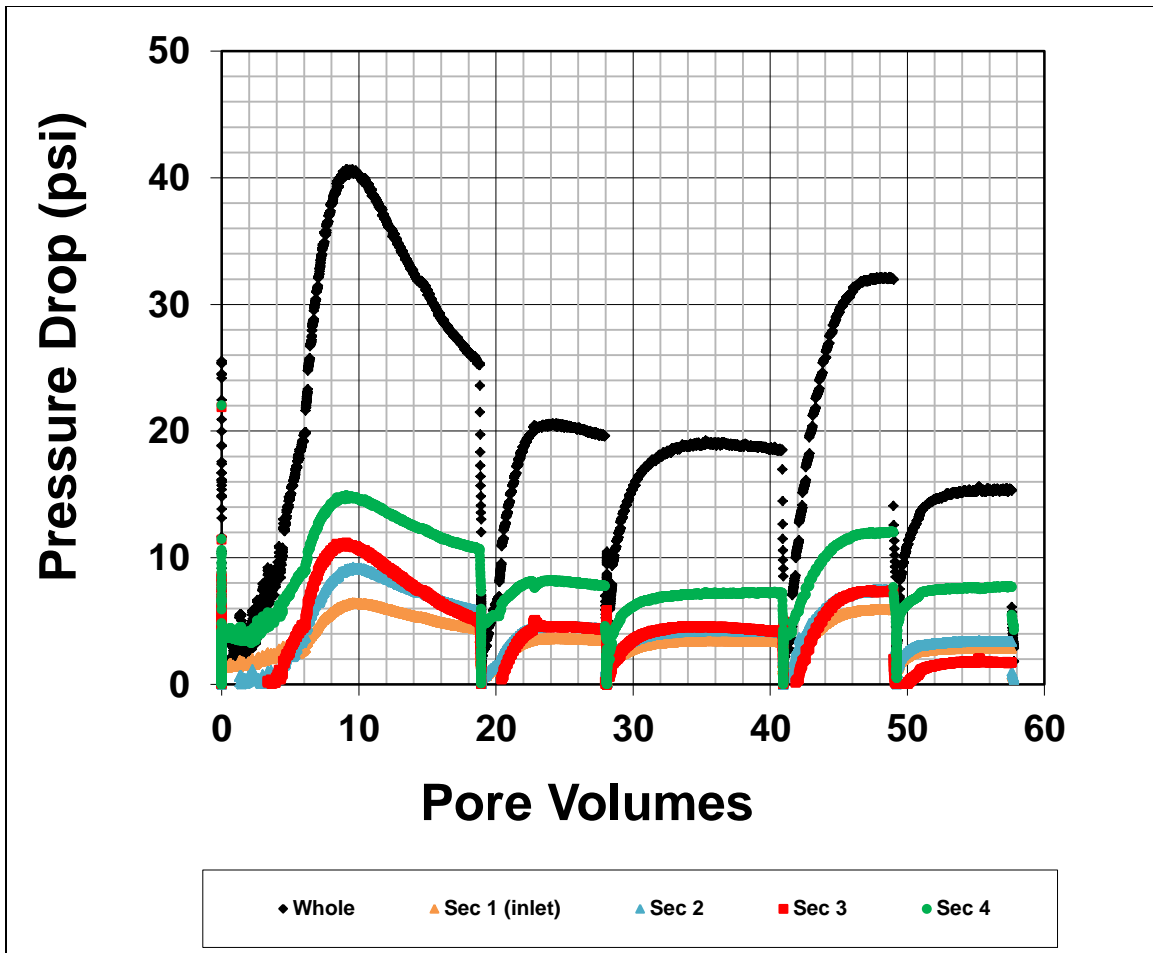


Figure A-11: Brine fractional flow at zero, 1180 psi 40 C. The discontinuities of pressure drop indicate when the apparatus was switched to a full accumulator of CO₂.

Imbibition Regime

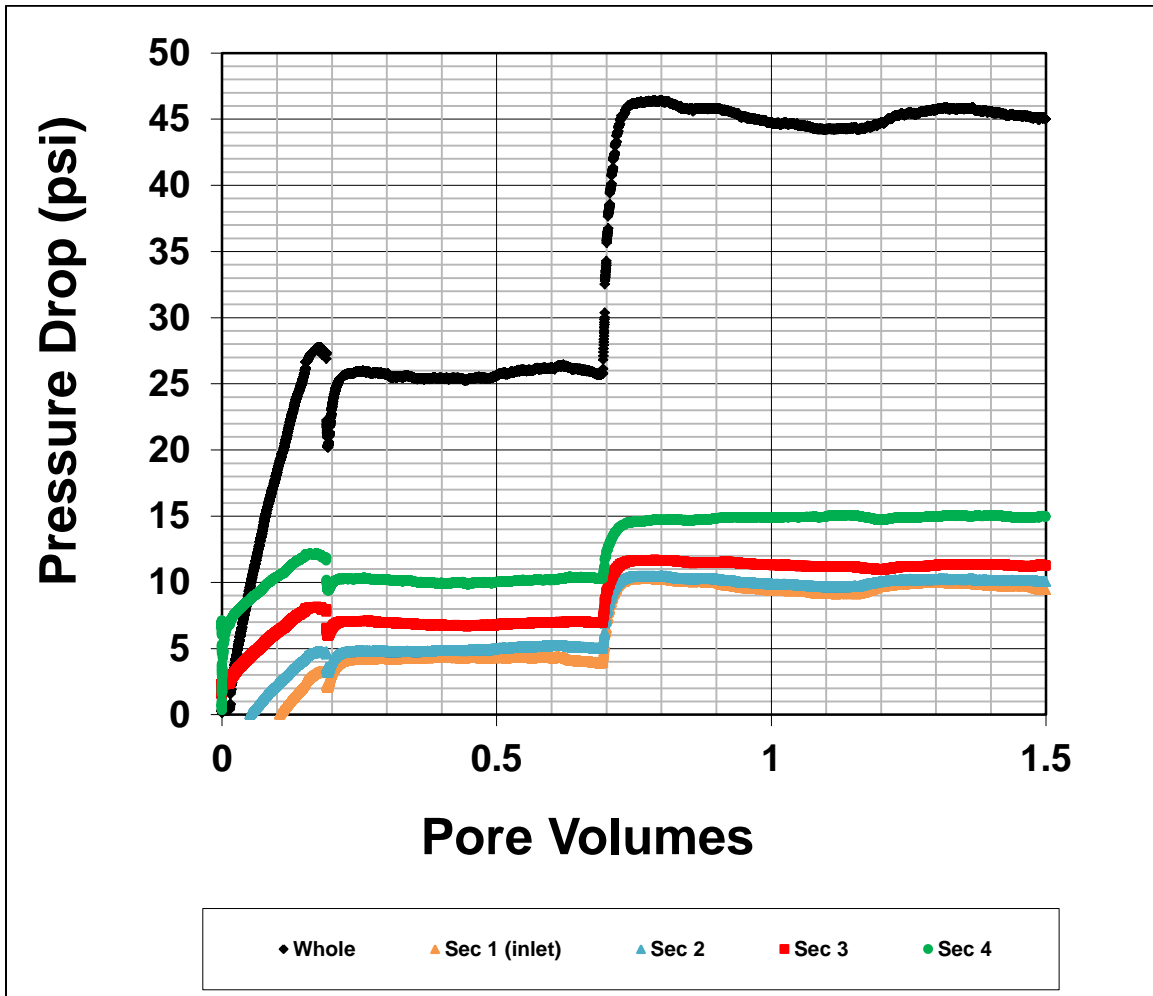


Figure A-12: CO₂-saturated brine flood, 1176 psi 40 C. Flow rate of 0.5 mL/min followed by 1 mL/min.

N₂ AND BRINE FLOODING

Drainage Regime

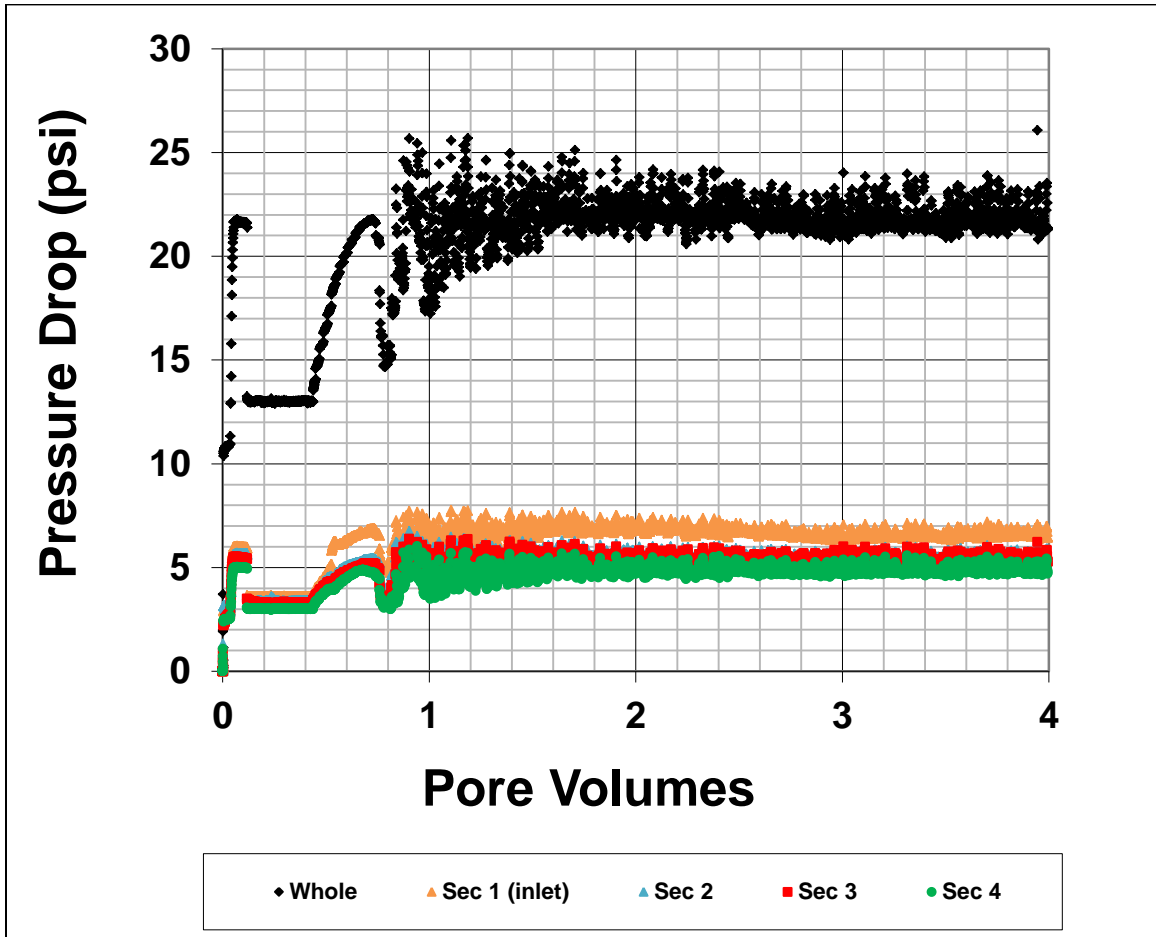


Figure A-13: Brine fractional flow at 0.498, 1853 psi 40 C.

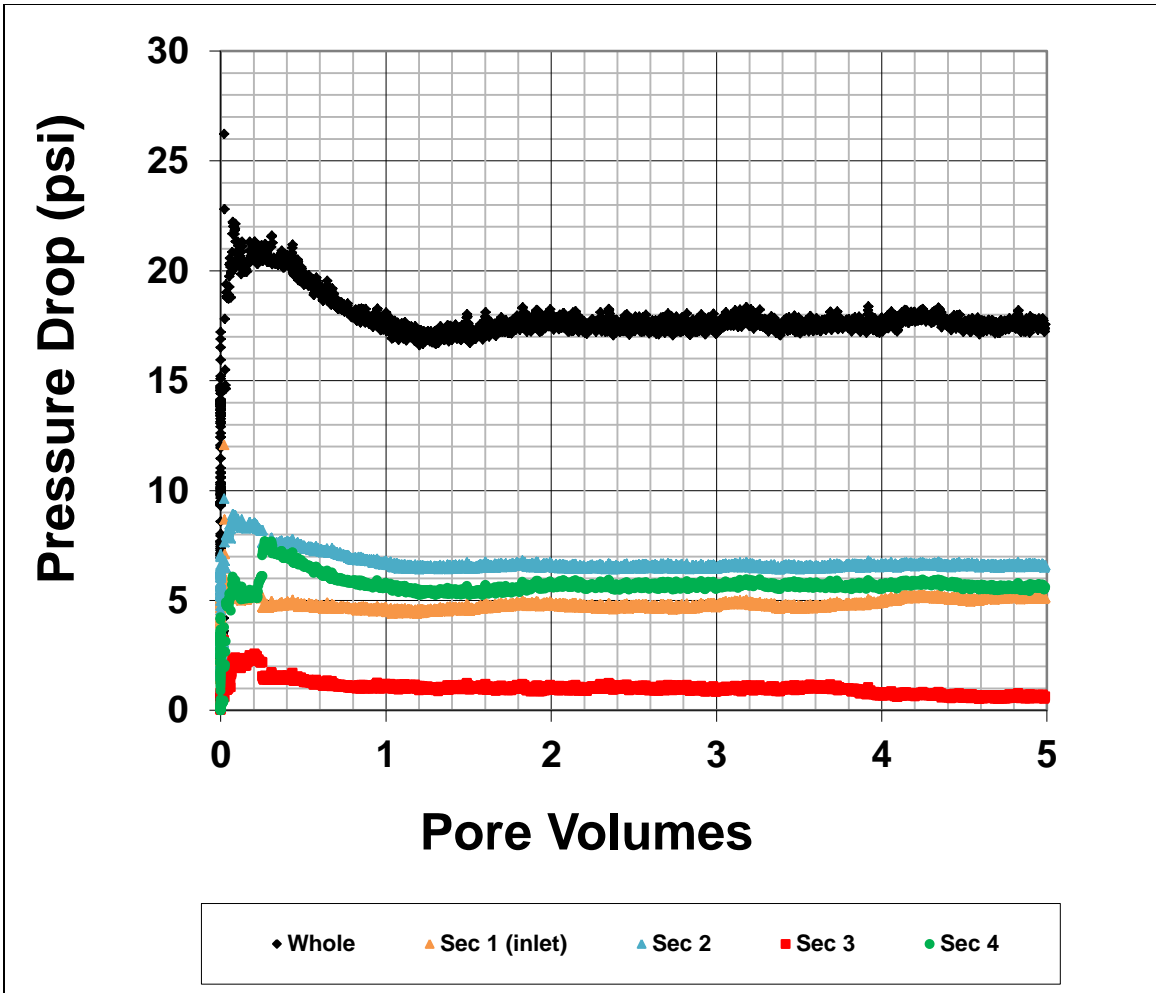


Figure A-14: Brine fraction flow at 0.103, 1855 psi 40 C.

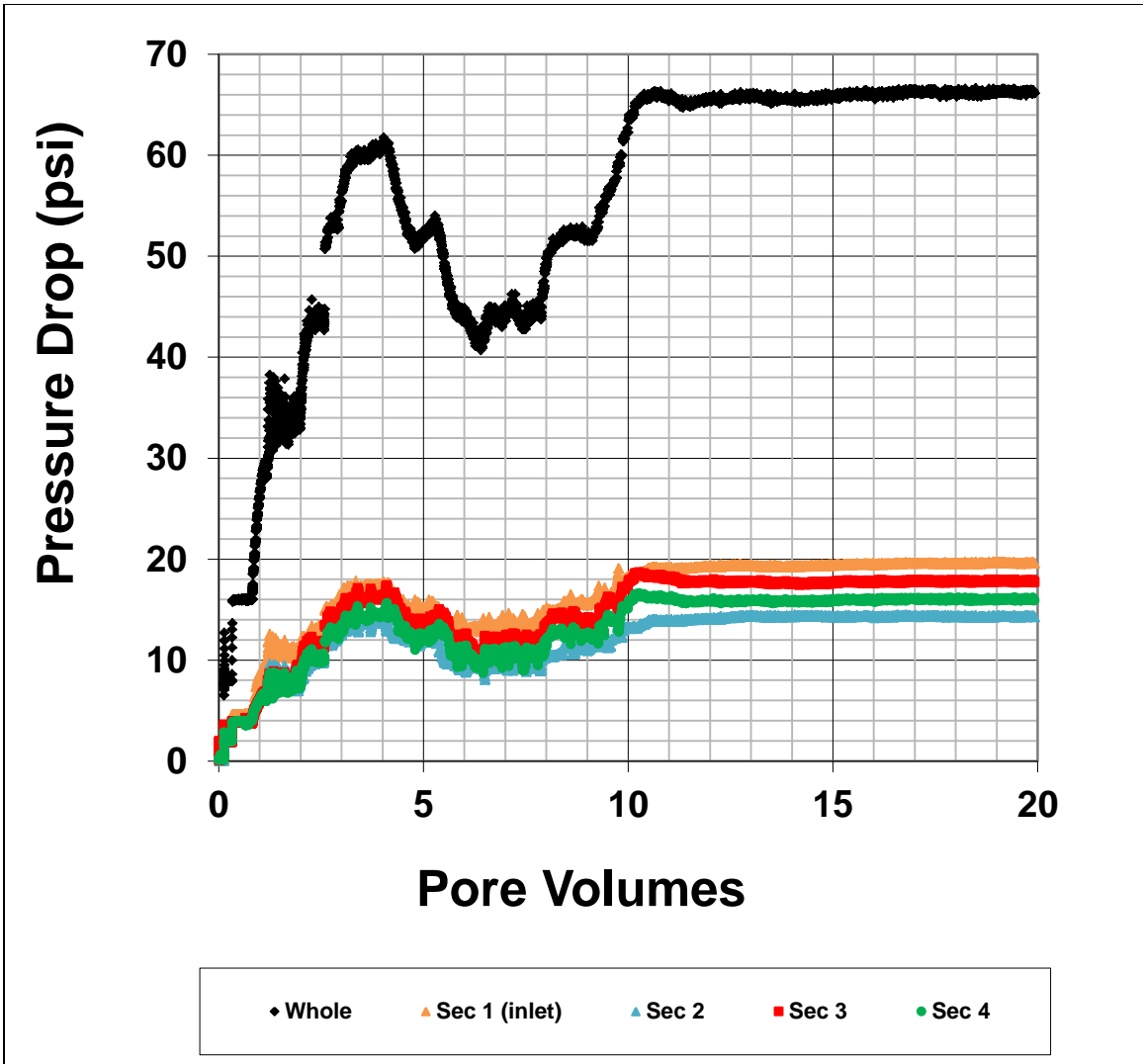


Figure A-15: Brine fractional flow at 0.0451, 1848 psi 40 C.

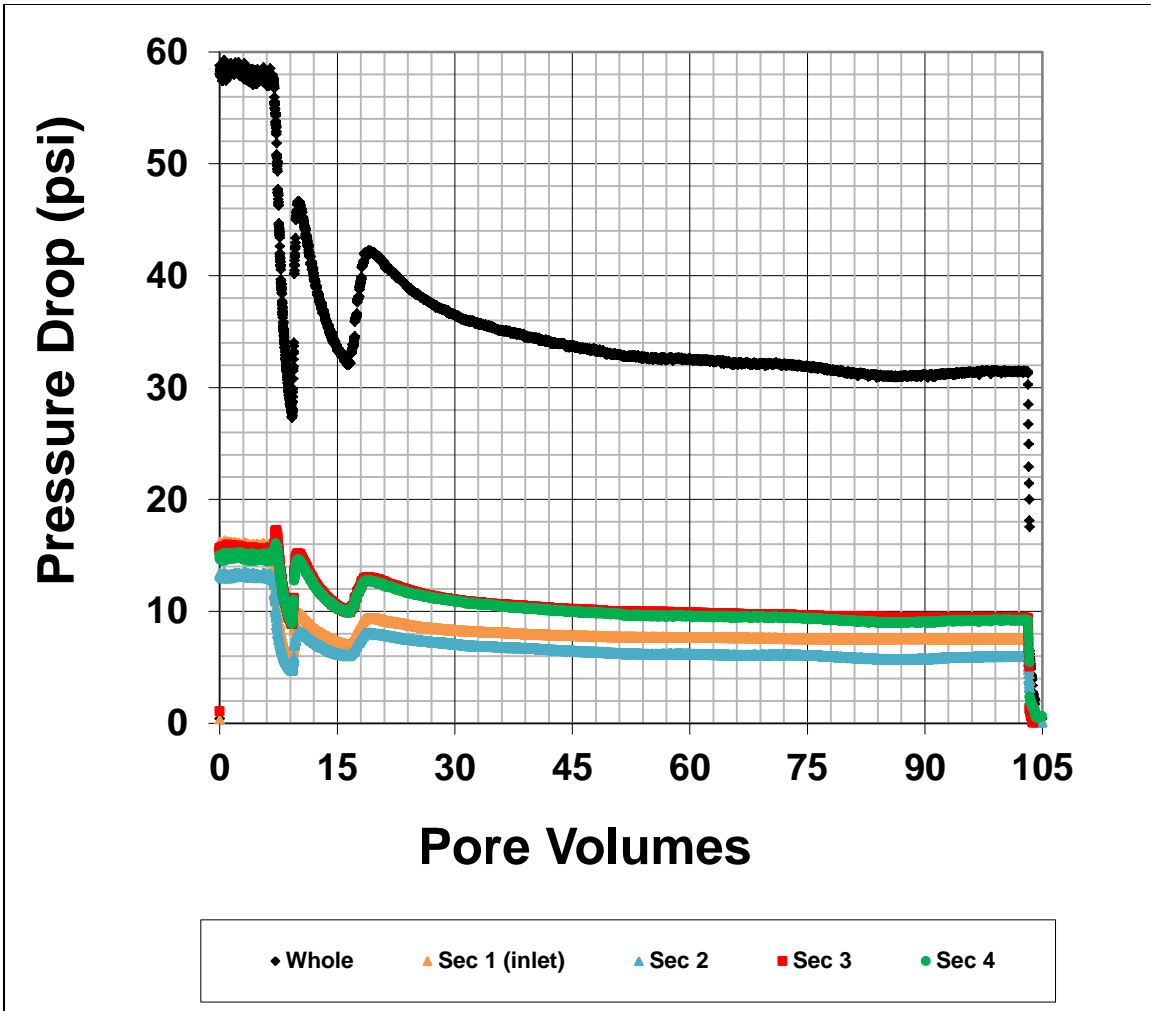


Figure A-16: Brine fractional flow at zero, 1889 psi 40 C.

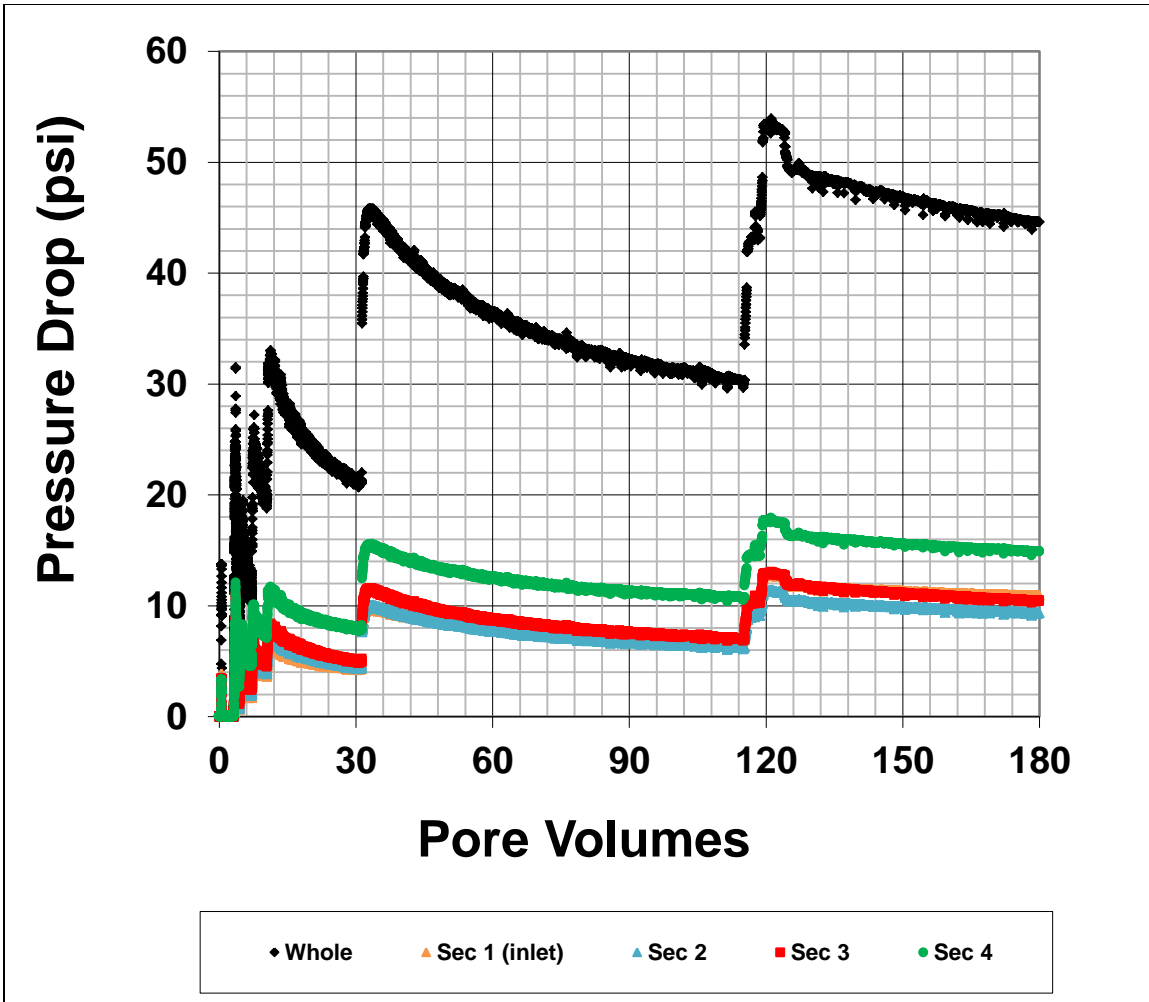


Figure A-17: Brine fractional flow at zero, 1854 psi 40 C. Flowrate increased in a stepwise fashion.

Imbibition Regime

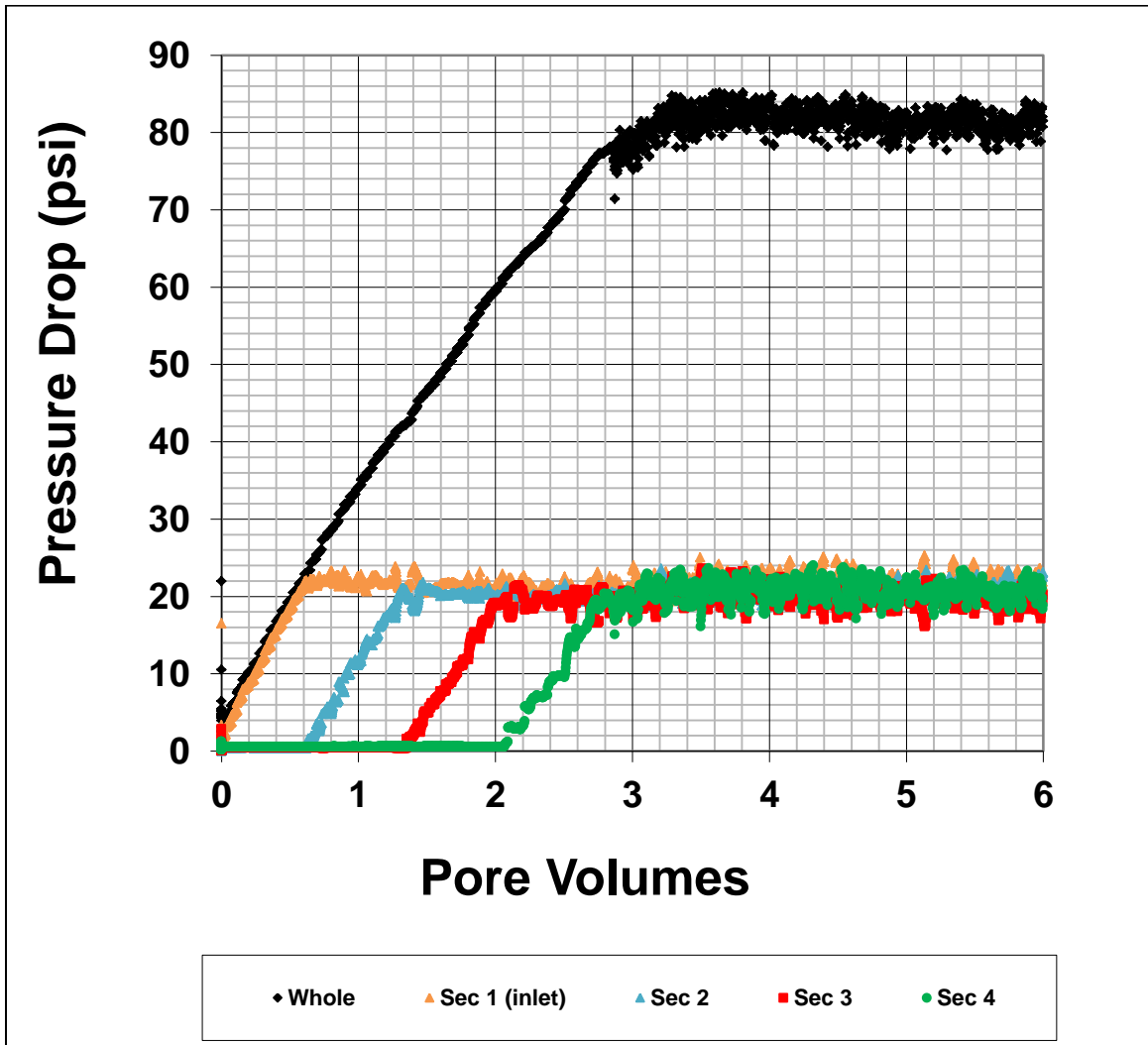


Figure A-18: Brine fractional flow at 0.0559, 1845 psi 40 C.

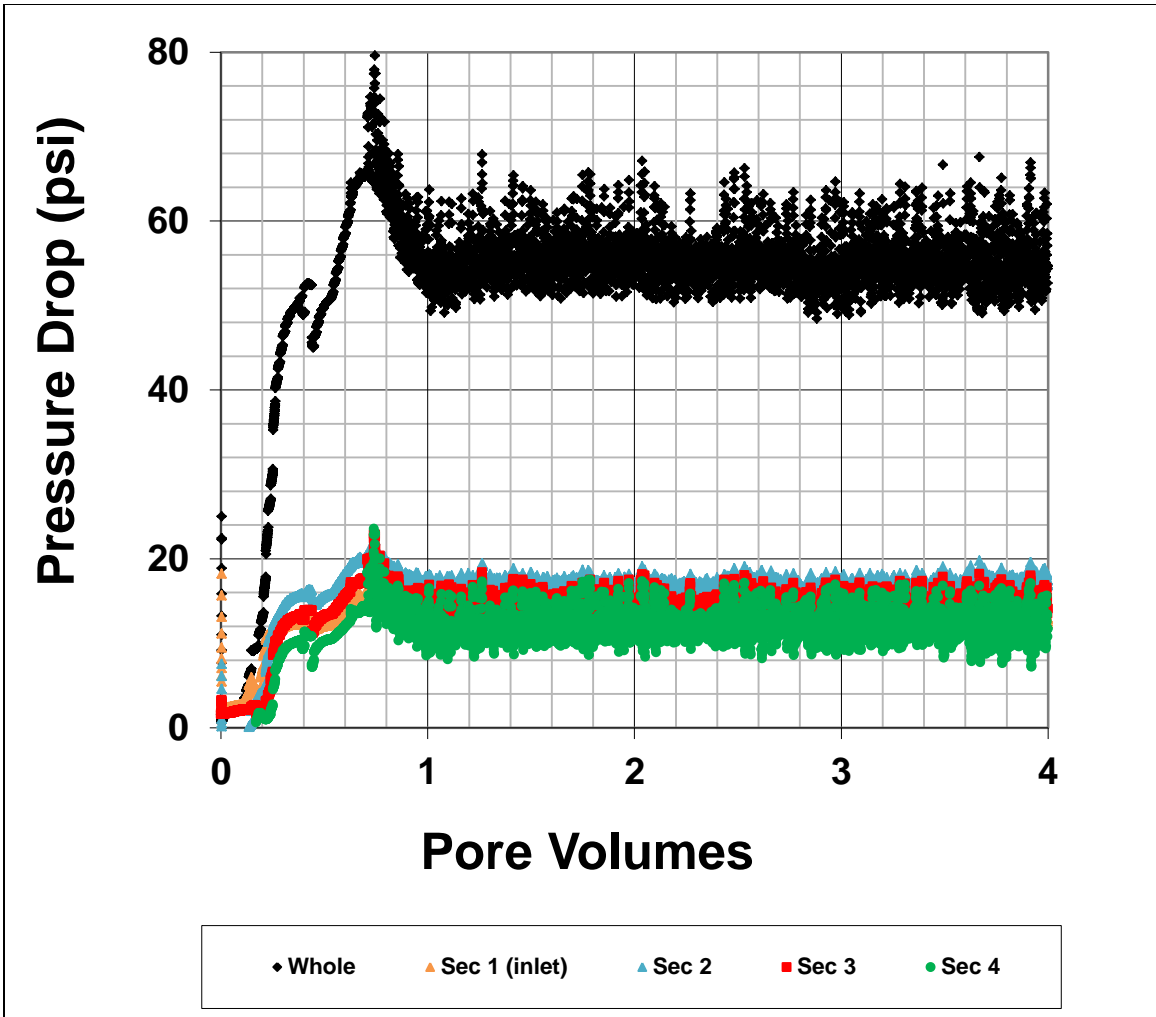


Figure A-19: Brine fractional flow at 0.198, 1843 psi 40 C.

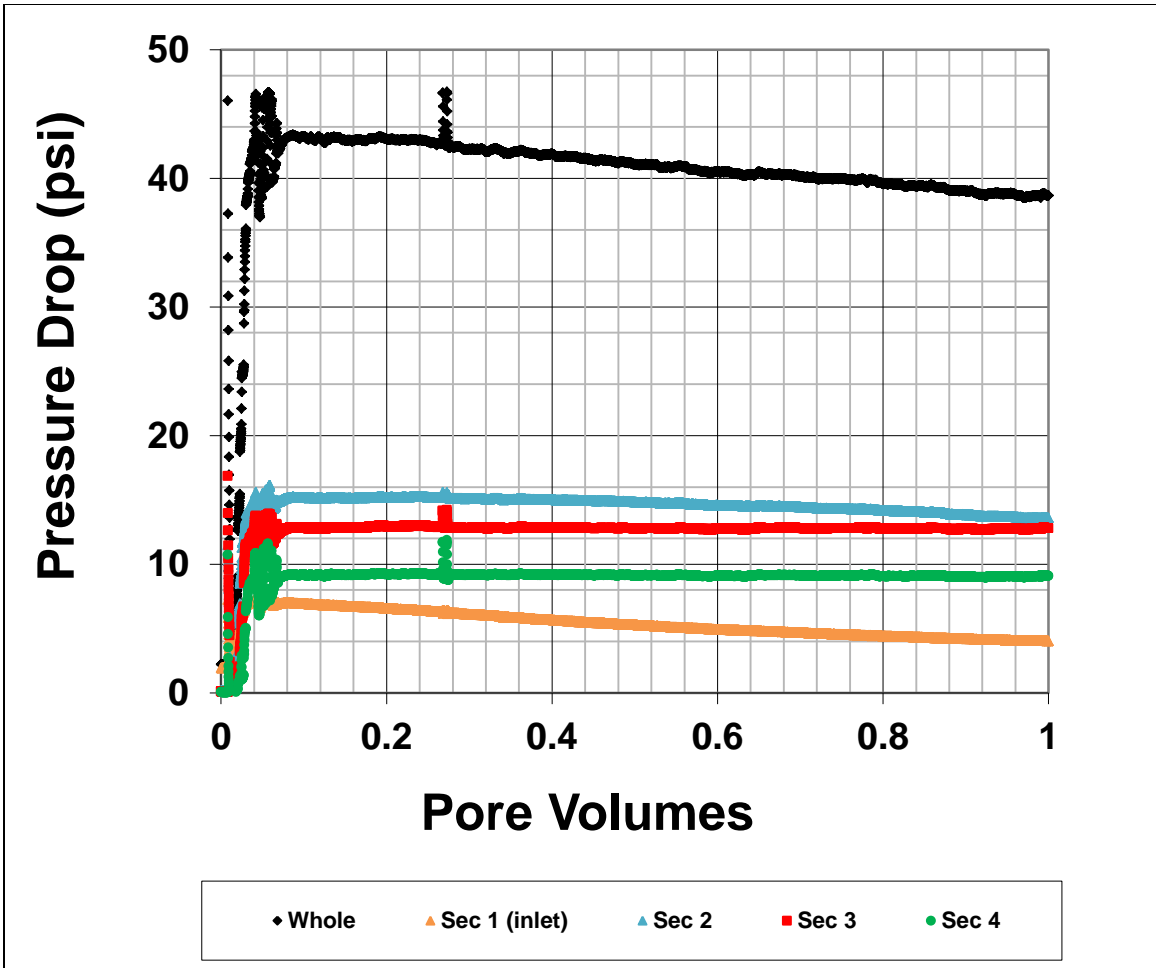


Figure A-20: Brine flooding, 1842 psi 40 C. The continually decreasing differential pressure is unexplained.

N-DECANE AND BRINE FLOODING

Drainage Regime

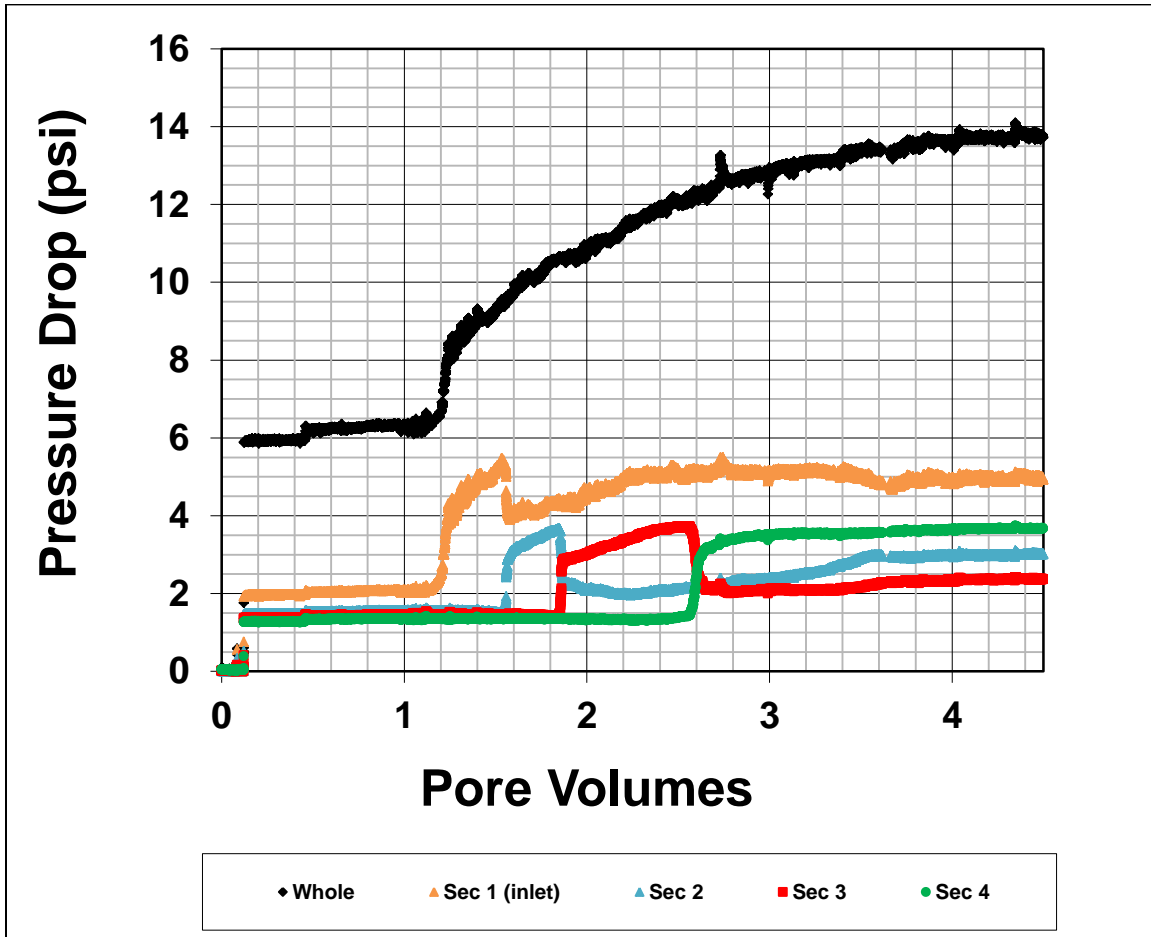


Figure A-21: Brine fractional flow at 0.95, 1536 psi 70 C.

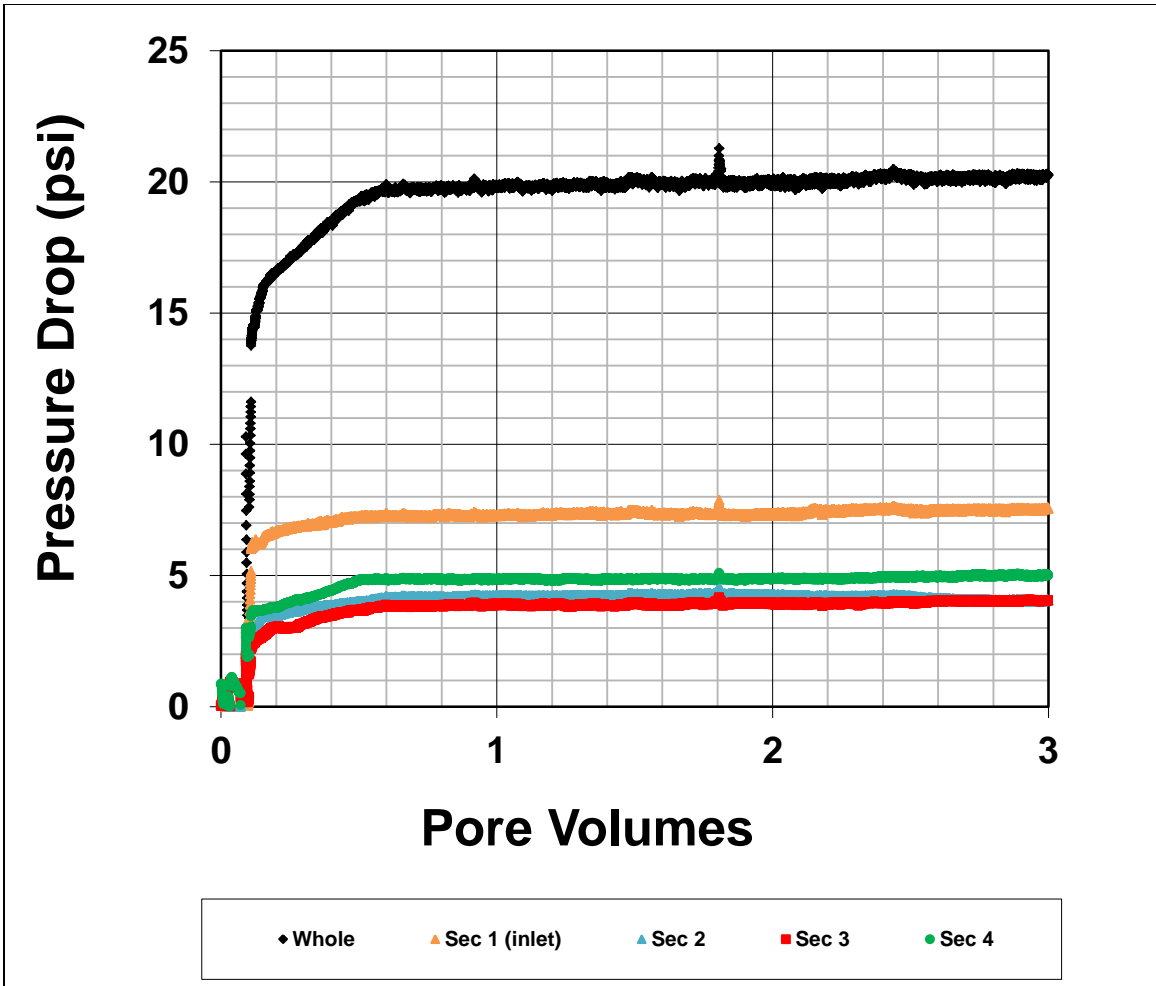


Figure A-22: Brine fractional flow at 0.75, 1553 psi 70 C.

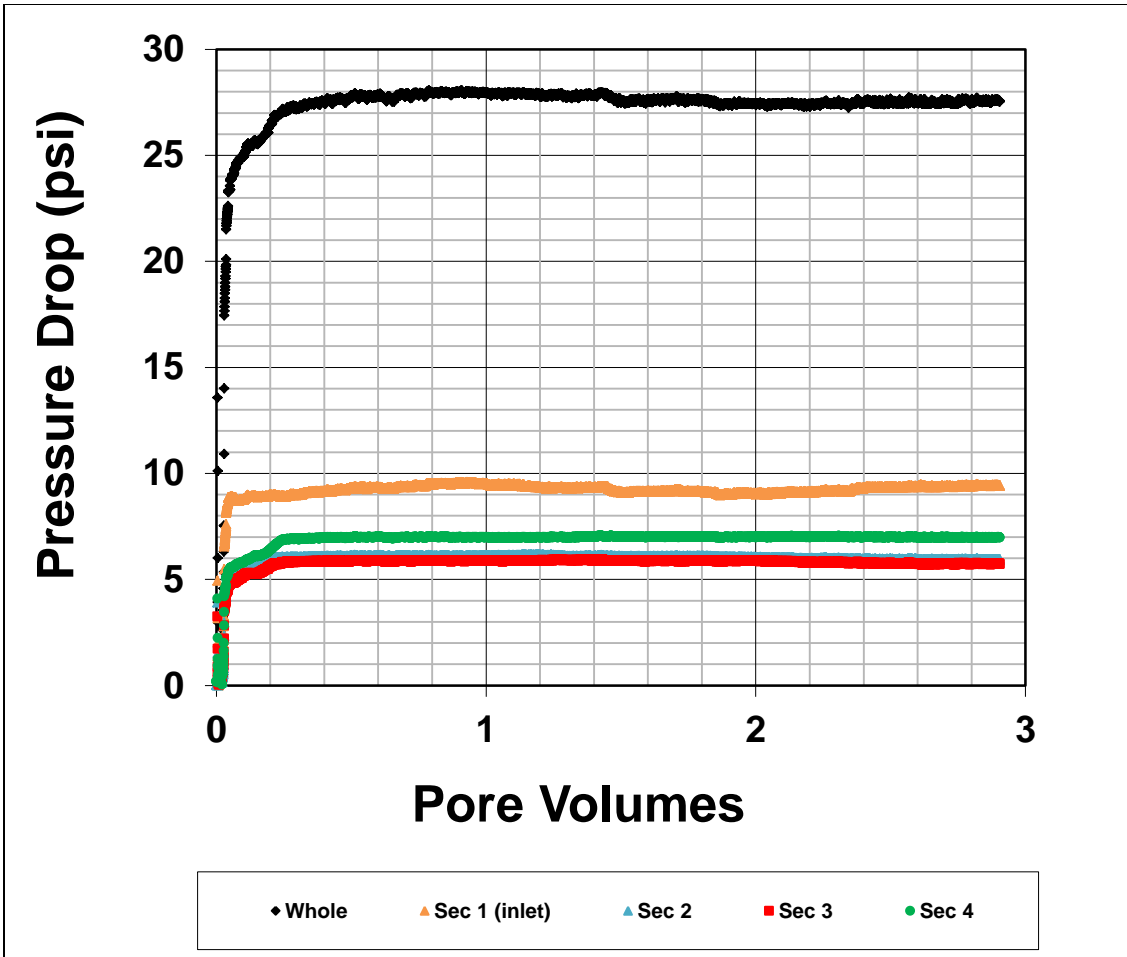


Figure A-23: Brine fractional flow at 0.25, 1549 psi 70 C.

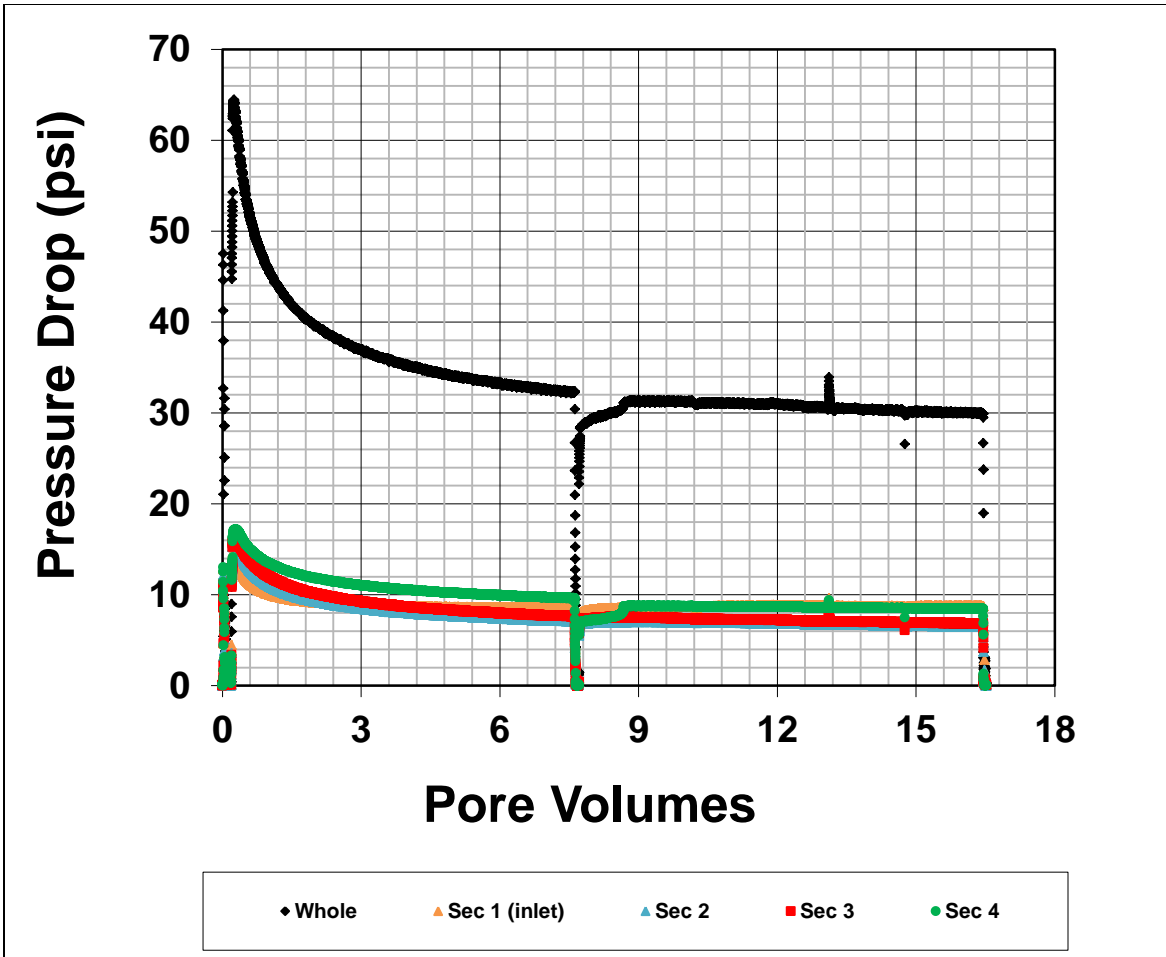


Figure A-24: Brine fractional flow at zero, 1547 psi 70 C. The discontinuities of pressure drop indicate when the apparatus was switched to a full accumulator of n-decane.

References

(2015-2016). <http://webbook.nist.gov>

Akbarabadi, M., & Piri, M. (2014, August 27). Co-sequestration of SO₂ with supercritical CO₂ in carbonates: An experimental study of capillary trapping, relative permeability, and capillary pressure. *Advances in Water Resources*, 77, 44-56. <http://dx.doi.org/10.1016/j.advwatres.2014.08.011>

Al-Yaseri, A., Sarmadivaleh, M., Saeedi, A., Lebedev, M., Barifcani, A., & Iglauer, S. (2015, January 23). N₂ CO₂ NaCl brine interfacial tensions and contact angles on quartz at CO₂ storage site conditions in the Gippsland basin, Victoria/Australia. *Journal Of Petroleum Science and Engineering*, 129, 58-62. <http://dx.doi.org/10.1016/j.petrol.2015.01.026>

Asakawa, K. (2005). *A Generalized Analysis of Partitioning Interwell Tracer Tests* (Doctoral dissertation). The University of Texas at Austin, Austin, Texas.

Bachu, S., & Bennion, D. B. (2008, December 31). Interfacial Tension between CO₂, Freshwater, and Brine in the Range of Pressure from (2 to 27) MPa, Temperature from (20 to 125) °C, and Water Salinity from (0 to 334 000) mg·L⁻¹. *Journal of Chemical Engineering Data*, 54, 765-775. doi:10.1021/je800529x

Bando, S., Takemura, F., Nishio, M., Hihara, E., & Akai, M. (2003, March 28). Solubility of CO₂ in Aqueous Solutions of NaCl at (30 to 60) °C and (10 to 20) MPa. *Journal of Chemical and Engineering Data*, 48(3), 576-579. doi:10.1021/je0255832

Brandt, M. (2010). Introduction to Absorbance Spectroscopy. https://www.rose-hulman.edu/~brandt/Fluorescence/Absorbance_Spectroscopy.pdf

Brooks, R. H., & Corey, A. T. (1964, March). Hydraulic Properties of Porous Media. *Hydrology Papers*, Colorado State University.

Brownell, L.E. and Katz, D.L. (1949). Flow of fluids through porous media, Part II. *Chem. Eng. Process.*, 43: 601-612.

- Cai, B., Yang, J., & Guo, T. (1996, March 15). Interfacial Tension of Hydrocarbon + Water/Brine Systems under High Pressure. *Journal of Chemical Engineering Data*, 41, 493-496.
- Chatzis, I., & Morrow, N. R. (1984, October). Correlation of Capillary Number Relationships for Sandstone. *Society of Petroleum Engineers Journal*. <http://dx.doi.org/10.2118/10114-PA>
- Chen, X., Kianinejad, A., & DiCarlo, D. A. (2014). An Experimental Study of CO₂-Brine Relative Permeability in Sandstone. *Society of Petroleum Engineers*. <http://dx.doi.org/10.2118/169137-MS>
- Chiquet, P., Broseta, D., & Thibeau, S. (2007). Wettability alteration of caprock minerals by carbon dioxide. *Geofluids*, 7, 112-122. doi: 10.1111/j.1468-8123.2007.00168.x
- Deans, H. A. (1978). Using Chemical Tracers to Measure Fractional Flow and Saturation In-Situ. *Society of Petroleum Engineers*. <http://dx.doi.org/10.2118/7076-MS>
- Dria, D. E. (1989). *A Study of Three-Phase Relative Permeabilities and Dispersivities Under Carbon Dioxide Flooding Conditions in a Heterogeneous Carbonate Core* (Doctoral dissertation). The University of Texas at Austin, Austin, Texas.
- Dwarakanath, V. (1997). *Characterization and Remediation of Aquifers Contaminated by Nonaqueous Phase Liquids Using Partitioning Tracers and Surfactants* (Doctoral dissertation). The University of Texas at Austin, Austin, Texas.
- Hansen, G., Hamouda, A. A., & Denoyel, R. (2000). The effect of pressure on contact angles and wettability in the mica/water/n-decane system and the calcite + stearic acid/water/n-decane system. *Colloids and Surfaces*, 172, 7-16.
- Haynes, W. M. (2016, June 24). *Handbook of Chemistry and Physics 97th Edition*. Retrieved August 1, 2016, from <http://hbcponline.com/>

- Kestin, J., Khalifa, H. E., & Correia, R. J. (1981). Tables of the Dynamic and Kinematic Viscosity of Aqueous NaCl Solutions in the Temperature Range 20-150 °C and the Pressure Range 0.1-35 MPa. *Journal of Phys. Chem. Ref. Data*, 10(1).
- Krevor, S., Pini, R., Zuo, L., & Benson, S. M. (2012, February 28). Relative permeability and trapping of CO₂ and water in sandstone rocks at reservoir conditions. *Water Resources Research*, 48. doi:doi:10.1029/2011WR010859
- Lake, L. W. (1989). *Enhanced Oil Recovery*. Englewood Cliffs, NJ: Prentice Hall. 48-57.
- Leverett, M. C. (1941). *Capillary Behavior in Porous Solids*. *Petroleum Technology*.
- Levine, J. S., Goldberg, D. S., Lackner, K. S., Matter, J. M., Supp, M. G., & Ramakrishnan, T. S. (2013, November 25). Relative Permeability Experiments of Carbon Dioxide Displacing Brine and Their Implications for Carbon Sequestration. *Environmental Science & Technology*, 48, 811-818. [dx.doi.org/10.1021/es401549e](https://doi.org/10.1021/es401549e)
- Liu, N., Ghorpade, S., Harris, L., Li, L., Grigg, R., & Lee, R. (2010). The Effect of Pressure and Temperature on Brine-CO₂ Relative Permeability and IFT at Reservoir Conditions. *Society of Petroleum Engineers*.
- Neshat, S. S. (2016, August). *Compositional Three-phase Relative Permeability and Capillary Pressure Models Using Gibbs Free Energy* (Master's Thesis) The University of Texas at Austin, Austin, Texas.
- Oak, M. J., Baker, L. E., & Thomas, D. C. (1990, August). Three-Phase Relative Permeability of Berea Sandstone. *JPT*.
- Pentland, C.H., El-Maghraby, R., Iglauer, S., Blunt, M.J. (2011). Measurements of capillary trapping of super-critical carbon dioxide in Berea sandstone, *Geophysical Research Letters* 38, L06401.

- Perrin, J., & Benson, S. (2009, June 30). An Experimental Study on the Influence of Sub-Core Scale Heterogeneities on CO₂ Distribution in Reservoir Rocks. *Transp. Porous Med.*, 82, 93-109. doi:10.1007/s11242-009-9426-x.
<http://pangea.stanford.edu/research/bensonlab/relperm>
- Perrin, J., Krause, M., Kuo, C., Miljkovic, L., Charoba, E., & Benson, S. M. (2009). Core-scale experimental study of relative permeability properties of CO₂ and brine in reservoir rocks. *Energy Procedia*, 3515-3522.
doi:10.1016/j.egypro.2009.02.144
- Pini, R., & Benson, S. M. (2013, June 18). Simultaneous determination of capillary pressure and relative permeability curves from core-flooding experiments with various fluid pairs. *Water Resources Research*, 49, 3516-3530.
doi:10.1002/wrcr.20274
- Rapoport, L. A., & Leas, W. J. (1953). Properties of Linear Waterfloods. *Petroleum Transactions, AIME*, 198, 139-148.
- Sabirzyanov, A. N., Il'in, A. P., Akhunov, A. R., & Gumerov, F. M. (2002). Solubility of Water in Supercritical Carbon Dioxide. *High Temperature*, 40(2), 203-206.
doi:10.1023/A:1015294905132
- Saraji, S., Goual, L., Piri, M., & Plancher, H. (2013, April 30). Wettability of Supercritical Carbon Dioxide/Water/Quartz Systems: Simultaneous Measurement of Contact Angle and Interfacial Tension at Reservoir Conditions. *Langmuir*, 29, 6856-6866. doi:dx.doi.org/10.1021/la3050863
- Shook, G. M., Pope, G. A., & Asakawa, K. (2009). Determining Reservoir Properties and Flood Performance From Tracer Test Analysis. *Society of Petroleum Engineers Journal*. <http://dx.doi.org/10.2118/124614-MS>
- Yan, W., Zhao, G., Chen, G., & Guo, T. (2001, October 13). Interfacial Tension of (Methane Nitrogen) Water and (Carbon Dioxide Nitrogen) Water Systems. *J. Chem. Eng. Data*, 46, 1544-1548. doi:10.1021/je0101505

Yuan, C., & Pope, G. A. (2012, December). A New Method to Model Relative Permeability in Compositional Simulators to Avoid Discontinuous Changes Caused by Phase Identification Problems. *SPE Journal*.
<http://dx.doi.org/10.2118/142093-PA>

Vita

Paul Byron Jordan graduated from The University of Texas at Austin in 2010 with a Bachelor's degree in Chemical Engineering with an emphasis on Process and Biotechnology. After working for BP America for over three years as a subsea engineer, in 2014 he enrolled in the graduate program within the Petroleum Engineering department at The University of Texas at Austin, where he received his Master's degree in 2016. He lives with his girlfriend and dog, Chloe and Rockefeller.

This thesis was typed by Paul Byron Jordan and he can be reached at p.jordan84@gmail.com.